Thin film deposition of arsenic free pnictide superconductors

Vom Fachbereich Material- und Geowissenschaften
zur Erlangung des akademischen Grades Doktor-Ingenieur (Dr.-Ing.)
genehmigte Dissertation von Dipl.-Ing. Alexander U. Buckow aus Hanau
Mai 2015 — Darmstadt — D 17

TECHNISCHE
UNIVERSITÄT
DARMSTADT

Thin film deposition of arsenic free pnictide superconductors

Genehmigte Dissertation von Dipl.-Ing. Alexander U. Buckow aus Hanau

1. Gutachten: Prof. Dr. Lambert Alff
2. Gutachten: Prof. Dr. Wolfgang Donner

Tag der Einreichung: 20.08.2014
Tag der Prüfung: 13.05.2015

Darmstadt — D 17

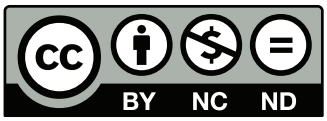

Erklärung zur Dissertation

Hiermit versichere ich, die vorliegende Dissertation ohne Hilfe Dritter nur mit den angegebenen Quellen und Hilfsmitteln angefertigt zu haben. Alle Stellen, die aus Quellen entnommen wurden, sind als solche kenntlich gemacht. Diese Arbeit hat in gleicher oder ähnlicher Form noch keiner Prüfungskommission vorgelegen.

Darmstadt, den 21. Juli 2014

(Alexander U. Buckow)

Contents

1 Introduction

Since the discovery of superconductivity by Heike Kamerlingh Onnes [1] more than a century ago, much has happened in this outstanding field of solid state physics. Although, the superconducting transition temperature T_C could be raised to temperatures above 130 K over the years and, thus, making cooling possible with rather cheap liquid nitrogen, the ultimate goal of finding a room temperature superconductor seems to be elusive.

Despite the limitations imposed by the low transition temperatures, novel superconductors have become more and more important in our modern technological world. Beside medical purposes in MRI machines with their ability to generate extremely high magnetic fields, superconductors have found a huge variety of applications such as microwave frequency filters for communication, measurement devices for nondestructive material analysis and superconducting power generators. Future applications could be lossless electric transport, levitation transport and so on. However, although the mechanism behind superconductivity at low temperatures of conventional superconductors is already known [2], a comprehensive universal theory which explains the superconducting mechanism in high T_C unconventional superconductors is still elusive.

For a long time of more than 20 years, cuprate high temperature superconductors found by Bednorz and Müller [3] were the only superconductors reaching temperatures above 50 K. And they still hold the record with a transition temperature of 164 K (under pressure) [4]. In 2008, a new compound with outstanding superconducting properties was found. Kamihara *et al.* [5] reported, that fluorine doped $LaFeAsO_{1-x}F_x$ is superconducting at temperatures below 26 K. Their announcement of this layered compound led to intense research activities all over the world and soon the T_C was raised to values as high as 56 K [6]. Beside this so called '1111'-type iron-pnictides a wide variety of different compounds have been found, among them but not limited to are the '122'-, '111'- and '11'-type structures.

The need of high quality samples for fundamental as well as technological applications also lead to a strong development of suitable thin film deposition techniques for the growth of films of this materials. Beside the conventional sputtering process, novel techniques like Pulsed Laser Deposition (PLD) and Molecular Beam Epitaxy (MBE) are the methods of choice in the field of thin film deposition. While each technique has its own advantages, for this thesis the last mentioned reactive MBE technique was used. The specific advantage of this technique is the flexibility in studying the composition or site substitution related studies which by other techniques need the preparation of solid state samples which in turn is tedious and time consuming. In addition, once the optimal parameters are found, it is rather easy to substitute one element by another and, thus, it is in principle possible to analyze different compounds in much less time. The disadvantage of MBE approach is, however, the complexity of the whole process and the cost of instrumentation.

Goal of this work is to grow high quality epitaxial pnictide superconductor thin films. The aim here is to substitute the noxious arsenic by another less toxic pnictogen. For that, bismuth is the element of choice. After the optimal deposition parameters are established,

substitution on the rare earth site is the next step to characterize the superconducting properties and maybe to find new compounds of this novel class of superconductors.

After this short introduction Chapter 2 gives a brief overview on superconductivity followed by Chapter 3 which describes the most important aspects of the new class of iron based pnictide superconductors. Chapter 4 is a short survey on the theory of thin film deposition while Chapter 5 deals with the characterization methods used during this thesis. Finally Chapters 6 and 7 are a detailed description of the thin film deposition process and the search for the optimal growth parameters. The crystallographic and superconducting properties are analyzed for their dependence of different growth parameters and finally a substitution on different atomic sites is performed. To finalize this thesis, a short summary with an outlook on future work based on the results described here is given in Chapter 8.

2 Superconductivity

Superconductivity is an outstanding phenomenon in solid state physics. The two main characteristics of superconductivity are the lossless transport of electrical current below a specific temperature, called the transition temperature T_C, and the perfect diamagnetic behaviour, called the Meissner effect after its discoverer. Discovered in 1911 by Heike Kammerlingh Onnes [1] in mercury, superconductivity was a pure low temperature phenomenon for almost 70 years. Only in 1986, Bednorz and Müller [3] discovered a novel class of high temperature superconductors, namely the cuprates. Superconductivity now is no longer limited to metals or metallic alloys but also observed in oxide ceramics. Soon T_C reached values above the level of liquid nitrogen temperature in $YBa_2Cu_3O_{7-\delta}$ [7] and maximum transition temperatures of 134 K were reported in $Hg_{0.8}Tl_{0.2}Ba_2Ca_2Cu_3O_{8.33}$ [8]. The following chapter gives an overview about the basics of superconductors and theoretical approaches to explain this phenomenon.

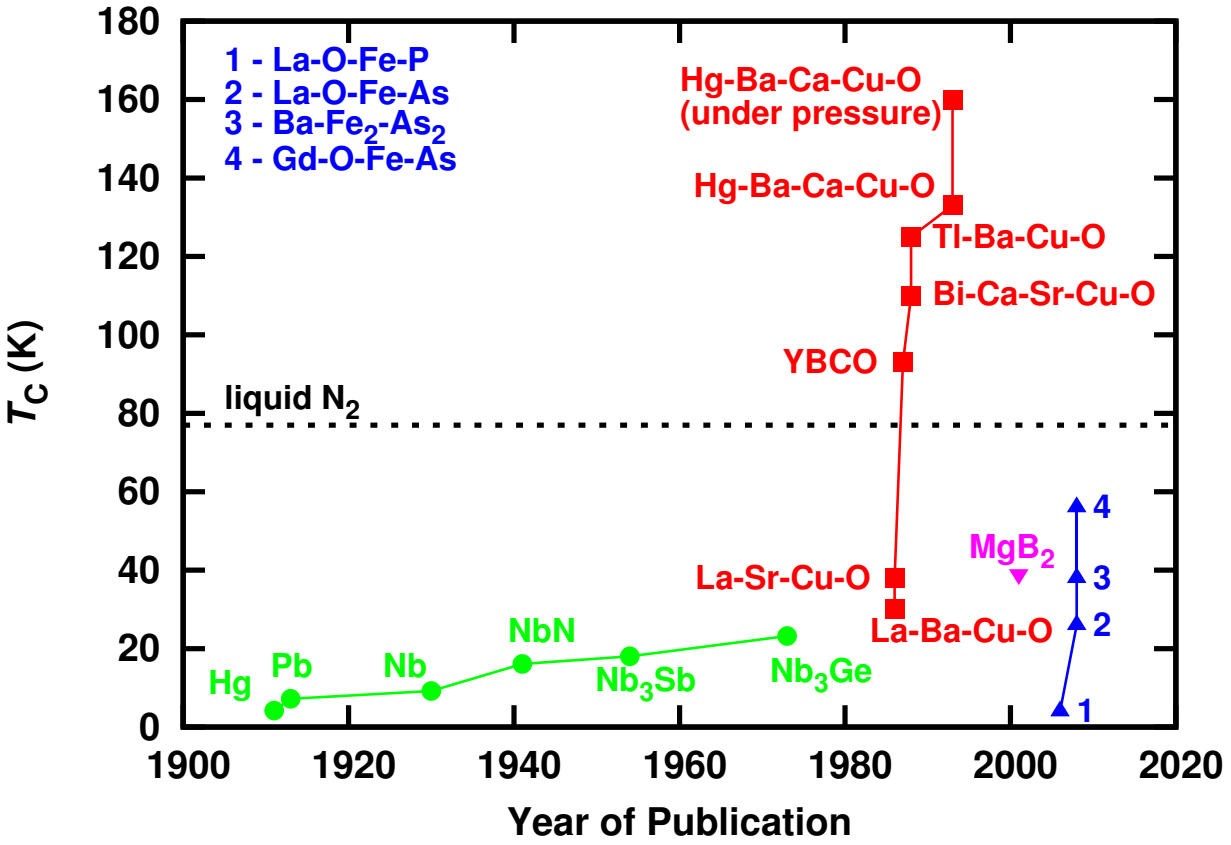

Figure 2.1: Timetable of some important superconductors, their year of discovery and their T_C. The dashed line shows the liquid nitrogen temperature as above this temperature cooling becomes rather easy and commercially available.

2.1 Zero Resistance

The first observation which lead to the discovery of superconductivity was the vanishing electrical resistance of mercury at the liquid helium temperature (∼4.2 K) (figure 2.2).

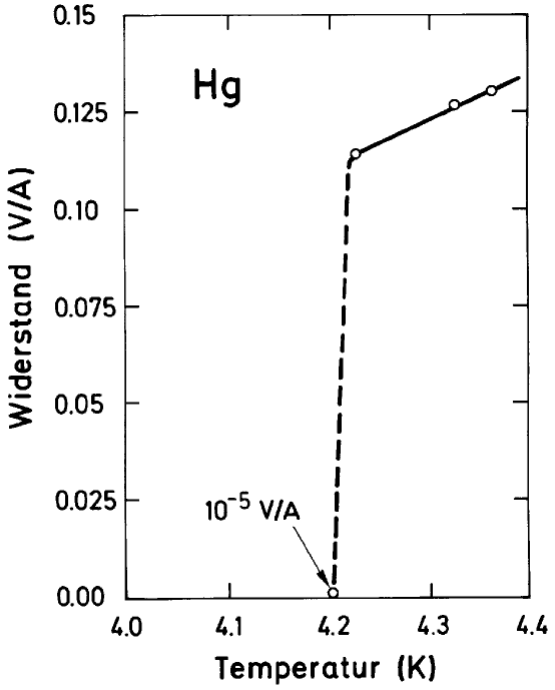

Figure 2.2: Resistance vs. Temperature measured by Heike Kammerlingh Onnes. At 4.2 K the resistance suddenly drops to values below 10^{-5} Ω [1].

In principal it is not known if the resistivity becomes zero or is just immeasurable close to zero. Onnes observed a decrease of electrical resistance down to values in the 10^{-5} Ω range. Of course, with this result it can not be said that the resistivity becomes zero. So he performed an experiment which gives much lower resistance values. He induced a current in a superconducting lead ring by a permanent magnet and observed the displacement of a magnetic needle. The displacement is caused by the magnetic field of the current inside the ring. If there would be an electrical resistance the current would decay exponentially following equation 2.1, where I(t) is the current at time t, I_0 the starting current, R the resistance and L the self-inductance.

$$I(t) = I_0 e^{-\frac{R}{L}t} \tag{2.1}$$

With this method Onnes gained resistance values below T_C in the range of 10^{-13} Ω [9]. More modern measurements reveal a small resistivity in the superconducting state of $\approx 10^{-23}$ Ωcm [10]. The difference in the resistivities of metals and superconductors in their superconducting state is as big as the difference of metals and insulators. This said, one can consider the resistivity of a superconductor as zero. This only applies for type I superconductors which will be addressed in a later section.

2.2 Meissner-Ochsenfeld Effect and evidence for a phase transition

As already stated above one important characteristic of a superconductor is its ideal diamagnetism. This effect is fundamental for superconductors and distinguishes between them and ideal but normal conductors. This was first time observed and described by Walter Meissner and Robert Ochsenfeld in 1933 [13]. They observed that a magnetic field applied to a superconductor is expelled from the bulk superconductor by reaching temperatures below T_C. That is independent of the temperature where the magnetic field is applied to the material. It is always $B = 0$ for $T < T_C$.

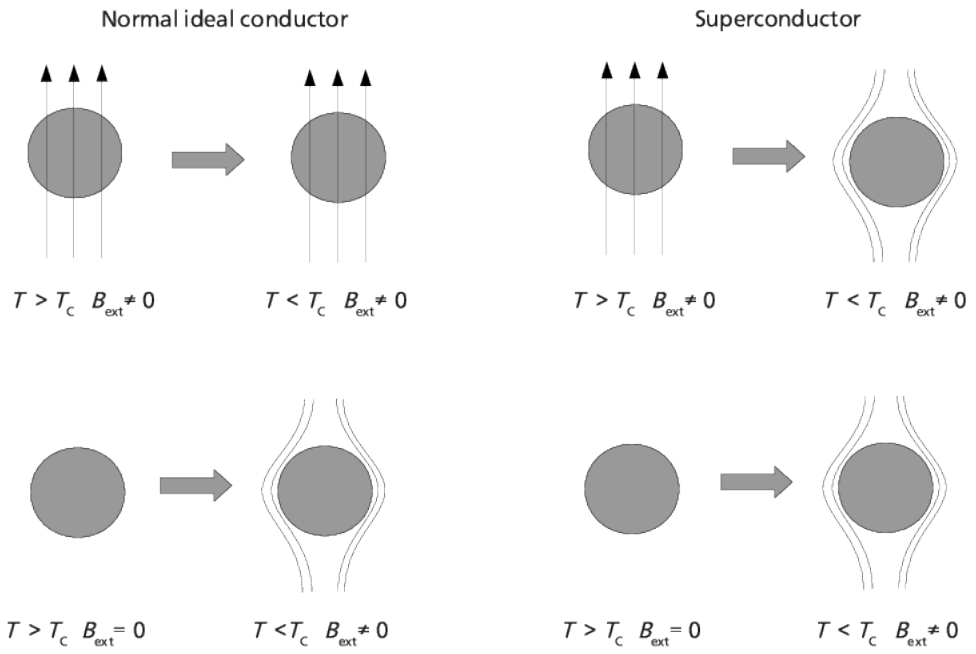

Figure 2.3: Comparison of flux penetration in a normal ideal conductor and a superconductor. On the left hand side the magnetic flux is shown for an ideal conductor, whereas the right hand side shows the case for a superconductor. It can be seen that for an ideal conductor it matters, if it is field cooled or zero-field cooled.

Figure 2.3 shows a comparison of the behaviour of a superconductor and an ideal conductor when exposed to an external magnetic field. It can be seen that for an ideal conductor there exist two different states for $T < T_C$ in dependency on field cooled or zero-field cooled scenario. For a zero-field cooled ideal conductor with $R = 0$, the magnetic field gets expelled from the bulk as soon as $B \neq 0$, i.e. the magnetic flux inside the bulk is zero. On the contrary, in the field cooled case the magnetic flux inside the bulk is not zero for $T < T_C$ and $R = 0$. So the final state of an ideal conductor depends on the history of the external magnetic field. The right hand side of figure 2.3 illustrates the superconductor and its behaviour with external magnetic fields. Here the final state for $T < T_C$ is always the same, no matter of the history of the magnetic field. This effect is

called the Meissner-Ochsenfeld effect and is the reason why a superconductor is an ideal diamagnet.

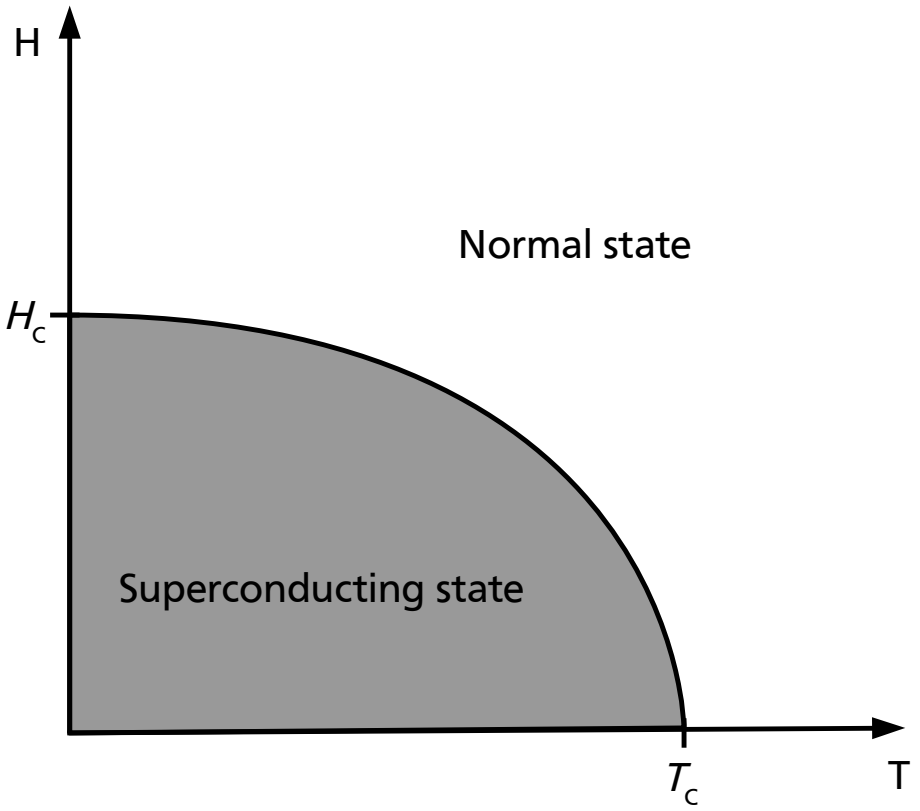

Figure 2.4: External magnetic field H vs. temperature T. The superconducting state can be destroyed either by raising temperature above T_C or by applying an external magnetic field above H_C. The upper critical field H_C is also a function of temperature.

This can also be seen as the presence of surface currents which induce a magnetization opposed to the external field. To keep the interior of a superconductor field free below T_C a small portion of energy is needed to create the surface currents. That means, with an external field high enough it is energetically more favorable to return to the normal state and let the external field penetrate the bulk material. This field is called upper critical field H_C and is a function of temperature (figure 2.4).

The difference in the behaviour of normal ideal conductor and superconductors exposed to an external magnetic field gives the impression of a thermodynamic phase transition at the boundary of normal conducting and superconducting state. An additional evidence for this impression can be found in the behaviour of the specific heat of a superconductor as a function of temperature. Figure 2.5 shows typical behaviour of a metals specific heat C_m and a typical superconductors specific heat C_S versus temperature. At T_C, C_S jumps to

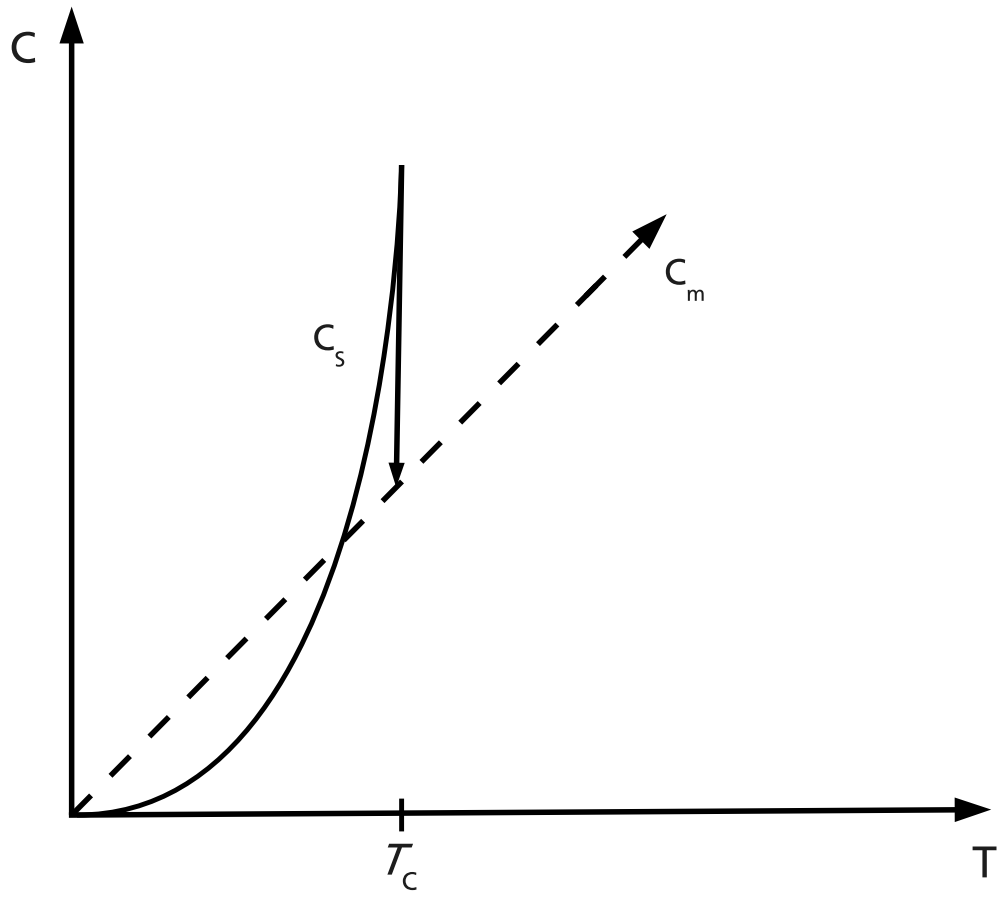

Figure 2.5: The variation of specific heat with temperature of a superconductor C_S and a normal metal C_m. Whereas the metals specific heat shows a continuous behaviour with temperature, the superconductor has a more exponential behaviour below T_C and a jump in specific heat at T_C.

much higher values which indicates a phase transition of second order. C_S can be described with an exponential behaviour as in equation 2.2.

$$C_S \sim exp(\frac{-B}{k_B T}) \tag{2.2}$$

Equation 2.2 already indicates an energy gap for the superconducting state, which will be described later in the BCS theory (section 2.6).

2.3 London equations

According to the Meissner-Ochsenfeld effect an external magnetic field is expelled completely from the interior of a superconductor. But there was experimental evidence that magnetic fields penetrate superconducting thin films. The first who described the Meissner-Ochsenfeld effect correctly were the London brothers [14]. For that they made the assumption that the electron move without friction through the material in the superconducting

state. With that the Drude theory for electrons is reduced by the friction term mv_D/τ (equation 2.3).

$$m\dot{v} = -eE \tag{2.3}$$

With $j_S = -en_s v$ the first London Equation can be derived (equation 2.4).

$$\frac{\partial j}{\partial t} = \frac{n_s e^2}{m} E \tag{2.4}$$

Using the Maxwell equation $\nabla \times E = -\dot{B}$, the behaviour of an ideal conductor can be described (equation 2.5).

$$\frac{\partial}{\partial t}\left(\frac{m}{n_s e^2}\nabla \times j_s + B\right) = 0 \tag{2.5}$$

But still with this equation the Meissner-Ochsenfeld effect can not be described. For that the constant of integration of equation 2.5 has to be zero. With that the second London Equation is derived (equation 2.6).

$$\nabla \times j_s = -\frac{n_s e^2}{m} B \tag{2.6}$$

The constant in the 1. and 2. London equation is now defined as $\lambda_L = \frac{m}{n_s e^2}$. So the London equation becomes

$$E = \lambda_L \dot{j_s} \tag{2.7a}$$
$$B = -\lambda_L \nabla \times j_s \tag{2.7b}$$

In addition to that the Maxwell equation (equation 2.8) can be applied.

$$\nabla \times H = j_s \Rightarrow \nabla \times B = \mu_0 j_s \tag{2.8}$$

For that the curl operator is applied to the Maxwell equation and combined with equation 2.7b

$$\nabla \times \nabla \times B = \mu_0 \nabla \times j_s = -\frac{\mu_0}{\lambda_L} B \tag{2.9a}$$
$$\nabla \times \nabla \times j_s = -\frac{1}{\lambda_L}\nabla \times B = -\frac{\mu_0}{\lambda_L} j_s \tag{2.9b}$$

Since $\nabla\times\nabla\times B = \text{grad}\,\text{div}\,B - \Delta B$ (where Δ is the Laplace operator), $\nabla\times\nabla\times j_s = \text{grad}\,\text{div}\,j_s - \Delta j_s$, $\text{div}\,B = 0$ and $\text{div}\,j_s = 0$ equations 2.9a and 2.9b become

$$\Delta B - \frac{\mu_0}{\lambda_L} B = 0 \tag{2.10a}$$

$$\Delta j_s = -\frac{\mu_0}{\lambda_L} j_s = 0 \tag{2.10b}$$

Equation 2.10a is an explanation for the Meissner-Ochsenfeld effect. Since $B(r) = B_0 = const.$ is not a valid solution for equation 2.10a (ΔB_0 is always zero, $\frac{\mu_0}{\lambda_L} B_0$ is never zero except $B_0 = 0$), there is no homogeneous magnetic field inside a superconductor. So in the superconducting state the only solution for equation 2.10a is a field which decreases exponentially inside the material.

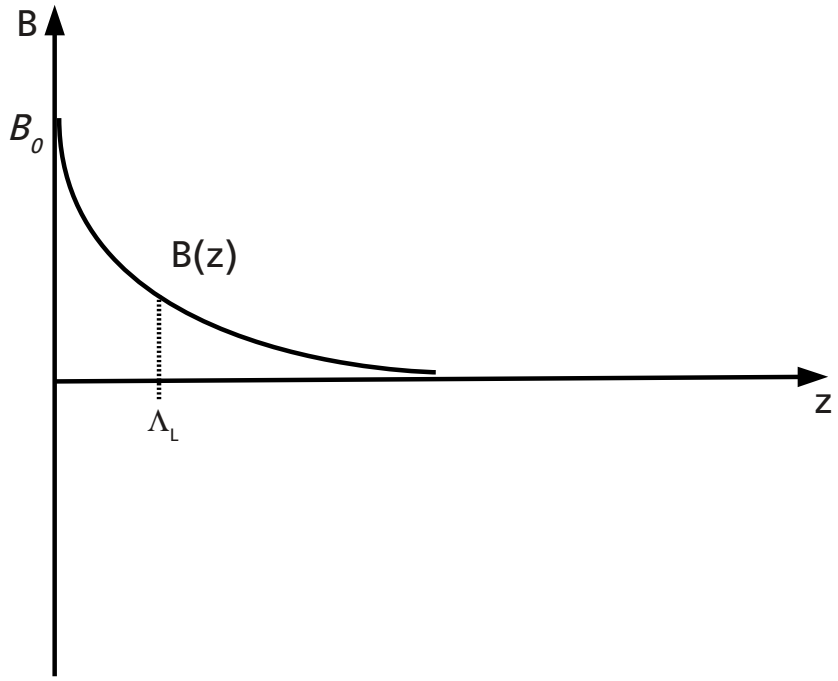

Figure 2.6: Exponential decay of an external magnetic field inside a superconducting material in its superconducting state. Λ_L is the distance from the surface where the field reaches a value of $\frac{1}{e}$.

This can be shown by considering an external magnetic field which is homogeneous and only in x-direction. Furthermore, it only can expand in z-direction. Then $\frac{\partial^2 B_x}{\partial z^2} - \frac{\mu_0}{\lambda_L} B_x = 0$ is

valid. Because of equation 2.8 is $j_s\ (0, j_{s,y}, 0)$ and it is $\frac{\partial^2 j_{s,y}}{\partial z^2} - \frac{\mu_0}{\lambda_L} j_{s,y} = 0$. Solutions for these equations are shown in equation 2.11.

$$B_x = B_x^0 \exp\left(-\sqrt{\frac{\mu_0}{\lambda_{L,z}}}\right) = B_x^0 \exp\left(-\frac{z}{\Lambda_L}\right) \tag{2.11a}$$

$$j_{s,y} = j_{s,y}^0 \exp\left(-\sqrt{\frac{\mu_0}{\lambda_{L,z}}}\right) = j_{s,y}^0 \exp\left(-\frac{z}{\Lambda_L}\right) \tag{2.11b}$$

The factor $\Lambda_L = \sqrt{\frac{m}{\mu_0 n_s e^2}}$ is the London penetration depth with m for electron mass and n_s for the density of the superconducting charge carriers. At this distance from the surface the external magnetic field reaches a value of $\frac{1}{e}$ (figure 2.6). Table 2.1 shows typical values for Λ_L in nm.

Table 2.1: Calculated London penetration depth values at absolute zero [15].

Metal	Λ_L in nm
Sn	34
Al	16
Pb	37
Cd	110
Nb	39

For a thin film with the thickness d much less than Λ_L, the situation is a little bit different. Because of the much bigger penetration depth compared to the materials thickness an external magnetic field will not decay completely. Thus, the energy brought to the system by the magnetic field is not enough to destroy superconductivity. That means, for thinner films the critical magnetic field will be higher (figure 2.7).

Equation 2.11b shows that not only the magnetic field decreases from the surface but also the current density.

2.4 Type I and Type II superconductors

With the considerations of the behaviour of a superconducting thin film in an external magnetic field, it is possible to take a look at different types of superconductors. If it can be assumed that a superconductor can be separated into thin alternating layers of normal state and superconducting state, it can be concluded that a superconductor build like that can stand higher critical fields. This assumption is found experimentally and split superconductors into two different types: type I and type II superconductors.

For type I superconductors there is one specific critical field H_C. Above H_C superconductivity is destroyed (figure 2.8 on the left, dashed line). Mostly elemental and pure materials show this type of superconductivity. These also called soft superconductors usually have small values of H_C. As a consequence they are not suitable for applications in superconducting magnets.

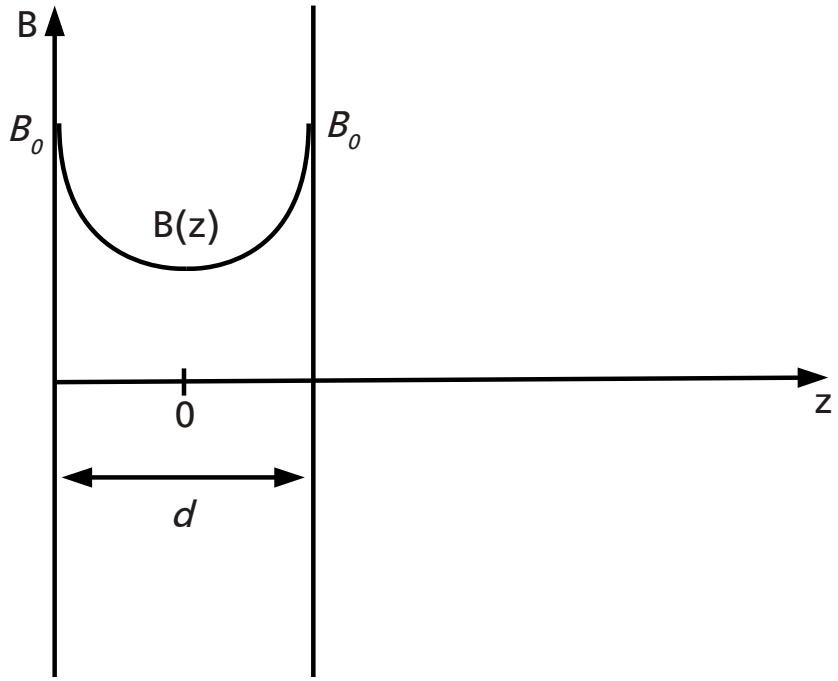

Figure 2.7: External magnetic field inside a superconducting thin film. Λ_L is much bigger than the film thickness d so the magnetic field does not decay completely.

Type II superconductors show a different behavior. They have a lower critical field H_{C1} and an upper critical field H_{C2} (figure 2.8 on the left, solid line). Below H_{C1} the behavior is similar to the type I superconductors. Above H_{C1} the magnetic flux starts to penetrate the superconductor. A hybrid configuration arises where superconducting and normal conducting areas exists side by side. In the so called Shubnikov-phase magnetic flux vortices were formed. Inside these vortices the normal conducting state is present whereas outside, the superconducting state is still stable (figure 2.8 on the right). The external magnetic field has to reach H_{C2} to destroy superconductivity. Type II superconductors are also called "hard superconductors" because of their very high H_{C2} ($> 20\,\mathrm{T}$)[15]. They are used for coils in superconducting magnets, e.g. for magnetic resonance imaging. Most of the superconducting compounds that show a type II behavior are alloys or impure materials.

2.5 Flux-Quantization

Already in 1950, Fritz London predicted a quantized magnetic flux passing through a superconductor. Thus the magnetic flux in a superconducting ring is equal to a multiple of one flux quantum $\Phi_0 = \frac{\hbar}{2e}$. In 1961, Doll and Näbauer [16] observed this behavior in one of their experiments (Figure 2.9). They used a small lead cylinder to generate the flux quantums. For that, a magnetic field B_e parallel to the cylinder axis was applied above T_C

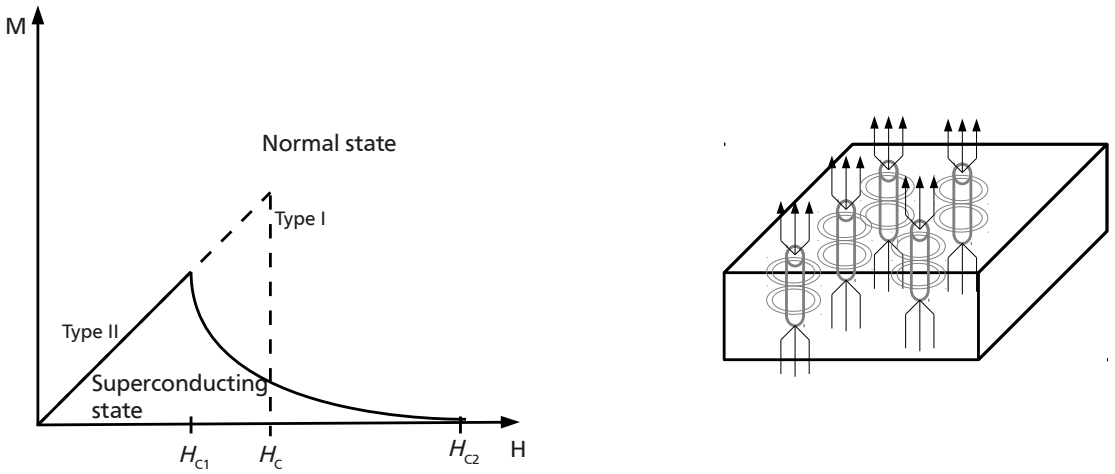

Figure 2.8: Left: Internal magnetization of a superconductor versus an external magnetic field. Shown are a superconductor type I (dashed line) and a superconductor type II (solid line). It can be seen that the internal magnetization for a type I superconductor is bigger but the upper critical field H_C is smaller. In comparison the type II superconductor has a lower magnetization but two different critical fields. At H_{C1} the external magnetic field starts to penetrate the superconductor but does not destroy superconductivity because areas with normal state and superconducting states are built (so called vortices, see picture on the right). Only fields above H_{C2} are capable of destroying superconductivity.

and then switched off after the superconducting state was reached. Thus a supercurrent was generated inside the lead ring. Now a measuring field B_M perpendicular to the ring was generated. This results in a torque and the ring, which hangs at a quartz fiber, starts to move. Doll and Näbauer used this movement to generate an oscillation. At its resonance frequency the amplitudes are big enough to be detected. The detection was done with an attached mirror and a laser. The resonance amplitude is proportional to the measuring field. Figure 2.10 depicts the experimental results of Doll and Näbauer. This diagram shows several steps for the resonance amplitude instead of a linear behavior, which proofs the flux quantization.

2.6 The BCS-Theory

The phenomenon of the superconducting state and its fundamental difference to any normal metallic state suggests a phase transition. A phase transition is always accompanied by an instability of the normal state. Cooper was the first who suggested a weak attractive interaction of two electrons as a reason for a collapse of the electron gas [17]. Fröhlich already discussed a phonon mediated interaction of two electrons [18].

His explanation of an attractive interaction of two negative charges which should interact repulsively was the effect of a moving electron through the positively charged crystal lattice of a solid. The negative electron interacts with the positive ions of the lattice in such a way that it moves the ions out of its position. Since the electron velocity on its path through

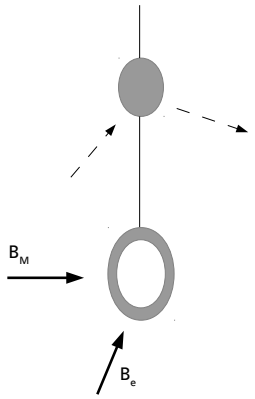

Figure 2.9: Experimental setup used by Doll and Näbauer. They used a superconducting ring in two perpendicular magnetic fields and measured the response via a laser and a mirror.

the lattice is much higher than the vibration frequency of the positive lattice ions and a path of higher positive charge density forms. Another electron now is attracted by this high density of positive charges and take for its movement through the lattice this exact path (in opposite direction) without seeing the Coulomb force of the other electron. The distance of these two electrons can be estimated by the Fermi velocity for the electrons $v_F \approx 10^8$ cm/s and the phonon periodic time $\tau \sim \frac{2\pi}{\omega_D} \approx 10^{-13}$ s. This is a distance of ≈ 1000 Å. This large distance also explains the negligible Coulomb repulsion which is simply shielded.

The ground state of the non-interacting Fermi gas is defined as all electronic states with $E < E_F$ are occupied whereas the states above E_F are unoccupied. If now two electrons would be added to this system and thus occupy states above E_F they can interact through phonons as stated above.

This phonon interaction is limited by two quantum mechanical boundary conditions. First of all the conservation principle has to be obeyed (equation 2.12).

$$\mathrm{K} = \mathrm{k}_1 + \mathrm{k}_2 \tag{2.12}$$

Furthermore, the interaction is limited to an energy range $\hbar\omega_D$ which ends up in an energy shell of the thickness Δk. These two boundary conditions combined lead to only a few states at the overlap of the two spheres which are allowed to scatter into (figure 2.12). For $\mathrm{K} = 0$ the attractive interaction becomes strongest and thus $\mathrm{k}_1 = -\mathrm{k}_2$ is most important, meaning electrons with opposite spin interact.

Since now the reason for the instability of the normal state is known, it is necessary to determine the energy of this new phase. As discussed above the electron pairing only occurs above the Fermi energy. That means, the kinetic energy of the system increases:

$$E_{\mathrm{kin}} = 2\sum_{\mathrm{k}} \omega_{\mathrm{k}} \xi_{\mathrm{k}} \tag{2.13}$$

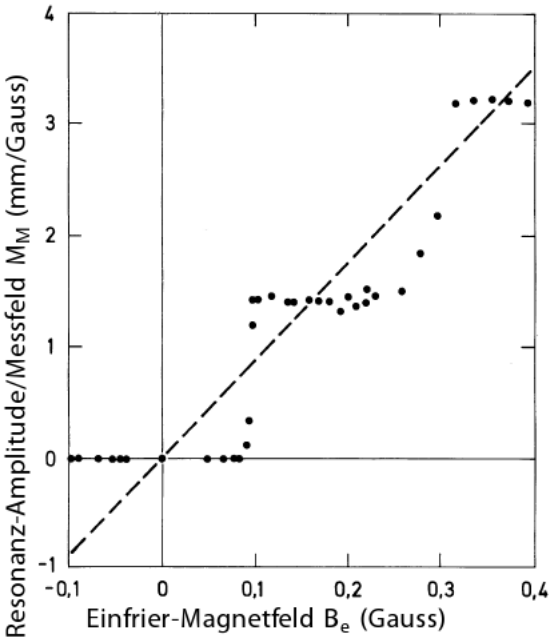

Figure 2.10: Experimental results discovered by Doll and Näbauer showing the flux quantization. It can be clearly seen that the results do not show a linear behaviour but discrete jumps with factor 2 [16].

where ω_k is the probability that a pair state is occupied and ξ_k is the energy of one particle related to the Fermi energy and defined as

$$\xi_k = \frac{\hbar^2 k^2}{2m} - E_F \tag{2.14}$$

Beside the kinetic energy part of the system there is also a potential part which decreases the systems energy and comes from the scattering of a cooper pair $(k\uparrow, -k\downarrow) \leftrightarrows (k'\uparrow, -k'\downarrow)$, i.e. annihilation and simultaneous creation of a pair. A state k can either be occupied or unoccupied:

$$|1\rangle_k \text{ if } (k\uparrow, -k\downarrow) \text{ occupied} \tag{2.15a}$$
$$|0\rangle_k \text{ if } (k\uparrow, -k\downarrow) \text{ unoccupied} \tag{2.15b}$$

That means in general the state can be described as

$$|\Psi\rangle = u_k|0\rangle_k + v_k|1\rangle_k \tag{2.16}$$

Here is $u_k^2 = 1 - \omega_k$ (probability that a state is unoccupied) and $v_k^2 = \omega_k$ (probability that a state is occupied), $u_k, v_k \in \Re$. With that the BCS state, which is the product of the states of all pairs, can be written as

$$|\phi_{BCS}\rangle \simeq \prod_k (u_k|0\rangle_k + v_k|1\rangle_k) \tag{2.17}$$

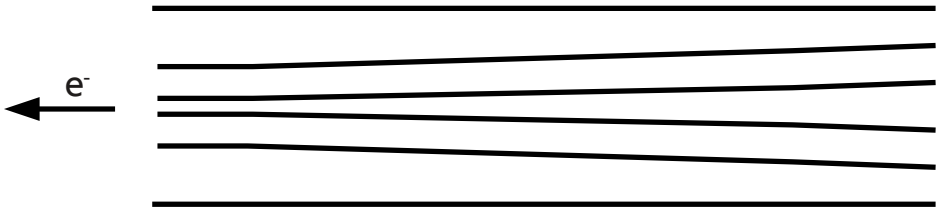

Figure 2.11: Schematic of an electron moving through a crystal lattice of a solid. The negatively charged electron leaves a path of higher density of positively charged lattice ions. This higher density of positive charges can be "seen" by another electron and will be used as a path in opposite direction of the first electron [11].

Here the assumption is that the pairs do not interact or rather their interaction can be neglected. In two dimensions the occupied and unoccupied state can be described as

$$|1\rangle_{\mathrm{k}} = \begin{pmatrix} 1 \\ 0 \end{pmatrix}_{\mathrm{k}} \tag{2.18a}$$

$$|0\rangle_{\mathrm{k}} = \begin{pmatrix} 0 \\ 1 \end{pmatrix}_{\mathrm{k}} \tag{2.18b}$$

or as Pauli matrix

$$\sigma_{\mathrm{k}}^{+} = \frac{1}{2}(\sigma_{\mathrm{k}}^{1} + i\sigma_{\mathrm{k}}^{2}) = \begin{pmatrix} 0 & 1 \\ 0 & 0 \end{pmatrix} \tag{2.19a}$$

$$\sigma_{\mathrm{k}}^{-} = \frac{1}{2}(\sigma_{\mathrm{k}}^{1} - i\sigma_{\mathrm{k}}^{2}) = \begin{pmatrix} 0 & 0 \\ 1 & 0 \end{pmatrix} \tag{2.19b}$$

where σ_{k}^{+} and σ_{k}^{-} describe the creation and the annihilation of the state $(\mathrm{k}\uparrow, -\mathrm{k}\downarrow)$. While the scattering process $(\mathrm{k}\uparrow, -\mathrm{k}\downarrow) \rightarrow (\mathrm{k}'\uparrow, -\mathrm{k}'\downarrow)$ the energy of the system is reduced by $V_{\mathrm{kk}'}$. This is usually assumed as constant and will be called V_0. In the Pauli matrix this process is represented by the operators $\sigma_{\mathrm{k}'}^{+}, \sigma_{\mathrm{k}}^{-}$. The whole energy reduction is the sum of all pair scatterings

$$V = -\frac{V_0}{L^3} \sum_{\mathrm{kk}'} \sigma_{\mathrm{k}'}^{+}, \sigma_{\mathrm{k}}^{-} \tag{2.20}$$

where L^3 is the scaling volume of the crystal. Thus the reduction of the potential energy is given by the eigenvalue of V in the state of $|\phi_{\mathrm{BCS}}\rangle$

$$\langle\phi_{\mathrm{BCS}}|V|\phi_{\mathrm{BCS}}\rangle = -\frac{V_0}{L^3}\left\{\prod_p (u_p\langle 0| + v_p\langle 1|) \sum_{\mathrm{kk}'} \sigma_{\mathrm{k}}^{+}\sigma_{\mathrm{k}'}^{-} \prod_q (u_q|0\rangle + v_q|1\rangle_q)\right\} \tag{2.21}$$

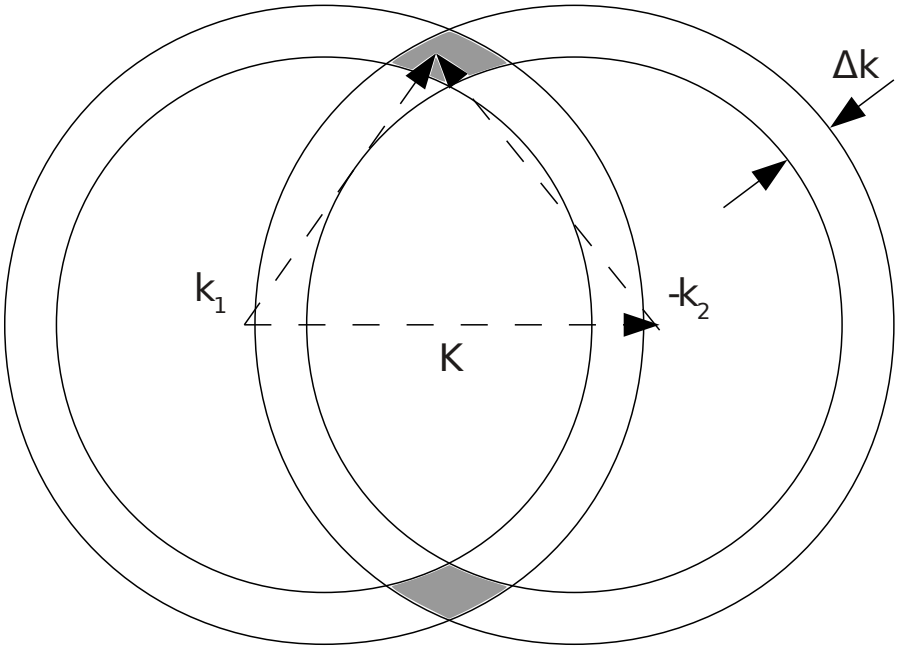

Figure 2.12: Electron pair scattering with $\mathrm{K} = \mathrm{k}_1 + \mathrm{k}_2 = \text{const}$. The shell of the Fermi sphere has the thickness $\Delta\mathrm{k}$. The states which the electron pairs can scatter into are marked.

In addition it is ${}_{\mathrm{k}}\langle 1|1\rangle_{\mathrm{k}} = 1$, ${}_{\mathrm{k}}\langle 0|0\rangle_{\mathrm{k}} = 1$, ${}_{\mathrm{k}}\langle 1|0\rangle_{\mathrm{k}} = 0$ and thus

$$\langle \phi_{\mathrm{BCS}}|V|\phi_{\mathrm{BCS}}\rangle = -\frac{V_0}{L^3}\sum_{\mathrm{kk'}} v_{\mathrm{k}} u_{\mathrm{k}} v_{\mathrm{k'}} u_{\mathrm{k'}} \tag{2.22}$$

Combination of the kinetic energy and of the potential energy of the BCS system gives the total energy of the Cooper pair system:

$$W_{\mathrm{BCS}} = 2\sum_{\mathrm{k}} v_{\mathrm{k}}^2 \xi_{\mathrm{k}} - \frac{V_0}{L^3}\sum_{\mathrm{kk'}} v_{\mathrm{k}} u_{\mathrm{k}} v_{\mathrm{k'}} u_{\mathrm{k'}} \tag{2.23}$$

The BCS ground state at $T = 0$ K is given by a minimum W_{BCS}^0 of W_{BCS}. This can be calculated because of the relation of v_{k} and u_{k}

$$\left.\begin{aligned} v_{\mathrm{k}} &= \sqrt{\omega_{\mathrm{k}}} \\ u_{\mathrm{k}} &= \sqrt{1-\omega_{\mathrm{k}}} \end{aligned}\right\} \Rightarrow \sqrt{1 - v_{\mathrm{k}}^2} = u_{\mathrm{k}} \tag{2.24}$$

This is equal to

$$v_k^2 + u_k^2 = 1 = \cos^2\theta_k + \sin^2\theta_k \Rightarrow \begin{cases} v_k = \cos\theta_k \\ u_k = \sin\theta_k \end{cases} \tag{2.25}$$

Now, to get the minimum in equation 2.17, v_k and u_k are substituted with equation 2.25 and θ_k is minimized:

$$\begin{aligned} W_{BCS} &= \sum_k 2\xi_k \cos^2\theta_k - \frac{V_0}{L^3}\sum_{kk'} \cos\theta_k \sin\theta_{k'} \cos\theta_{k'} \sin\theta_k \\ &= \sum_k 2\xi_k \cos^2\theta_k - \frac{V_0}{L^3}\sum_{kk'} \frac{1}{4}\sin 2\theta_k \sin 2\theta_{k'} \end{aligned} \tag{2.26}$$

To get the minimum, $\frac{\partial W_{BCS}}{\partial \theta_k}$ has to be 0:

$$\frac{\partial W_{BCS}}{\partial \theta_k} = 0 = -4\xi_k \cos\theta_k \sin\theta_k - \frac{V_0}{L^3}\sum_{k'} \cos 2\theta_k \sin 2\theta_{k'} \tag{2.27}$$

$$\xi_k \tan 2\theta_k = -\frac{V_0}{2L^3}\sum_{k'} \sin 2\theta_{k'} \tag{2.28}$$

Now two factors are introduced, Δ and E_k:

$$\Delta = \frac{V_0}{L^3}\sum_{k'} u_{k'} v_{k'} = \frac{V_0}{L^3}\sum_{k'} \sin\theta_{k'} \cos\theta_{k'} \tag{2.29}$$

$$E_k = \sqrt{\xi_k^2 + \Delta^2} \tag{2.30}$$

Because of trigonometric relations, it is valid:

$$\frac{\sin 2\theta_k}{\cos 2\theta_k} = \tan 2\theta_k = -\frac{\Delta}{\xi_k} \tag{2.31}$$

$$2u_k v_k = \sin 2\theta_k = \frac{\Delta}{E_k} \tag{2.32}$$

$$v_k^2 - u_k^2 = -\frac{\xi_k}{E_k} \tag{2.33}$$

With that it is possible to calculate the probability of an occupied state w_k at $T = 0$ K:

$$w_k = v_k^2 = \frac{1}{2}\left(1 - \frac{\xi_k}{E_k}\right) = \frac{1}{2}\left(1 - \frac{\xi_k}{\sqrt{xi_k^2 + \Delta^2}}\right) \tag{2.34}$$

To get the energy of the superconducting BCS ground state W^0_{BCS}, the equations 2.31–2.34 have to be combined with equation 2.26:

$$W^0_{\mathrm{BCS}} = \sum_{\mathrm{k}} \xi_{\mathrm{k}} \left(1 - \frac{\xi_{\mathrm{k}}}{E_{\mathrm{k}}}\right) - L^3 \frac{\Delta^2}{V_0} \tag{2.35}$$

If now the energy of the BCS ground state W^0_{BCS} and the energy of the normal state, i.e. the energy of the Fermi sea without attractive interaction $W^0_{\mathrm{n}} = \sum_{|\mathrm{k}|<\mathrm{k_F}} 2\xi_{\mathrm{k}}$ are compared, it is possible to determine the condensation energy for the superconducting phase:

$$\frac{W^0_{\mathrm{BCS}} - W^0_{\mathrm{n}}}{L^3} = -\frac{1}{L^3} \sum_{\mathrm{k}} \xi_{\mathrm{k}} \left(1 + \frac{\xi_{\mathrm{k}}}{E_{\mathrm{k}}}\right) - \frac{\Delta^2}{V_0} \approx -\frac{1}{2} Z(E_{\mathrm{F}}) \Delta^2 < 0 \tag{2.36}$$

Equation 2.36 can be interpreted as $Z(E_{\mathrm{F}})\Delta$ electron pairs per volume condensate into a state Δ below E_{F}. Through this one electron gains an average energy of $\frac{\Delta}{2}$. This means the formation of superconductivity reduces the ground state energy. Through similar calculations as above it can be shown that the energy which is needed to break a cooper pair and thus destroy the superconducting state is 2Δ.

The BCS-theory by John Bardeen, Leon N. Cooper and John R. Schrieffer [2, 19] explains the quantum mechanical effects of superconductivity very well and was awarded with the Physics Nobel price in 1972. However, a universal theory for explaining the observed unconventional superconductivity in cuprates and pnictides is still eluding.

3 Iron-pnictides: A novel class of superconductors

For more than 20 years cuprates were the only high temperature superconductors. This changed when Kamihara *et al.* [5] published a report about a fluorine doped iron pnictide with a T_C as high as 26 K in 2008. This discovery led to high research activity all over the world and soon many other compounds and structures with the maximum T_C as high as 56 K were found [6]. In table 3.1 an overview about some important compounds and their transition temperatures are given.

Table 3.1: Some transition temperatures for the most important compounds of the newly discovered iron based superconductors.

Compound	T_C (K)	References
$LaFeAsO_{0.89}F_{0.11}$	26	[5]
$CeFeAsO_{0.85}$	46.5	[20]
$NdFeAsO_{1-y}$	54	[21]
$SmFeAsO_{1-x}F_x$	55	[22]
$Gd_{0.8}Th_{0.2}FeAsO$	56.3	[6]
$Ba_{0.6}K_{0.4}Fe_2As_2$	38	[23]
$Sr_{0.6}K_{0.4}Fe_2As_2$	35.6	[24, 25]
KFe_2As_2	3.8	[24]
LiFeAs	18	[26–28]
FeSe	8	[29]

Another important factor of a superconductor beside its transition temperature is the upper critical magnetic field H or for a type II superconductor it is H_{c2}. It turned out that pnictide superconductors are not only type II but also exhibit rather high H_{c2} values $\gg 40$ T. Table 3.2 shows some values of the upper critical magnetic field of important pnictide compounds.

As it can already be seen from the tables 3.1 and 3.2 there is a huge variety of different structures and compositions which contain Fe and As (or chalcogenides like Se) and become superconducting. Remarkable is the layered appearance of the structure which is remindful of the layered cuprates. The structure consists of alternating FeAs and charge reservoir layers along the *c*-axis. The ferromagnetic Fe in the structure should also be mentioned, since it was thought that iron containing materials could not show such an extraordinary high T_C. So far, only transition temperatures below 10 K were observed in Fe containing compounds, e.g. $Lu_2Fe_3Si_5$ ($T_C = 6.1$ K) [39] or U_6Fe ($T_C = 3.9$ K) [40]. In fact, iron itself can become superconducting under pressures of 20 GPa and below temperatures of 1.8 K [41]. However, the discovery of Kamihara *et al.* was groundbreaking not only because of the fact of iron inside the structure and the high T_C but also for the wide range

Table 3.2: Some values for upper critical fields for some pnictide superconductors measured parallel and perpendicular to the *ab*-plane at the specified temperature.

Compound	T_C (K)	T (K)	$H_{c2,c}$ (T)	$H_{c2,ab}$	Ref.
$NdFeAsO_{0.7}F_{0.3}$	47	35	9	54	[30]
$Ba_{0.55}K_{0.45}Fe_2As_2$	32	14	57	68	[31]
$Ba_{0.6}K_{0.4}Fe_2As_2$	28.2	10	56	57	[32]
$Ba(Fe_{0.92}Co_{0.08})_2As_2$	22.1	1	50	53	[33]
$Ba(Fe_{0.9}Co_{0.1})_2As_2$	22	10	41	25	[34, 35]
$Sr(Fe_{0.9}Co_{0.1})_2As_2$	20	1	46	46	[36]
LiFeAs	18	1	72	83	[37]
$FeSe_{0.5}Te_{0.5}$	14.5	10	32	31	[38]

of research activities all over the world which led to a drastic increase in T_C by a factor of two within six month time.

One of the important features of the iron pnictide superconductors is their semimetal nature in the normal state revealed by band structure calculations and angle-resolved photoemission spectroscopy (ARPES) [42]. This directly influences the carrier concentrations of undoped FeAs compounds which is roughly an order of magnitude smaller compared to those of a conventional metal.

The following chapter gives a brief introduction to this new class of high T_C superconductors. Because of the variety of different types and structures this chapter will concentrate on the four most important compounds.

3.1 The '1111' compounds

One of the most important structures in the field of iron based superconductors and at the same time the first one to be discovered is the so called '1111' structure, named after its stoichiometry. The first discovery of superconductivity in this ZrCuSiAs-type structure [44] was in 2006 by Kamihara *et al.* [45] in $LaFeP_{1-x}F_x$ with a T_C of 5 K. But only the discovery of isostructural $LaFeAsO_{1-x}F_x$ with T_C up to 26 K for $x \sim 0.11$ has started intense research on that novel class of superconducting compounds [5]. Soon after the discovery of the superconducting nature of $\mathbf{LaFeAsO_{1-x}F_x}$ many more compounds were found just by replacing the lanthanum by various rare earth elements. Figure 3.2 gives a brief overview of the discoveries and the increase of T_C within a few months. So far, the record in T_C was reported by Wang *et al.* [6] with a T_C of 56.3 in $Gd_{0.8}Th_{0.2}FeAsO$.

Figure 3.1a shows the crystal structure of 1111-type *RE*FeAsO compounds where *RE* is a rare earth element, e.g. lanthanum. It has a tetragonal crystal system with space group 129 (*P4/nmm*). As most of the pnictide superconductors this structure contains FeAs layers. These layers alternate with *RE*O layers which act as charge reservoir. Thus, doping in this layer by oxygen vacancies (e.g. $NdFeAsO_{1-y}$) or doping on the oxygen side (e.g. fluorine doping) lead to superconductivity. Later it was found, that doping by oxygen vacancies was a doping by partial substitution of oxygen by hydrogen [46]. Of course, it is also possible to dope on the rare earth side as in $Gd_{0.8}Th_{0.2}FeAsO$, which holds the T_C record in pnictide superconductors so far. There are also reports on doping

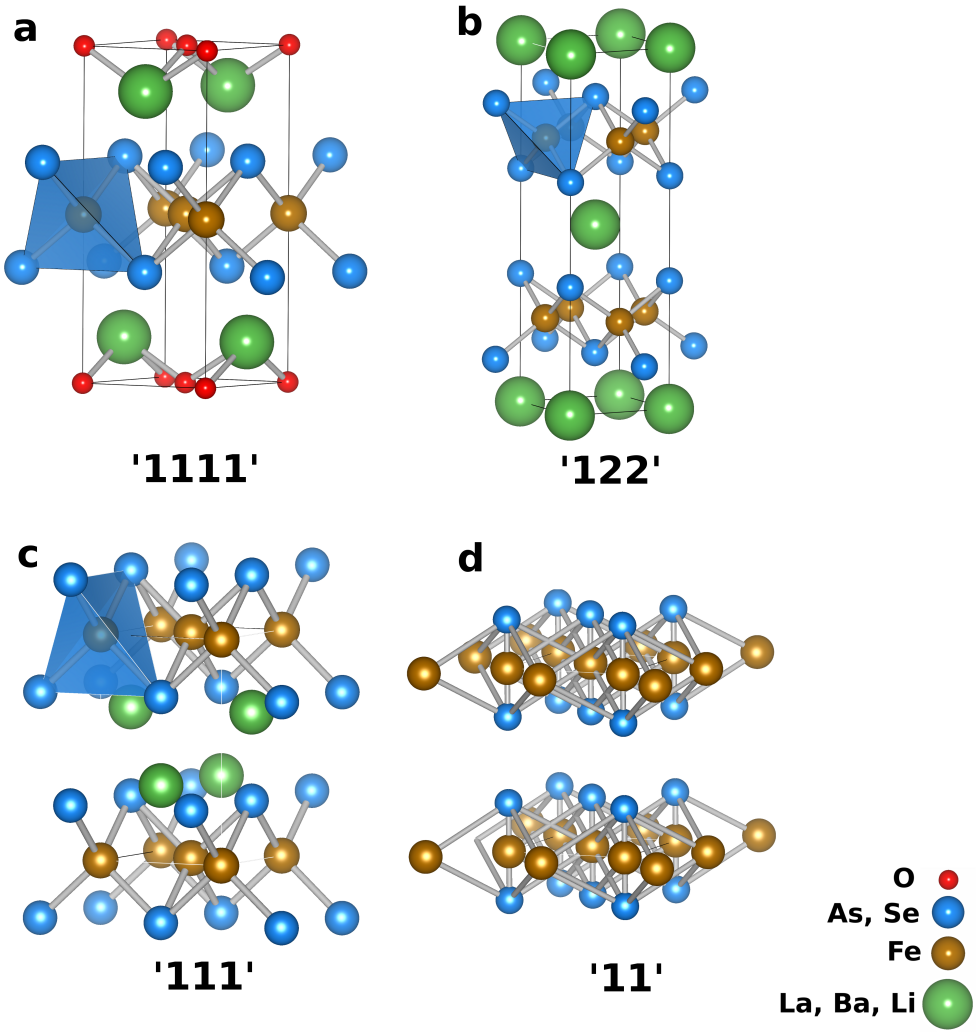

Figure 3.1: Crystal structure of a) '1111'-type REFeAsO, b) '122'-type $BaFe_2As_2$, c) '111'-type LiFeAs and d) '11'-type FeSe superconductor.

on the metal site in $A(Fe_{1-x}Co_x)AsF$ (A = Ca or Sr) with maximum T_C of 22 K and 4 K, respectively [47, 48]. The undoped compounds are non-superconducting antiferromagnets with a T_N of $\sim$ 150 K and show poor metallic behaviour [49]. Notable is a structural distortion from the tetragonal to an orthorhombic system which occurs below temperatures of 140 K. The transition of the normal state system to the distorted system can also be seen in resistivity versus temperature measurements and in magnetic susceptibility measurements. The transition occurs as a kink in the measurement curves [50]. In the case of the resistivity measurement the reason for the kink is a spin density wave (SDW) affecting the electrical properties of the compound. The magnetic measurement reveals a antiferromagnetic ordering of the system when the structural transition occurs. By doping this transition is suppressed. Superconductivity only occurs in the tetragonal system which can be achieved by doping. Figure 3.3 shows a schematic of the temperature versus doping level phase diagram. As it can be seen, at low doping levels and above the structural transition temperature T_S the compound is in a paramagnetic state with tetragonal crystal structure and poor metallic behaviour. Decreasing the temperature below T_S results in the mentioned structural transition from tetragonal to orthorhombic crystal system. A further

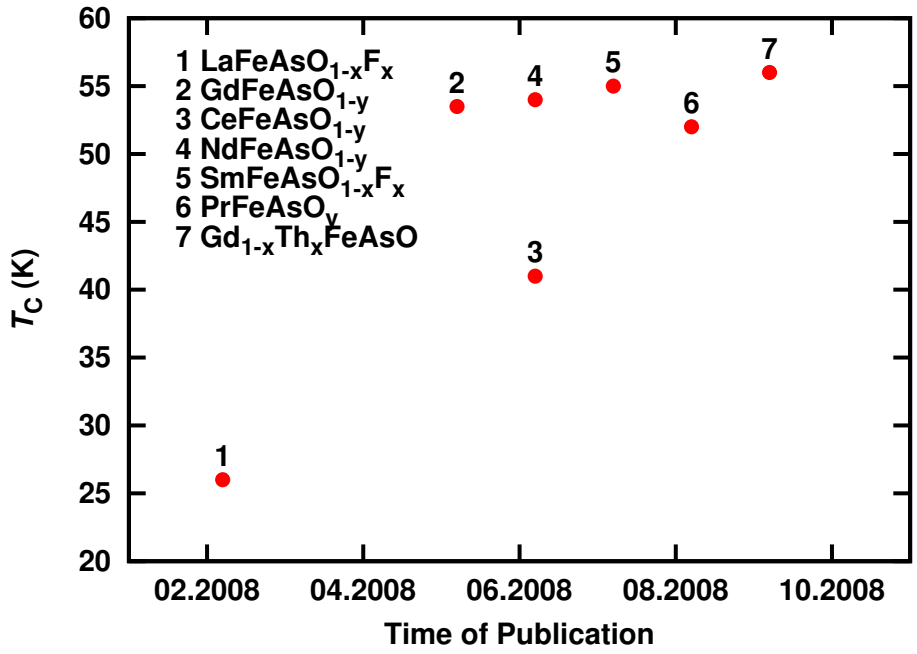

Figure 3.2: Timetable of the discovery of various '1111'-type superconductors and their T_C's.

reduction below T_N leads to the antiferromagnetic ordering. Only by doping the structural transition and the antiferromagnetic ordering at lower temperatures can be suppressed and superconductivity occurs. The dependence of superconductivity versus doping level has a dome like shape as it is known from cuprate superconductors. Also notable about this new class of superconductors is the presence of two different anions in one structure. In this case it is arsenic which is in the -3 valence state and oxygen which is in the -2 valence state.

As it can be seen in figure 3.1a the iron and the arsenic form a $FeAs_4$ tetrahedron. These tetrahedra are regular (all faces are equilateral triangles) if the As-Fe-As bond angle is 109.47°. The angle can be determined by the unit cell size assuming a constant Fe-As distance. Since the unit cell size is dependent of the rare earth element (for '1111'-type) inside the structure with substitution of the rare earth side, the angle can be manipulated. The rare earth substitution with Gd gives the "perfect" angle of 109.47°. This compound also gives the highest T_C. So the tetrahedron angle seems to be crucial for superconductivity [51]. This also influences the symmetry of the gap function [52]. Kuroki *et al.* [53] discussed the nature of the gap symmetry, nodal versus fully gapped. They assume a function of the height of the As above the iron plane, i.e a small height (e.g. in LaFePO) favours a nodal behaviour whereas a large height (e.g. in $LaFeAsO_{1-x}F_x$) is fully gapped.

Taking a look at the Fe-Fe spacing reveal a rather short distance of 2.85 Å for the '1111'-type[54] which ensures the 3*d* Fe electrons take part in the band formation and dominate the rather large density of states near the Fermi energy [55].

Another important question is the pairing of the Cooper pair orbital angular momentum. NMR measurements revealed a spin singlet behaviour [56]. That means the Cooper pair orbital angular momentum should correspond to either *s*-wave or *d*-wave pairing. Josephson junction experiments suggest an s-wave pairing [57]. The pairing mechanism for the Cooper pairs itself is still unclear. Comparable to the cuprate superconductors the conventional BCS theory does not give a satisfying answer to the rather high T_C.

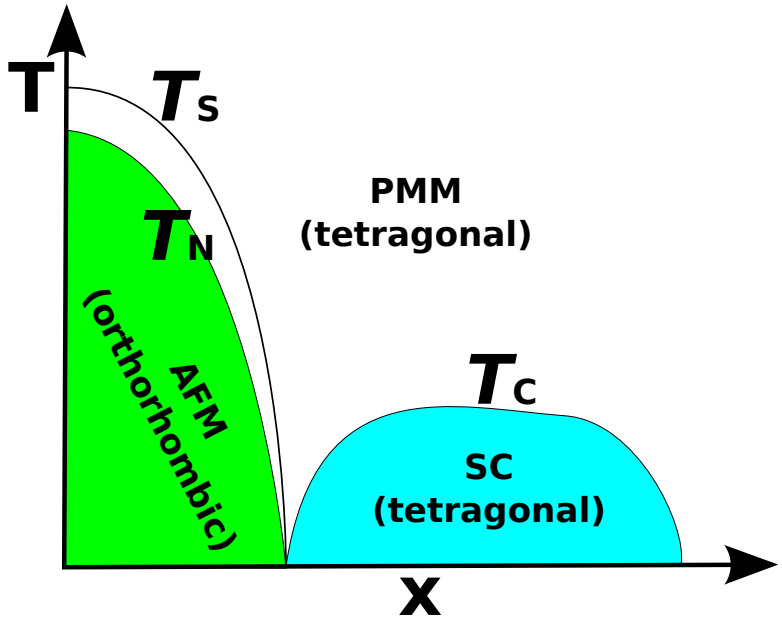

Figure 3.3: Schematic phase diagram of the '1111'-type iron based superconductors. It is shown temperature T versus various doping contents x. The different states of this compounds are clearly separated (AFM: antiferromagnetic metal, PMM: paramagnetic metal, SC: superconductor). After [43].

3.2 The '122' compounds

Shortly after the '1111'-type pnictide superconductors were discovered a second very similar structure was found to be superconducting. The so called '122'-type superconductor is probably the best studied compound. It is rather easy to grow single crystals of the structure and thus makes it a perfect candidate for characterization of intrinsic physical properties. Especially in the field of thin films the '122'-compounds play an important role. The first compound of this type of material was $BaFe_2As_2$ discovered by Rotter *et al.* [23].

Figure 3.1b shows the crystal structure of $BaFe_2As_2$, abbreviated as 122. This compound crystallizes in the $ThCr_2Si_2$-type structure [23]. This type is also a tetragonal crystal system with space group 139 (*I4/mmm*). Obviously, in this compound only one anion is present (arsenic in its -3 valance state). Maximum T_C in this type of iron based superconductors is 38 K in the K doped Ba122 compound. Obviously in this structure the $(RE_2O_2)^{+2}$ layer is replaced by a single ion. These compounds become superconducting by hole doping on the (Sr, Ba)-site by potassium (38 K) [23] or caesium (37 K)[24] or by electron doping on the iron site by cobalt (22 K)[35], nickel (19 K)[58] or rhodium (24 K) [59]. The undoped '122'-type compositions show a similar antiferromagnetic behaviour as there '1111'-counterparts and also have the structural distortion which can be suppressed by doping. So the partial replacement of arsenic by isoelectronic phosphorous leads to a suppression of the structural and antiferromagnetic transitions and induces superconductivity [60]. This behaviour suggests an influence of the unit cell volume of the compound on the superconducting behaviour since the smaller phosphorous leads to a shrinking of the unit cell. On the other hand an isoelectronic doping of Ba by Sr (or vice versa) does not lead to superconductivity although the volume of the unit cell decreases in a similar way [61]. Rotter *et al.* [62]

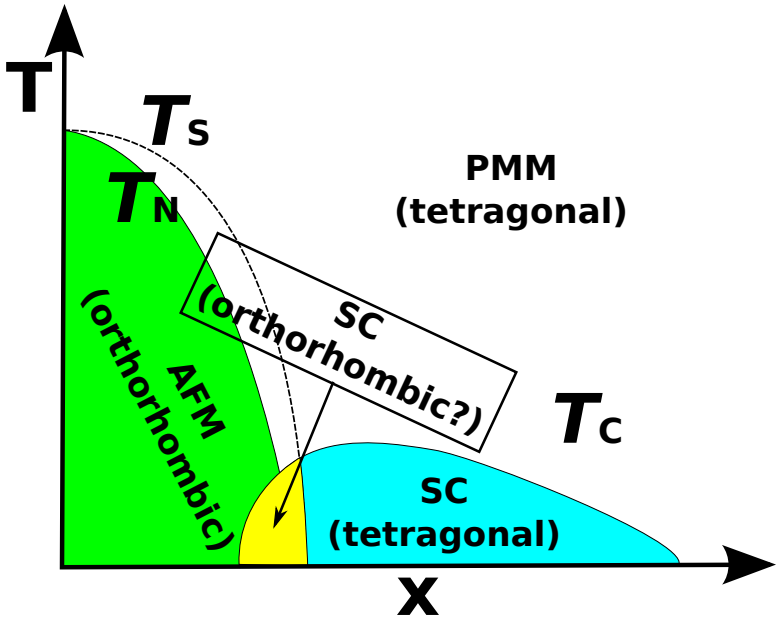

Figure 3.4: Schematic phase diagram of the '122'-type iron based superconductors. It is shown temperature T versus various doping contents x (AFM: antiferromagnetic metal, PMM: paramagnetic metal, SC: superconductor). After [43].

revealed a connection of the heights of the pnictogen atoms from the iron layer to the suppression of the SDW and the magnetic transition. The difference in height in the phosphorous containing system and the arsenic system come from the large size mismatch of these two elements. The doping behaviour of the '122'-type compounds is visualized in figure 3.4. At zero and low doping levels the compound is a paramagnetic poor metal in a tetragonal structure. With decreasing temperature a similar structural transition to a orthorhombic crystal system occurs and the system starts to order antiferromagnetically. Only at sufficient doping levels the structural transition and the antiferromagnetic ordering is suppressed and superconductivity below T_C can be observed. But there is a remarkable difference between the '1111'-type compounds and the '122'-type superconductors. While in the '1111'-types the antiferromagnetic order is suppressed when superconductivity emerges, there is a coexistence of antiferromagnetic and superconducting phase indicated as yellow area in the phase diagram in figure 3.4 [63–66].

Similar to the '1111'-type compounds the Fe-Fe spacing is rather short with a value of 2.77 Å [67] and is also responsible for the 3*d* Fe electrons taking part in the band formation. Again, the density of states is rather large near the Fermi energy [55].

To reveal the Cooper pair angular momentum pairing of course also for this compound some NMR and Josephson junction measurements were performed. These measurements reveal, similar to the '1111'-compound, a spin singlet behaviour with an *s*-wave pairing [68].

3.3 The '111' compounds

The third group of iron base superconductors with the FeAs layered structure was reported first by Tapp *et al.* [26] and soon confirmed by Wang *et al.* [27] and Pitcher *et al.* [28]. The LiFeAs compound has a T_C as high as 18 K and belongs to the CeFeSi type crystal structure

(*P4/nmm* space group, see figure 3.1c). Later Parker *et al*. [69] found that substitution of lithium by sodium lead to superconducting '111'-type compound NaFeAs with T_C as high as 18 K. The structure is almost identical to the '1111'-type compounds. Only the oxygen is removed completely and the rare earth elements are substituted by lithium or sodium ions. Because of the similarity, the tetrahedrally coordinated iron is also found for this type of pnictide superconductors. Remarkable about this type of iron based superconductors is the superconducting nature in the undoped parent compound [26]. Wang *et al*. [70] showed, that the undoped parent compound is an electron overdoped superconductor. Since the structure, especially of the FeAs layers, is almost identical to the '1111'-type and '122'-type compounds this behaviour was not expected. Borisenko *et al*. [71] suggested that the reason for that is because of magnetic fluctuations. The behaviour revealed by ARPES measurements is almost a ferromagnetic one and favours a more *p*-wave triplet superconductivity than a singlet pairing state. Moreover, slight lithium deficiencies lead to a destruction of the superconducting state [26, 27]. Wang *et al*. [70] revealed the reason for this in a suppression of superconductivity because of an impurity scattering effect. A similar behaviour of destruction of the superconducting transition was found by Pitcher *et al*. [72] for electron doping by partially substituting iron by cobalt or nickel. The structural and magnetic transitions which were observed for the other compounds are not present in the '111'-type superconductors.

However, although this compound is very interesting and exhibit completely different physical properties compared to the other pnictide superconductors, this '111'-type compounds are much less studied than the other compounds. Reason for that is probably the extreme instability in ambient atmosphere leading to direct decomposition when exposed to air. Because of that, a phase diagram of LiFeAs or NaFeAs could not be produced since there are not enough data [55].

3.4 The '11' compounds

Last type in this series of novel superconducting compounds is the so called '11'-type with a T_C of ∼8 K [29]. Containing selenium instead of arsenic this compound is not a pnictide but a chalcogenide. However, the FeSe superconductors belong to the iron based superconducting class not only due to the iron but also because of a similar crystal structure. This compound has a PbO structure and belongs to the *P4/nmm* space group (figure 3.1d). The layered structure consists of $FeSe_4$ layers. To induce superconductivity the system has to be doped by either selenium deficiencies or by partial substitution of selenium by tellurium [73–75]. Here it is remarkable, that the FeSe compound shows a structural transition similar to the '1111'- and '122'-type compounds but no magnetic transition, whereas the tellurium doped compound does show both transitions. Figure 3.5 shows a schematic phase diagram of $Fe(Se_xTe_{1-x})$. Here the antiferromagnetic transition for lower selenium contents is shown. The AFM ordering occurs together with the structural distortion. Increasing the selenium content results in a short range spin glass state. Note here, that for this type of compound no simultaneous long range magnetism and superconductivity is observed. With a further increase of selenium the spin glass state change to a superconducting state. Other substitution studies were performed by Mizuguchi *et al*. [76]. While doping the selenium site with tellurium or sulfur enhances T_C up to a doping level

of ∼75% and ∼20%, respectively, doping on the iron site with cobalt or nickel leads to a suppression of T_C at a doping level of ∼10%.

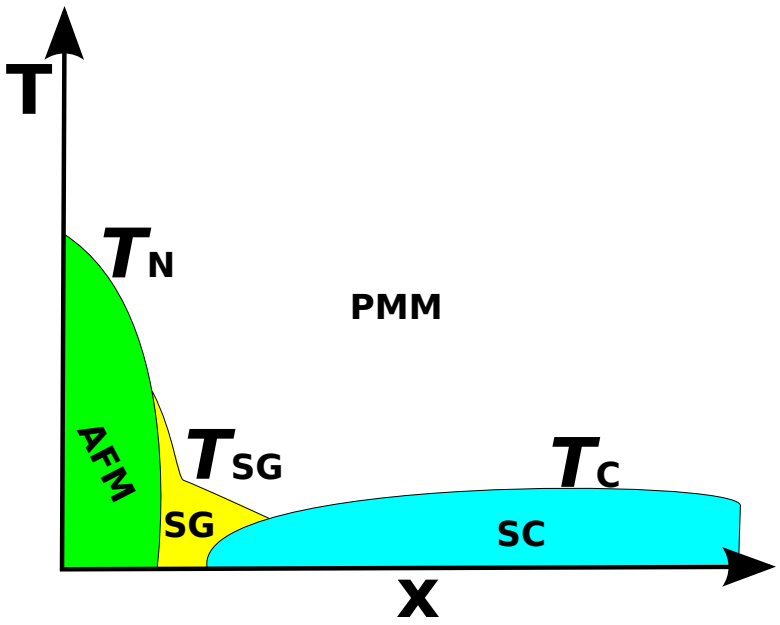

Figure 3.5: Schematic phase diagram of Fe(Se_xTe_{1-x}) superconductors. It is shown temperature T versus various doping contents x. (AFM: antiferromagnetic metal, PMM: paramagnetic metal, SC: superconductor). After [77].

Another way to enhance superconductivity in FeSe is to apply pressure. Margadonna *et al.* [78] found that a pressure of only 2.6 GPa lead to an increase in T_C to 27 K. The maximum improvement is reached at 37 K for a pressure of 7 GPa. A further increase in pressure then leads to a decrease in T_C and at 14 GPa a T_C of only 6 K can be observed. One explanation for that could be the tetrahedral bonding angle described for the '1111'- type and '122'-type structures (see sec. 3.1 and 3.2). One could think that under pressure the bonding angle reaches its optimum value of 109.47°. But in fact that is not true for FeSe and the reason for the enhanced T_C under pressure is to find in the band structure which also changes under pressure. However, the actual reason is not clarified yet.

Beside the '11'-type chalcogenide superconductors there is a second class of iron based compounds exhibiting superconductivity and containing chalcogenides. This compound has a stoichiometry of $A_{0.8}Fe_{1.6}Se_2$ where A is potassium, rubidium, cesium or thallium and has a reduced *I4/m* symmetry. The stoichiometry and the crystal structure is very close to the '122' compounds which is why these type of superconductors are often called '122*'-type compounds. T_C in these compounds is around 30 K [79]. These compounds are much less studied and of less importance and because of that not described any further here.

3.5 Thin film growth of pnictide superconductors

Thin films are crucial in the field of superconductivity, not only for scientific reasons but also for device fabrication. Many research on josephson junctions is done in superconducting thin films and many microwave filters used in mobile communication today are made of superconducting thin films. But one of the most important areas for thin film fabrication

are superconducting tapes. So far, most commercially available tapes are made of cuprate superconductors. But the large upper critical field of iron based superconductors of more than 100 T makes these class of material highly appropriate for tape applications involving high magnetic fields [80, 81]. For that reason soon after the discovery of the iron based pnictide superconductors research in thin film growth of these compounds had started. The following section gives a brief overview of results achieved in the field iron based superconducting thin film deposition.

3.5.1 Thin films of '1111' compounds

So far, only a few groups world wide were successful in growing '1111'-type pnictide superconductor thin films. The deposition techniques used by these groups are Pulsed Laser Deposition (PLD) and Molecular Beam Epitaxy (MBE).

First attempts to grow '1111'-type LaFeAsO films were done by PLD with the second harmonic of a Nd:YAG laser and were published 2008 by Hiramatsu *et al*. [82]. They succeeded in growing epitaxial LaFeAsO films on MgO(001) and (La,Sr)(Al,Ta)O_3((LSAT) (001). However, the grown films exhibit impurities of a LaAs phase and a post deposition treatment of annealing in vacuum or H_2 atmosphere was necessary. A superconducting transition was not observed down to 2 K and the resistivity behaviour was similar to that of undoped bulk samples. It was important to use targets of high quality without any impurity phases. Especially La_2O_3 and LaOF impurities are likely to be incorporated in the film.

The first successful growth of superconducting LaFeAsO thin films was done by Backen *et al*. [83] on MgO(001) and $LaAlO_3$ (LAO) (001). They also used PLD but with a KrF excimer laser. The deposition was done at room temperature and crystallization was realized with a subsequent thermal treatment after film growth in an evacuated silica tube. The films were highly textured and showed minor impurities of FeAs, LaOF and La_2O_3. Although, superconductivity was confirmed by magnetic measurements, only a T_C onset was observed at 11 K without zero resistance down to 2 K. Reason for that is wrong fluorine doping and showed that the transfer of fluorine from the target to the film is challenging since the target had a fluorine concentration of 25 at.%.

The first report to overcome this issue was published by Kidszun *et al*. [84] and Haindl *et al*. [85]. They achieved epitaxial $LaFeAsO_{1-x}F_x$ films on LAO by a PLD growth process and additional thermal treatment after the deposition. With optimized growth parameters and improved thermal annealing atmosphere it was possible to grow films with a superconducting transition onset of 28 K and a T_C zero of 20 K. Only minor oxide impurities were observed in the XRD scan. With similar procedure it was also possible to grow epitaxial $GdFeAsO_{1-x}F_x$ thin films [86]. Although, a phase formation was confirmed by XRD scans, only a T_C onset at 41 K was obtained and no T_C zero could be observed down to 2 K.

Similar issues as in the PLD grown films regarding the fluorine content in the structure were found in thin film growth of '1111'-type compounds by MBE as growth technique. Kawaguchi *et al*. [87] were the first to report the growth of NdFeAsO films on GaAs(001) substrates by MBE. In their approach they used solid state sources of NdF_3, As, Fe and Fe_2O_3. They found out, that the ratio of oxygen flux versus arsenic flux is of importance in growing impurity free '1111'-type compounds. Too high or too low ratio resulted in NdAs and other impurity phases. However, although they were successful in growing epitaxial impurity free films in a small parameters windows, a superconducting transition was not observed down

to 2 K. Again, the suggestion for that behaviour was a lack of incorporated fluorine into the structure. Surprisingly, they found a correlation of deposition time and fluorine content. While deposition times $t_d \leq 4$ h resulted in high quality epitaxial thin films of NdFeAsO without impurity phases and no superconducting transition, increasing t_d to or above 5 h resulted in superconducting epitaxial thin films with T_C zero as high as 42 K [88]. It was also confirmed by Secondary Ion Mass Spectroscopy (SIMS) measurements that only in films grown at $t_d \geq 5$ h fluorine is incorporated into the structure. The explanation for this behaviour is the formation of a NdOF layer on top of the film surface preventing the fluorine to escape from the structure and, thus, act as a dopant.

A similar approach was done by Ueda *et al.* [89]. They grew SmFeAsO '1111'-type films on r-cut sapphire substrates. To dope the films with fluorine a top layer of SmF_3 or NdF_3 was grown. That layer acts as an fluorine reservoir and allows doping of the films. With that, T_C zero of 48.6 was obtained. However, the highest T_C was observed for $NdFeAsO_{1-x}F_x$ thin films grown by MBE on CaF_2 substrates with a T_C as high as 52 K [90]. Their suggestion for the high T_C is a substrate influence. The CaF_2 substrate has a smaller lattice parameter as the $NdFeAsO_{1-x}F_x$ films and, thus, induce a compressive lattice-strain effect which affects T_C in a positive way.

In conclusion it can be said, that the growth of superconducting '1111'-type pnictide thin films is possible with PLD and MBE. MBE seems to be the more effective method, since the independent control of each single source allows for a higher flexibility. Because of that, it is easier to obtain the small parameters window in which the '1111'-type phase forms as a thin film. Although, there were reports on the successful growth of *RE*FeAsO thin films, the focus in thin films research world wide was more in the field of the '122'-type compounds which will be discussed in the next section.

3.5.2 Thin films of '122' compounds

The second important group of the pnictide superconductors is the '122'-type of compounds. With a bulk T_C of ∼38 K for potassium doped , it is the second highest in this new class of high T_C superconductors. And the fact, that it contains no oxygen makes it a perfect candidate for thin film growth since the presence of two anions (oxygen and arsenic in '1111') is challenging. The first attempts to grow this class of material was done by PLD (Nd:YAG laser) for a cobalt doped variant of $SrFe_2As_2$ which has a bulk T_C of 20 K [91, 92]. The advantage of the cobalt doping in this attempt is the much lower vapour pressure of cobalt compared to fluorine which caused the issues in gaining superconductivity in the '1111'-type thin films. Similar issues were expected for potassium doping in the '122'-type films. Although highly *c*-axis oriented $SrFe_{1-x}Co_xAs_2$ films with a T_C onset of 20 K and a T_C zero of 14 K were obtained on LSAT (001) single crystal substrates, the films also exhibit FeAs impurities and had FWHM of the rocking curve of 1° at optimal growth parameters. However, the T_C of 14 K which is similar to the reported bulk values and high H_{C2} of >9 T at ≤9 K showed the advantage of the '122' compound for film deposition compared to the '1111'-type compounds. Further increase in T_C zero in $SrFe_{1-x}Co_xAs_2$ thin films was achieved by Choi *et al.* [93]. They also used PLD as growth technique but with a KrF excimer laser. In their attempt they achieved a T_C zero of 16.5 K and FWHM of the rocking curve of 0.8° with films grown on LAO (100) but still FeAs impurities were observed in the $2\theta - \theta$-scan. Interestingly, Hiramatsu *et al.* [94] found water induced superconductivity

as high as 25 K (T_C onset) in undoped $SrFe_2As_2$ thin films. They found that exposing undoped films (not superconducting) to ambient atmosphere for ∼6 h leads to an emerging superconducting transition at 25 K and a T_C zero of 21 K which is slightly higher than the reported bulk value of 20 K. They found the reason for that to be water incorporated into the structure from air. The same effect was not observed in dry nitrogen or oxygen atmosphere, but in high humidity environments. This was the first time that water induced superconductivity was observed in iron based superconductors. Later on, it was also observed in bulk samples of '122' compounds and even in '1111' compounds [46, 95–100]. Potassium doped thin films of $SrFe_2As_2$ grown by PLD were not reported. Instead, a recent publication report on the growth of indirectly electron-doped $SrFe_2As_2$ thin films with lanthanum grown by PLD [101] with a T_C as high as 20 K which is identical to the directly electron-doped $SrFe_{1-x}Co_xAs_2$ compounds.

For the growth of $SrFe_2As_2$ thin films by MBE only one report is found in literature. Agatsuma *et al*. [102] reported on the growth of epitaxial undoped $SrFe_2As_2$ on r-cut sapphire as well as on the growth of potassium doped $Sr_{1-x}K_xFe_2As_2$ thin films. They achieved epitaxial *c*-axis oriented thin films of $SrFe_2As_2$ and superconducting $Sr_{1-x}K_xFe_2As_2$ thin films with a T_C zero as high as 22.9 K (T_C onset was reported at 30.3 K). FeAs impurities were also reported in for these films. While the growth temperatures for the PLD grown films were in the region of 600–800 °C, the MBE grown films were deposited at substrate temperatures of ∼400 °C for the undoped compound and at ∼250 °C for the potassium doped ones to overcome the high vapour pressure of potassium.

Most research in thin film fabrication for the '122' compounds was done for the barium '122'-system. Potassium doped $BaFe_2As_2$ has a rather high T_C of 38 K in bulk samples and the thin films are more stable compared to the $SrFe_2As_2$ compound thin films [103]. The first films were grown by Katase *et al*. [103] by PLD (Nd:YAG laser) on LSAT and were cobalt doped. The epitaxial *c*-axis oriented films exhibit no impurity phases as it was observed for the $SrFe_2As_2$ thin films. Only a pure iron peak was found. FWHM of the rocking curve was determined to be 0.6° which is an improvement compared to the $SrFe_2As_2$ thin films. T_C was found to be 20 K.

While Lee *et al*. [105] fabricated high quality thin films of $BaFe_{1-x}Co_xAs_2$ on $SrTiO_3$ (STO) bicrystals and discussed the grain boundary nature of $BaFe_{1-x}Co_xAs_2$, Iida *et al*. [104] investigated the effect of strain in the films on T_C. For that, they grew $BaFe_{1-x}Co_xAs_2$ thin films on different substrates and found that STO exhibit the best superconducting properties in thin films with a T_C of 24.5 K [81]. Figure 3.6 shows the T_C of the thin films for various substrates. STO has the lowest misfit of only -1.32%. The conclusion was that the deformation of the $FeAs_4$ tetrahedra affect the superconducting properties and that larger deformation lead to an decrease in T_C. Remarkable in these experiments were the observation of 45° rotated grains of $BaFe_{1-x}Co_xAs_2$ grown on YAO which was not found for the other substrates.

To further improve the crystal quality of $BaFe_{1-x}Co_xAs_2$ thin films Lee *et al*. [106] proposed buffer layers of STO or $BaTiO_3$ (BTO) with a thickness of 50–100 unit cells (∼0.2–0.4 nm). They claimed more effective bonds between '122'-type films and substrates because of the STO or BTO buffer layers. But they could improve T_C to a value of only 22.8 K which is lower than the values reported by Iida *et al*. [104] for $BaFe_{1-x}Co_xAs_2$ films grown directly on STO substrates. Another buffer layer set up was reported by Iida *et al*. [107, 108] who grew $BaFe_{1-x}Co_xAs_2$ thin films on various substrates with iron buffer layers.

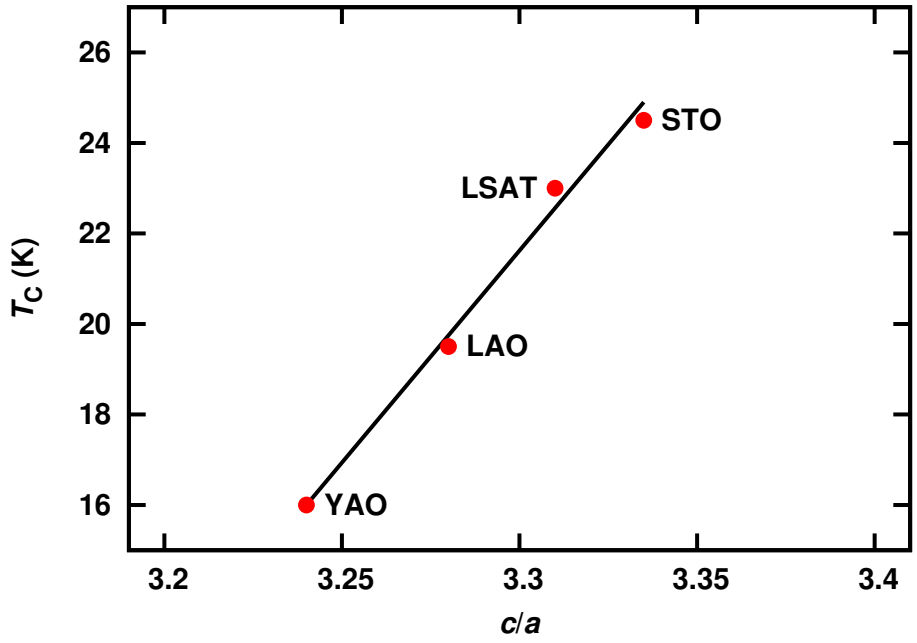

Figure 3.6: Variation of T_C with various substrates. After [104] (YAO = $YAlO_3$).

Although an improvement of T_C was not observed they could improve the critical current density J_C with the iron buffered films. The optimum iron buffer thickness was determined to be 15 nm. However, MBE grown $BaFe_{1-x}Co_xAs_2$ thin films were not reported.

Since, it is rather easy to fabricate cobalt doped $BaFe_2As_2$ films compared to the deposition of the '1111'-type compounds numerous studies on this topic were done. However, T_C for the cobalt doped 'Ba:112' compounds is low compared to their potassium doped counterparts. The first report on the growth of potassium doped $BaFe_2As_2$ thin films was done by Lee *et al.* [109]. They grew undoped $BaFe_2As_2$ at room temperature and then annealed the fabricated films at 700 °C with potassium in evacuated quartz tubes. The obtained films exhibit *c*-axis oriented growth on LAO (001) and Al_2O_3 (0001) substrates and had a T_C of 40 K which is even larger than reported for bulk $Ba_{1-x}K_xFe_2As_2$ samples.

MBE grown films of $Ba_{1-x}K_xFe_2As_2$ were reported by Takeda *et al.* [110] and Ueda *et al.* [89]. Similar to the $Sr_{1-x}K_xFe_2As_2$ films already mentioned above the $Ba_{1-x}K_xFe_2As_2$ films were fabricated *in situ* at reduced deposition temperatures of 250–300 °C. The resulting films exhibit high crystal quality and a T_C of 38.3 K which is very close to the reported bulk values.

To summarize this small section on the growth the '122'-type iron pnictide superconductors it can be said that it is much easier to grow high quality thin films of the '122'-type compound than of '1111'-type compounds. Reason for that may be the oxygen free nature of these compounds since oxygen content is always challenging to control. In addition, the possibility to dope the '122' compounds with a metal (cobalt) makes the growth much easier since it is not as volatile as fluorine. However, although potassium has similar issues as fluorine because of the high vapour pressure, there were also successful attempts to grow $Ba_{1-x}K_xFe_2As_2$ thin films by PLD and MBE.

3.5.3 Thin films of '11' compounds

The first reports on the deposition of '11'-type thin films was by Wu *et al*. [111]. They grew $FeSe_{1-x}Te_x$ films with the PLD technique (KrF laser) on MgO (100) substrates. The films exhibit *c*-axis oriented growth and were free of impurities. Interestingly, this type of pnictide based superconductors also grow with some domains 45° rotated with respect to the substrate. They concluded that the large misfit of 10% is the reason for that rotation of some domains. Later the same group could show that the rotation of the domains is temperature dependent [112]. Films grown at lower temperatures of ∼320 °C do not grow rotated while films grown at higher substrate temperatures of ∼500 °C grow 45° rotated with respect to the substrate. A maximum T_C was observed for the films grown at $x = 1$ with a transition at 13 K [111]. Reason for that could be a strain in the film resulting from the large misfit. Undoped, pure FeSe films are not superconducting at all. In addition, a clear dependence of film thickness and T_C was observed. While films with a thickness below 30 nm exhibit no T_C zero, The highest T_C of 12 K for $FeSe_{1-x}Te_x$ with $x = 0.5$ was observed for films with a thickness of 600 nm. The reason could be less strain influence in the thicker films. The film's characteristic becomes more bulk-like. The dependence of T_C of the film thickness is only true for the films grown at low temperature, while the films grown at higher temperature do not show any T_C dependence with substrate temperature.

Superconducting thin films of $FeSe_x$ ($x = 0.8 - 0.92$) were also reported by Han *et al*. [113]. They grew the films on STO, LSAT and LAO substrate with a XeCl excimer laser. The films were *c*-axis oriented but most of them did not show a T_C zero but only a transition onset, although the onset was observed at rather high temperatures of ∼11 K. Since then, many '11'-type thin films have been grown but many did not show a real T_C zero [81]. Interestingly, it is possible to grow undoped FeTe films which exhibit a superconducting transition although the bulk samples of FeTe are not superconducting without doping. Beside Wu *et al*. [111], which was described above, Han *et al*. [114] reported a study on FeTe thin films and their superconducting properties. They showed, that it is possible to grow FeTe films with a T_C onset as high as 13 K. For that the films have to have a thickness larger than ∼90 nm. Below, a T_C was not observed. They also could show, that superconductivity was only observed for "stretched" films and not for compressed ones.

The highest T_C exhibit in thin films of the '11'-type compounds was reported by Bellingeri *et al*. [115]. They grew 200 nm thick films of $FeSe_{0.5}Te_{0.5}$ on LAO, STO and ZrO:Y (YSZ) with a KrF excimer lase and exhibit a T_C as high as 21 K which is ∼5 K higher than reported for bulk samples. They observed a decrease in *a*-axis lattice parameter with increasing thickness. A minimum in *a*-axis lattice parameter was reached for a thickness of 200 nm where the maximum T_C of 21 K was achieved.

Superconducting FeSe films grown by MBE were reported by Agatsuma *et al*. [102]. As in the other pnictide superconducting compounds the parameters window for the growth of the superconducting phase is rather small. The superconducting β-Fe_xSe forms for $x = 1.010 - 1.025$ which is very narrow. Even in this small window, T_C varies between 8.5 K for $x = 1.010$ to 0 K for $x = 1.025$. The growth temperature has to be below 450 °C to obtain the superconducting tetragonal phase. While it is possible to grow superconducting thin films on LAO, the parameters window to grow superconducting FeSe films with MBE could be expanded by choosing r-Al_2O_3 ((1012)-surface) substrates. This is

in agreement with the PLD grown films where substrate induced strain in the film lead to better superconducting properties. In this case, LAO is almost perfectly lattice matching while the *r*-cut sapphire has a strain effect on the film. Although a superconducting transition onset was observed even for optimized parameters no T_C zero could be achieved.

In conclusion it can be said, that the simple composition of the '11'-type superconductors makes it rather easy to grow thin films. The necessity to dope with a volatile dopant like fluorine or potassium is not there for the '11'-type family of iron based superconductors. The most crucial factor in thin film growth for this compound seem to be a substrate induced strain in the films. With that it is possible to induce superconductivity without changing the composition or even induce superconductivity in compositions which are usually not superconducting. As already observed in the other compounds, growth by MBE seems to be more challenging than growth by PLD since the parameters window is rather narrow.

4 Thin Films

Thin films can be defined as layer of material on top of a substrate ranging from a few nanometer to the micrometer range in thickness. Usually, they show different characteristics compared to analog bulk materials which come from different reasons like stress influence, quasi–two dimensional properties or interactions with the substrate surface. Thin film formation can be traced back to observations of Grove (1852) and Faraday (1957) [116]. Grove noticed, that metal, which was sputtered from the cathode of a glow discharge plasma, had formed coatings after his experiments. Faraday experimented with exploding fuselike metal wires in an inert atmosphere and, thus, evaporated thin films.

Today, thin films are important as coatings for optical applications like antireflection coatings, mirrors or beam splitters or for mechanical purposes like improving wear resistance or corrosion protection. Furthermore, in microelectronics thin films play a very important role. Especially the field of semiconductors and sensors is unimaginable without thin film technology.

In general, thin film deposition techniques could be divided into two main groups; physical vapor deposition (PVD) and chemical vapor deposition (CVD) [117]. To the group of chemical vapor deposition techniques belong methods like Metal Organic Chemical Vapor Deposition (MOCVD) or Metal Organic Vapor Phase Epitaxy (MOVPE). To the second main group of thin film preparation techniques belong methods like thermal evaporation, sputtering, Pulsed Laser Deposition (PLD) and Molecular Beam Epitaxy (MBE). For the experimental part of this thesis a PVD method used, namely the MBE technique. Beside the former mentioned vapor techniques there are many more physical deposition techniques such as solid phase deposition (SPD) and liquid phase deposition (LPD). These are beyond the scope of this report and will not be described further in detail.

This chapter gives a short overview about thin film formation and describes the principles of MBE. It also summarizes some aspects of substrate selection and preparation.

4.1 Thin Film Formation

For the formation of a thin film on top of a substrate a series of surface processes are involved which are illustrated in figure 4.1. These processes can be summarized as follows (as described in reference [118]):

1. adsorption of atoms or molecules reaching the surface
2. surface migration and dissociation of the adsorbed atoms or molecules
3. incorporation of adsorbed atoms into the crystal lattice of the substrate or the already grown epilayer
4. thermal desorption of the species not incorporated into the crystal lattice

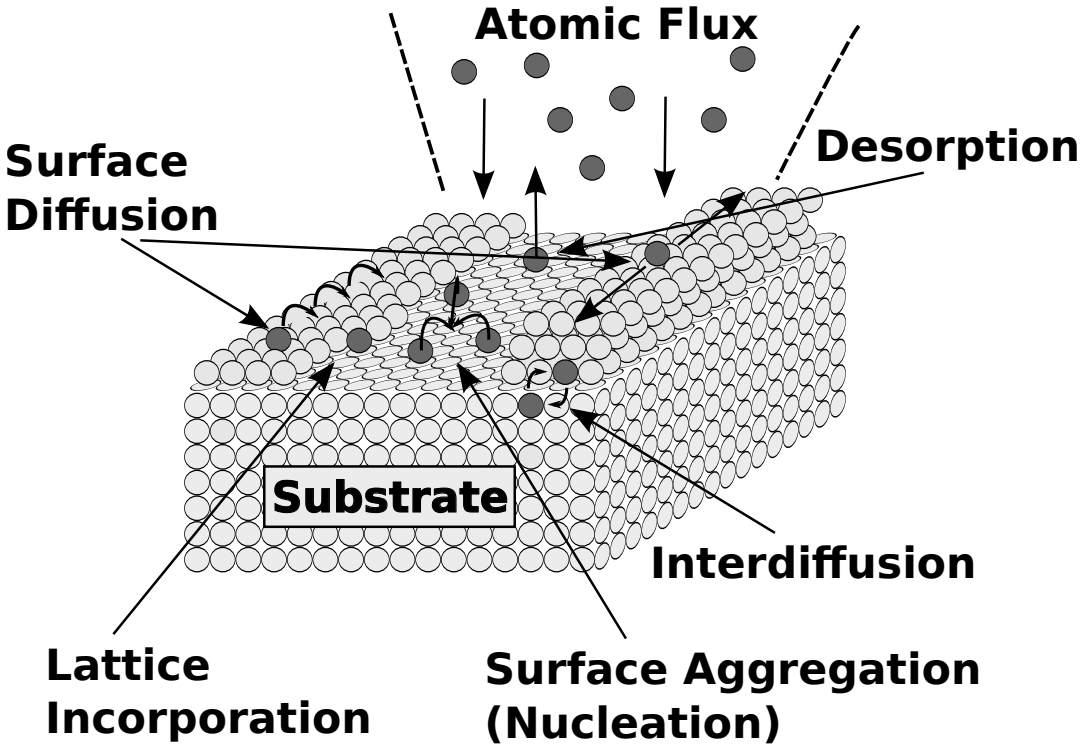

Figure 4.1: Schematic illustration of the surface processes occurring during epilayer growth. After [118].

Adsorption is divided into two types: physical adsorption and chemical adsorption. With physical adsorption or physisorption there is no electron transfer between the adsorbate and the adsorbent. Binding happens trough attractive van-der-Waals forces. The second one, chemisorption, can be described as an electron transfer between the adsorbate and the adsorbent. The process of electron tansfer results in forces similar to forces occurring in chemical bonds. Thus, adsorption energies for physical adsorption happen to be smaller than for chemical adsorption. This can be seen in the interaction potential for the two adsorption types illustrated in Figure 4.2.

Film growth is influenced by many parameters like temperature and surface quality of the substrate, interaction between the film material and the substrate material, ambient pressure and residual gases and so on. Thus, different growth modes are observed for the formation of thin films (figure 4.3). Island or Volmer-Weber growth occurs when nucleated clusters grow in three dimensions and form separated islands. This growth mode is observed for films where the bonding force is stronger between the atoms or molecules of the film material to each other than between the substrate and the atoms or molecules of the film. The opposite situation is observed for the growth mode the layer-by-layer or Frank-Van-der-Merwe growth. Here, the film nucleus grows in two dimensions and, thus, forms single layers. In this mode the atoms or molecules of the film material are more strongly bond to the substrate. After the first layer is completed, the second layer is less tightly bond. In every additional layer, the bonding energy is more decreased until the bulk-crystal value is reached. The third growth mode can be described as a combination of the island and the layer growth, the so called Stranski-Krastanov growth mechanism. In this

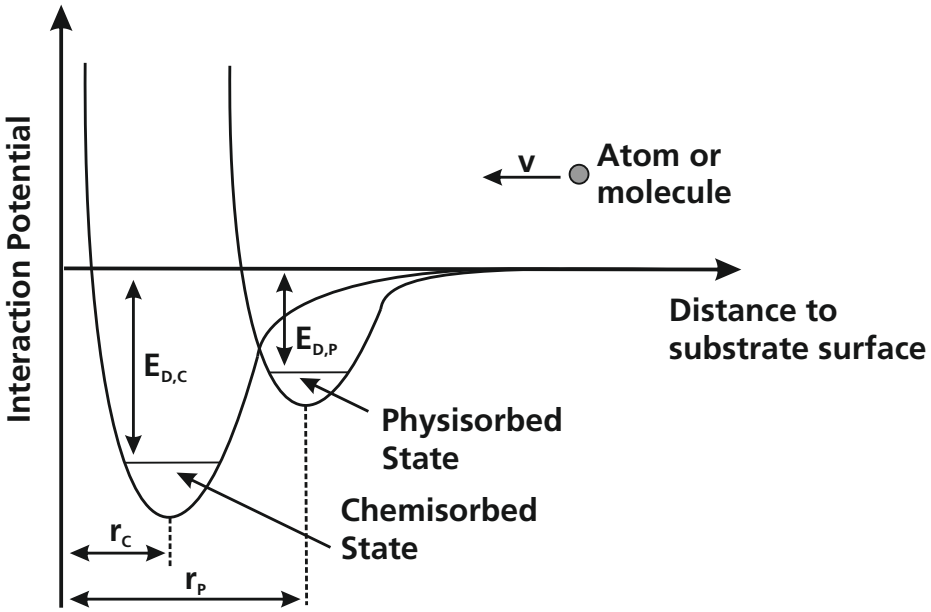

Figure 4.2: Interaction potential due to the surface as seen by an atom or molecule impinging perpendicular to the surface for chemisorption and physisorption. After [118].

growth mode one or more layers form until this type of film formation becomes unfavorable and islands begin to grow. Depending on factors like lattice match or chemical compatibility between substrate material and film material, films can form amorphous, polycrystalline or single crystalline epitaxial phases. Epitaxial growth means a film formation with identical lattice structure and orientation as the substrate. For this, it is very important that the lattice parameters of the substrate and the film are roughly identical. There are two types of epitaxy, homoepitaxy and heteroepitaxy. For homoepitaxy the film consists of the same material as the substrate, whereas for heteroepitaxy substrate and film are of different materials. This can lead to stress or strain in the film due to lattice misfits, different thermal expansion coefficients etc. Thus, it is important to choose the substrate very carefully according to the parameters of the deposited material.

4.1.1 Substrate Selection and Preparation

As mentioned in the former section, substrate selection is very important when depositing thin films. There are a lot of parameters to consider in determining the suitability of a substrate. A detailed discussion of substrate selection can be found in reference [119].

First and maybe most important is the chemical compatibility of substrate and film material. Ideally there are no chemical reactions. In addition, high deposition temperatures make substrate selection a critical point in thin film growth. If there is oxygen involved, it gets even more complicated. Another important parameter connected to temperature is

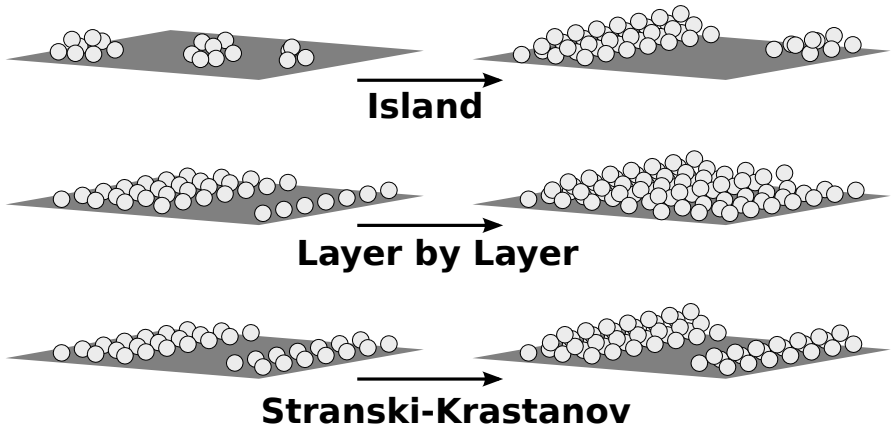

Figure 4.3: Basic growth modes for thin films. After [116].

the thermal-expansion coefficient. If the thermal expansion coefficients of the film material and the substrate differ too much, a loss of adhesion or film cracking during thermal cycling is the consequence. In particular for brittle materials a very small thermal-expansion mismatch is crucial. The surface quality of a substrate also is not to underestimate. A uniform surface is necessary to ensure a uniform, homogeneous film growth. Various types of irregularities have to be considered like defects on the atomic scale (point defects, dislocation lines etc.), submicron features (polishing scratches, pores etc.), the micron scale (grinding scratches, crystalline boundaries etc.) and macrodefects (surface wrap, cracks). Thus, an ideal substrate would have a flat, dense surface and be free of twins and other structural inhomogeneities [119]. Needless to say that substrate cleanliness plays a prominent role. All these mentioned parameters are valid in general for epitaxial and non-epitaxial growth. For epitaxial growth additional requirements are necessary. The most important property of a substrate is its lattice match with the film. Epitaxial growth will not occur if the lattice mismatch is too big. Studies showed that a lattice mismatch of less than 15 % is required for epitaxy [119]. In addition, to get even better results, coincidence sites between the lattices of substrate and film materials are necessary. These are atomic positions that coincide on either side of the interface, which would improve the chance of epitaxy. Thus, it is desirable for the substrate and film to have the same or at least a similar crystal structure.

Beside these two mentioned issues structural quality of the substrate and surface quality play important roles for epitaxial growth. Especially surface quality is a matter of substrate preparation and treatment. Moeckly *et al*. [120] studied the effect of substrate preparation on YBCO films grown on MgO substrates. They found that according to the preparation of the MgO substrate the YBCO films show different characteristics. E.g., T_C is different for chemical polished and mechanical polished substrates. An annealing step also can effect T_C because of the well-known hygroscopic nature of MgO. Thus, it is essential to handle the substrates with care and use an adequate preparation procedure to ensure the substrate is ready to be used for thin film growth.

4.2 Reactive Molecular Beam Epitaxy

A powerful technique to deposit high-quality epitaxial thin films based on the principle of PVD is the Molecular Beam Epitaxy (MBE) technique. In this growth technique elemental solid state sources are evaporated by heating, laser or electron beam. A beam of atoms or molecules emerges and leads to thin epitaxial layers on a substrate surface via reactions between the single beam atoms. The substrate is maintained at an elevated temperature. The whole process takes place in an ultrahigh vacuum. The composition of the grown layer can be adjusted by varying the deposition rates of the particular element. The deposition rates can be regulated by the evaporation rates of the appropriate sources. Typical growth rates are around 1-10 nm/s [118]. The rather low growth rate is necessary to ensure surface migration of the impinging species. The surface migration process is also supported by the heated substrate. In that way, a very smooth surface of the grown layer can be obtained.

The main advantage of MBE is the ability of a very precise control of the atomic flux. Hence, the composition of the grown film can be adjusted in nearly any order. Because of vacuum deposition, MBE conditions are far from thermodynamic equilibrium. Thus, for film formation only the kinetics, which occur during the deposition process, are important. Since, MBE is realized in an ultrahigh vacuum environment, it is possible to use surface sensitive characterization methods such as reflection high energy electron diffraction (RHEED) or spectroscopic ellipsometry (SE). With these *in situ* methods it is possible to monitor the film deposition process. In the present study only RHEED was used.

4.2.1 MBE unit used in the present study

A schematic drawing of the MBE unit used for the present study is shown in figure 4.4. The MBE unit is based on a custom design and consists of two chambers: a transfer chamber and a growth chamber. The transfer chamber is a small chamber which can be pumped down rather quickly to load samples into the growth chamber. Connection to the main chamber is provided by a gate valve. By this arrangement the main chamber can stay under ultra high vacuum (UHV) of $\sim 10^{-9}$ mbar all the time.

A substrate holder is placed in the middle of the main chamber and can be rotated through a manipulator to ensure a homogeneous film growth. The manipulator also contains a custom designed pyrolytic graphite substrate heater with a temperature capability of up to 800 °C. The maximum substrate size which can be used is up to 2". Substrate temperature is controlled by a thermocouple which is attached to the substrate holder. In addition, an external optical pyrometer is used to calibrate the substrate temperature. The UHV main chamber is equipped with three electron beam evaporators which allow the evaporation of three different metals simultaneously and independently. For source control and *in situ* rate monitoring the MBE unit is equipped with four quartz crystal microbalances (QCM) and a state-of-the-art four channel thin film deposition controller (Cygnus, Inficon). Three of the QCM are mounted above the sources and are provided with collimators to ensure an independent measurement for each single source. The fourth QCM is mounted in substrate level and is used to calibrate the three source QCM. It can be moved out of the substrate place. A shutter attached in front of the substrate provides control of the amount of

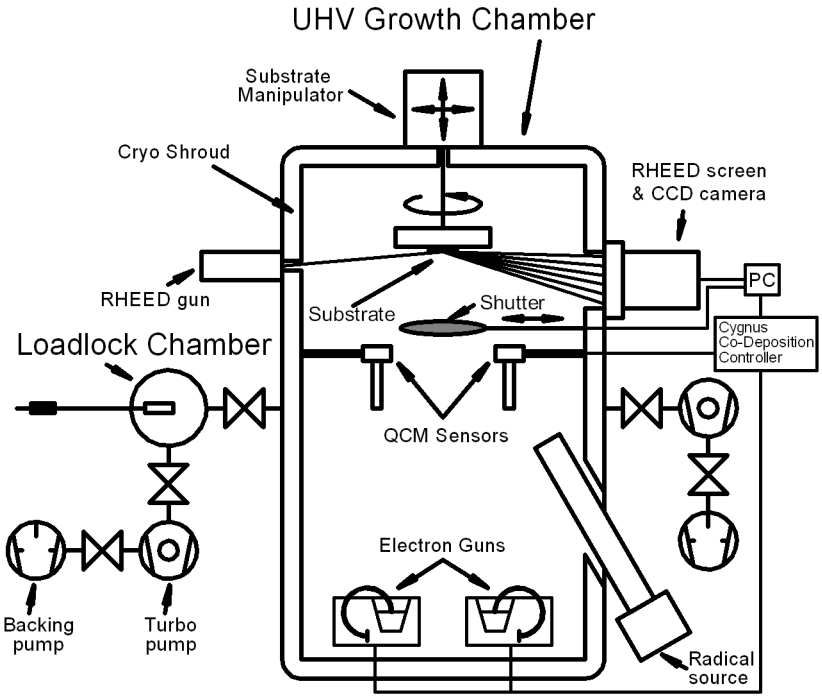

Figure 4.4: Schematic representation of the RMBE unit used in the present study.

deposited material and, thus, of the film thickness. An additional attached radio frequency (RF) activated oxygen source (HD25, Oxford Applied Research) provides radical oxygen and the gas flow is controlled by a separate mass flow controller. For oxide materials the oxidation conditions can be controlled by varying the RF power and/or the oxygen flow rate. For *in situ* monitoring the deposition process a Reflection High Energy Electron Diffraction (RHEED) setup is attached to the main chamber. It serves as a powerful tool to monitor the film growth in real time and at the same time enables the necessary modifications during film growth.

4.2.2 General growth procedure for the deposition of thin films of arsenic free pnictide superconductors

To grow the pnictide compounds the substrate, in most cases MgO, was glued onto stainless steel substrate holders using silver paste and then dried in air. As soon as the silver paste was dry, the substrate holder was introduced into the growth chamber of the MBE system through the load lock chamber. In the growth chamber, the substrate holder was heated to the required deposition temperature. The temperature was held for at least five minutes for temperature stabilization. After the growth temperature has stabilized the radical oxygen was introduced into the growth chamber at specific oxygen flow rates. Once the oxygen flow rate has stabilized the substrate shutter was closed before the elemental sources were started. For a homogeneous film growth, the substrate was rotated at 50 rpm. After the growth process was finished the substrate shutter was closed and elemental sources and radical oxygen were stopped. Then the films were cooled down in vacuum below a temperature of 150 °C before the sample was taken out for further characterization.

5 Characterization Methods

To study the growth of thin films a suitable characterization of the deposited samples is essential. To do that, a variety of *in situ* and *ex situ* techniques were utilized. As *in situ* techniques for analyzing the process of film formation RHEED and QCM already mentioned in section 4.2.1 were utilized. For an observation of the film deposition process the RHEED was used while rate control was done by the QCM.

After the deposition was finished and the film was taken out of the deposition chamber, *ex situ* methods like X-ray diffraction (XRD), magnetic susceptibility measurements using a superconducting quantum interference device (SQUID) and electrical transport measurements were performed. The following chapter gives an overview of the utilized characterization methods used during the experimental part of this work.

5.1 *In situ* techniques

5.1.1 Reflection High Energy Electron Diffraction (RHEED)

The Reflection High Energy Electron Diffraction technique is one of the standard methods in surface science to monitor the structure and the status of surfaces during the growth process. The high vacuum environment inside an MBE chamber makes RHEED a perfect tool for *in situ* analysis of the surface quality of a growing film. The RHEED technique is based on the diffraction of higher energy electrons at the surface of a sample. For that, every RHEED setup consists of an electron gun, providing the electrons. To visualize the diffracted electrons a phosphor screen for imaging is installed on the opposite site of the electron gun. The electrons have high energies in the range of 5–50 keV. As a consequence the Ewald-sphere is maximized and a sufficient area of reciprocal space can be observed on the relatively small angle of the phosphor screen. To provide information only of the sample surface and thus image only the first few layers of the growing film the incidence angle of the electrons is chosen to be rather small ($0.5° < \theta < 4°$) [118].

In figure 5.1 the schematic principles of a RHEED setup is illustrated. In comparison to other electron diffraction techniques like LEED (Low Energy Electron Diffraction) in big advantage of RHEED is the mounting point of the electron gun. It is mounted far away from the sample and thus does not block the molecular beam coming from the elemental sources in an MBE. In addition, a lot more information can be extracted from RHEED patterns like in-plane lattice parameter, roughness, crystallinity and phase purity. A further detailed description of RHEED applications can be found in reference [121]. During the experimental part of this work a Vieetech 052S set up was used. For image recording, a CCD-camera was installed and for analysis the k-Space Associates kSA-400 analysis software was utilized.

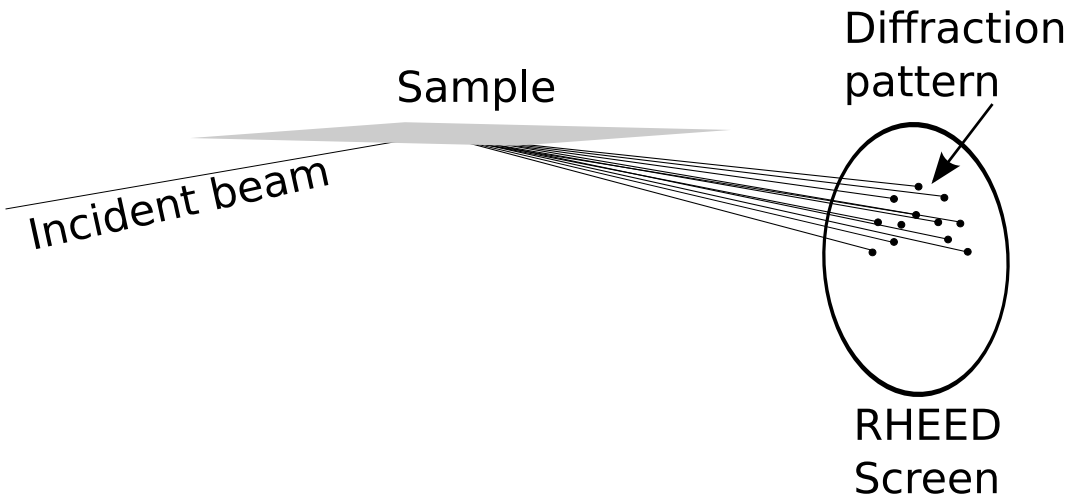

Figure 5.1: Schematic drawing of RHEED principles. The incident electron beam and the diffraction pattern on the RHEED screen can be seen.

5.1.2 Quartz Crystal Microbalance

For *in situ* rate control the MBE unit used during this work is equipped with a quartz crystal microbalance (QCM) as already mentioned in section 4.2.1. The QCM is supplied by Inficon. To perform the *in situ* rate control the QCM system is equipped with a piezo-electric quartz crystal, electrodes, a monitor for rate and thickness measurement and a controller for process automation [122]. The principle behind this technique is a change in resonance frequency of the quartz crystals. To measure this change in resonance frequency the quartz crystals are mounted between two electrodes. As soon as an AC-voltage is applied, the quartz crystal starts to oscillate at its resonance frequency due to the piezo-electric effect. The frequency is a function of the mass of the crystal. During film deposition the mass of the crystal changes and thus its frequency. The deposited mass is approximately proportional to the film thickness. Equation 5.1 allows a determination of the thickness.

$$T_f = \frac{N_q \cdot D_q}{\pi \cdot D_m \cdot F_c \; cdotZ} \cdot \tan^{-1}\left[Z \cdot \tan\left(\frac{\pi \cdot \left(F_q - F_c\right)}{F_q} \right) \right] \tag{5.1}$$

In equation 5.1 N_q is the AT-cut crystal constant with $N_q = 1.668 \cdot 10^{13}\text{Hz/Å}$, D_q is the density of the quartz with $D_q = 2.648\text{g/cm}^3$, D_m is the density of the monitored material, Z is the Z-factor, F_q is the starting frequency and F_c is the ending frequency. The Z-factor is the relation of the acoustic impedance of the deposited material Z_m to that of the quartz Z_q with $Z_q = 8.83$. For most common materials the Z-factors can be found in literature.

For every single elemental source a separate QCM is necessary. It is absolutely crucial that one QCM only monitors only one source at a time. This is achieved by the installation of collimators between the crystals and the sources. Because of that QCM systems are not mounted in substrate level and thus the monitored thickness differs from the real film thickness. This difference is corrected by a tooling factor which is determined by a calibration crystal mounted in substrate level or by *ex situ* thickness measurements.

Deposited mass of a material in time corresponds to a specific deposition rate and thus a QCM is a suitable control unit is capable of *in situ* rate control of the elemental sources. With a QCM system it is possible to monitor the rate of a huge variety of materials.

Although, QCM is a powerful tool for rate monitoring it has certain drawbacks. The QCM system lacks of materials selectivity and thus it is not possible to control more than one source at a time. In addition, the frequency change is nonlinear with deposited mass on the crystal which lead to an increasing error of the monitored rate. External parameters like temperature, film stress or oxidation conditions also leads to errors in the frequency measurements and even affect life time of the crystals. Spectroscopic methods like electron impact emission spectroscopy (EIES) technique overcome these disadvantages but on the other hand complicate the rate monitoring and control.

5.2 *Ex situ* techniques

5.2.1 X-ray diffraction

X-ray diffraction (XRD) is a powerful non-destructive analysis method for solid state matter. It is based on the interaction of X-rays and the outer electron shells in solids. It provides information about crystal structure and, thus, structure related parameters like lattice constants etc. Detailed information on this analysis method are beyond the scope of this thesis and can be found in reference [123].

During this work two different X-ray diffractometers were used; a Siemens D5000 which later was exchanged by a Rigaku SmartLab Thin Film Diffractometer. The Siemens D5000 was equipped with a Cu-anode providing radiation with a wavelength of 1.5406Å (Cu-K_α) in combination with a secondary (111) graphite crystal monochromator. The D5000 operates with a Bragg-Brentano geometry, a maximum acceleration voltage of 40 kV and a maximum emission current of 50 mA.

The Rigaku SmartLab Thin Film Diffractometer is equipped with a 9 kW rotating anode. The target is a copper target which provides X-rays with a wavelength of 1.5406 Å. A voltage between 20-45 kV and a current between 2-200 mA can be applied. The Eulerian Cradle can perform measurements with θ_s/θ_d coupled or independent of each other. In addition, χ-scans between -5° – 95° with a step size of 0.001° and ϕ-scans between -180° – 180° with a step size of 0.002° are possible. The height of the sample table can be adjusted between -4 to 1 mm with a 0.0005 mm step. For a perfect surface alignment the x/y-stage can be tilted in x- and y-direction between -5° to 5° (0.002° step size). The detector is a NaI scintillation counter coupled with a photomultiplier with preamplifier. The X-ray optics like monochromators, collimators etc. can be selected according to the measurement needs. For most of the measurements in this work a 2-bounce Ge (220) primary monochromator was used. The measurements were performed in a parallel beam geometry.

The SmartLab software “SmartLab Guidance” was used to control the XRD-device and to program the single measurements steps. Each sample was aligned for the sample surface and usually for a strong substrate or film peak. For the ϕ-scans in addition the samples were aligned for a correct in-plane alignment using the x/y-tilt of the stage using a substrate peak. In rare cases an optical alignment had to be performed before the measurements. This was only necessary when the optics were changed.

For ϕ-scans the sample was glued to the x/y-table with a double-sided adhesive tape. The SmartLab Guidance software has an integrated crystal simulation part. By introducing the film/substrate details of the samples including atomic positions and lattice parameters the software is able to calculate all reflections of the sample system. With that information it is possible to choose appropriate reflections of the film and the substrate and the goniometer automatically sets the correct positions for ω, 2θ and χ. First, a ϕ-scan of a specific substrate reflection $(hkl)_s$ is performed followed by a ϕ-scan of a specific film peak $(hkl)_f$ without altering any alignment.

The ω-scan which is often called "rocking curve" is done in a similar way as the $2\theta - \theta$ measurement. But in this case the detector arm is fixed at a specific peak position while only the source arm moves over a specified angle range. To determine the full width at half maximum (FWHM) of the X-ray reflections the peaks were fit by either using Gauss function or by using Lorentz function. The first and mostly used one is the Gauss function:

$$g(x) = \frac{A}{\sigma\sqrt{2\pi}} e^{-\frac{1}{2}\left(\frac{x-\mu}{\sigma}\right)^2} + y0 \tag{5.2}$$

where σ represents the FWHM.

The second function is the Lorentz function:

$$l(x) = \frac{2A}{\pi} \cdot \frac{\sigma}{4\left(x-\mu\right)^2 + \sigma^2} + y0 \tag{5.3}$$

Again σ corresponds to the FWHM.

To evaluate the measured X-ray diffraction patterns, they were compared to published data of the same material. For this purpose the ICCD included in the software PDXL was used.

The Nelson-Riley method for exact determination of lattice parameters [124]

One essential part for the analysis of thin films is the determination of lattice parameters from X-ray measurements. In this thesis, especially the determination of the c-axis lattice parameter from $2\theta - \theta$-scans is of high importance. But there are several errors which influence the determination of lattice parameters like absorption of the X-ray beam in the sample. This systematic errors vanish for $\theta = 90°$. Therefore, the standard way to determine the lattice parameters was to plot the angle values of a taken diffraction pattern versus a function of the Bragg angle. For the actual parameter determination an extrapolation to a value corresponding to $\theta = 90°$ was done. However, for this method a correct function which includes all the systematic errors was not found and thus the errors could be neglected partially only.

Nelson and Riley were the first who investigated this issue systematically with Cu_9Al_4 specimens. They prepared samples from the annealed alloy and measured them with X-rays. The results were plotted against different functions. The functions were chosen in such a way that most of the systematical errors were considered. A detailed description can be found in [124]. The function where the best results were achieved is given in equation 5.4.

$$f(x) = \frac{1}{2}\left(\frac{\cos^2\theta}{\sin\theta} + \frac{\cos^2\theta}{\theta}\right) \tag{5.4}$$

For the determination of the lattice parameters the calculated lattice parameters for each peak position of the X-ray measurements were plotted against equation 5.4 with corresponding θ. This plot was fit linearly and the y-axis intercept was determined as the lattice parameter.

5.2.2 Resistivity measurement

To determine the superconducting transition temperature the resistivity versus temperature behaviour was measured using the four-probe technique. For that a constant current was applied through two outer contacts of the measurement device. By measuring the voltage between two contacts which are situated between the outer current contacts the resistivity could be determined. For that the contacts of the measurement device are brought in contact with silver pads which were evaporated through a mask onto the film. The silver pads have the advantage of realizing a good electrical contact between sample and measurement pins and at the same time ensuring a well defined distance between the inner contacts. The last mentioned point is crucial for resistivity determination. The four probe measurement has the advantage that an error due to contact resistance and/or lead resistance can be eliminated. The measurement stick is shown in figure 5.2.

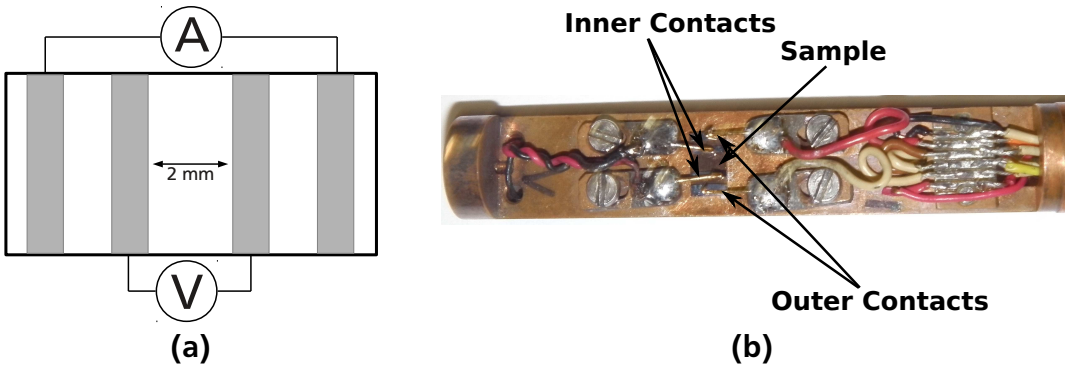

Figure 5.2: a) Schematic illustration of the sample set up for resistivity measurements. b) Picture of the four-probe measurement dip stick used for the resistivity versus temperature measurement. The sample is placed on a copper piece and fixed by copper contacts. The measurement current is applied through the outer contacts while the voltage is measured through the inner contacts.

As a current source a Keithley current source model 6221 was used. For the measurement of the voltage a Keithley nanovoltmeter model 2182 A was utilized and temperature determination was done by a LakeShore calibrated silicon diode model DT-670D-SD. Temperature determination was done by measuring the voltage of the diode since its resistivity is temperature dependent.

For the measurement, the dip stick including the sample was manually introduced into a liquid helium dewar. Temperature of the sample was varied by changing the distance

between liquid helium level and sample stage. For recording the measurement data like current, voltage, temperature etc. a custom programmed LabView software was used. The software uses a look up table to get the correct temperature value out of the silicon diode's voltage.

Measuring the temperature behaviour of the resistivity of the samples from room temperature down to 4.2 K was performed in the liquid helium dewar whereas for the measurement ranging below 4.2 K, an Oxford cryostat was used. The cryostat is capable of a temperature range between 300 K and 1.5 K. For the measurement inside the cryostat the same dip stick was used. Beside the silicon diode mentioned above mounted on the sample stick the temperature is also measured inside the sample chamber. While for temperature control in this case another custom written LabView program was used, the same program mentioned above was used for data recording.

5.2.3 Superconducting Quantum Interference Device

A transition in the temperature behaviour of the resistivity is only an indication for the superconducting nature of a sample. To confirm superconductivity, the Meissner effect (see section 2.2) has to be proven. For that the magnetic susceptibility versus temperature was measured using a superconducting quantum interference device or short SQUID. In principle a SQUID does not measure the magnetic susceptibility of a sample but the magnetic response of the sample to an external applied magnetic field. A SQUID is a powerful tool to detect very low magnetic moments down to 10^{-8} emu using two Josephson junctions (in DC-SQUIDs) or one Josephson junction (in RF-SQUIDs). This high sensitivity is possible due to measurements of the changes in magnetic fields associated with one flux quantum. For the magnetic measurements in this work a Magnetic Property Measurement System (MPMS) supplied by Quantum Design was used. The measurement in the MPMS are done through the movement of the samples through a system of superconducting coils, the so called "pickup coils". The movement of the sample induces a voltage in the coils, which are inductively coupled to the SQUID sensor (Figure 5.3).

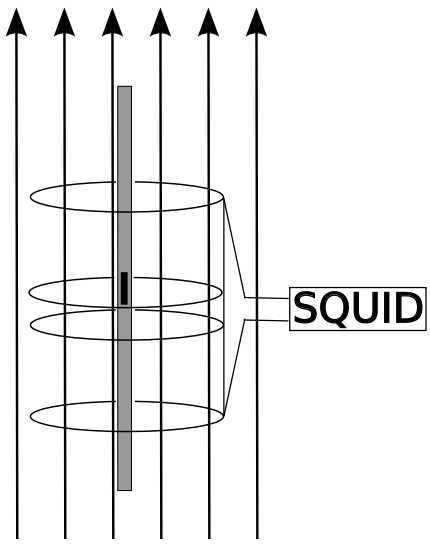

Figure 5.3: Schematic illustration of the SQUID.

This results in an output-signal, which is proportional to the current flowing in the input coils. With this “current-to-voltage converter” it is possible to measure very low magnetic moments of thin film samples. The superconducting magnets are installed inside a dewar filled with liquid helium. The sample space consists of a small chamber which also can be cooled by the helium. To reach temperatures below 4.2 K this small sample space is filled completely with liquid helium and then pumped down. As a sample holder a commercially available straw was used. The sample is placed in the middle of the straw, while the straw is placed in the middle of the magnet system of the MPMS. For the measurement it is crucial to determine the exact sample position inside the MPMS. For position detection, the sample is moved trough the coils. The maximum of the response signal indicates the sample position. The MPMS used in this study is equipped with a Reciprocating Sample Option. This option enables measurements for magnetic moments down to 5×10^{-9} emu. Further information can be found in reference [125].

6 Growth of arsenic free thin films of '1111'-type pnictide superconductors

Part of this thesis is to grow superconducting thin films of arsenic free pnictide compounds. It was already shown, that a substitution of arsenic by phosphorus is possible. So a substitution of the toxic arsenic by elements from the same periodic group is the next step in the search for arsenic free pnictide superconductors. Reports on a similar structure containing antimony instead of arsenic were not made. Nevertheless, in 2012, Muir *et al.* [126] tried to synthesize an antimony containing '1111'-structure without success. In addition, they did ab-initio density functional theory (DFT) calculations for LaFe*Pn*O where *Pn* is phosphorus, arsenic and antimony. The results suggest, that LaFePO and LaFeAsO form stable compounds. But LaFeSbO seems to be a metastable compound according to their calculations. To confirm the metastability of LaFeSbO they calculated the phonon spectrum of the compound and found no imaginary phonon frequencies. This indicates a lack of lattice instabilities which means a local minimum for the formation energy of LaFeSbO can be found. In conclusion it can be said, that in principle a formation of LaFeSbO is possible. But because of energetic reasons under normal conditions the formation of a $ThCr_2O_2$ type La_2Sb_2 is more favourable than the formation of LaFeSbO.

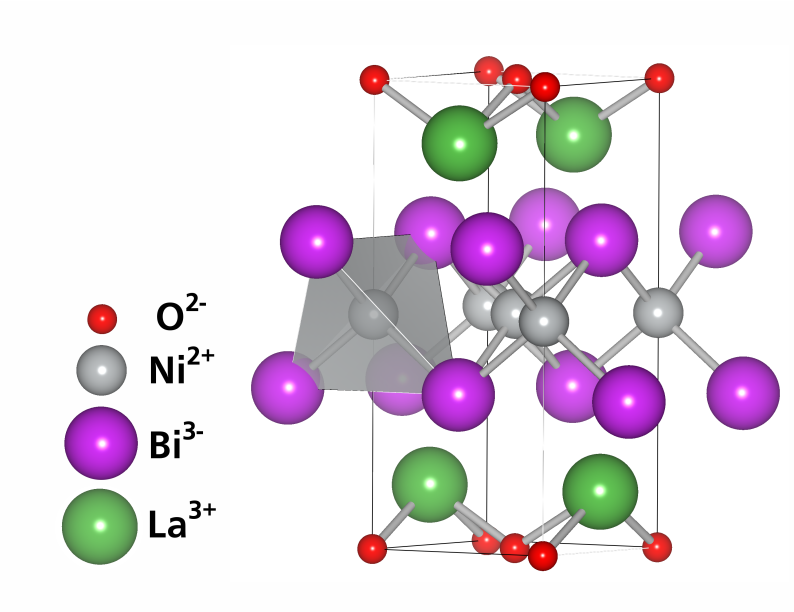

Figure 6.1: Crystal structure of LaNiBiO. The tetragonal crystal structure shows the same type of layers as it is observed in LaFeAsO with Fe replaced by Ni and As replaced by Bi.

However, in 2008 Kozhevnikov *et al.* [127] reported the synthesis of a bismuth containing LaNiBiO '1111' type structure. It is reported, that with oxygen deficiency this compound is superconducting below temperatures of $\sim$ 4 K. Although, this superconductor has a

very low T_C compared to the 56 K of present oxyarsenides, the identical crystal structure ($P4/nmm$, figure 6.1) with similar lattice constants ($a = 4.262$ Å, $b = 8.888$ Å), a similar ρ(T) behaviour and the absence of the noxious arsenic make LaNiBiO a perfect candidate for investigating the growth parameters of a arsenic free '1111'-type superconductor.

6.1 Growth of $LaNiBiO_{1-x}$ thin films

First attempts to grow arsenic free films were made during my diploma thesis (November 2008 – May 2009, TU Darmstadt) [128]. Here, the main results will be described in a brief summary.

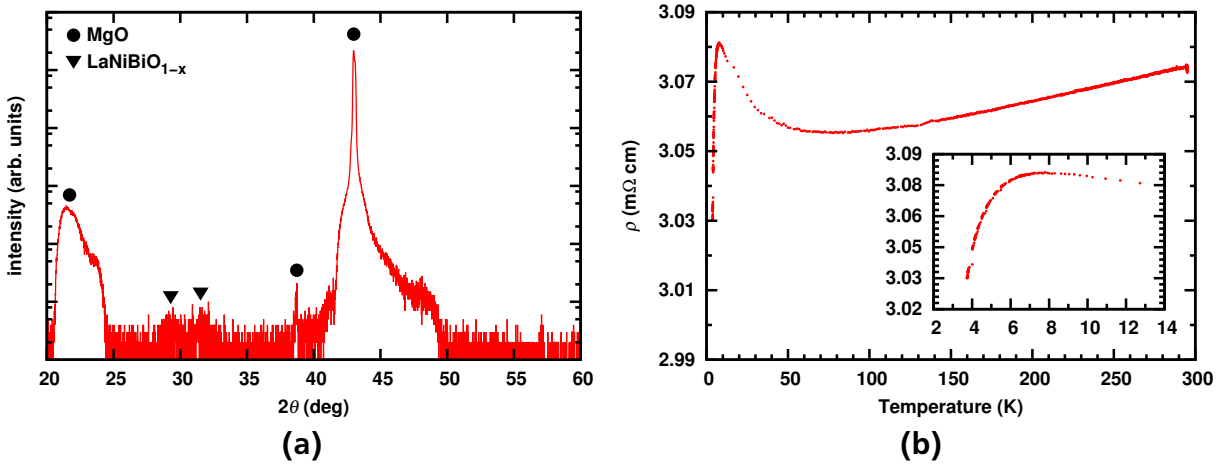

Figure 6.2: a) $2\theta - \theta$ measurement of a $LaNiBiO_{1-x}$ film grown with MBE. The measurement was done with the Siemens D5000 b) Temperature behaviour of the resistivity of a $LaNiBiO_{1-x}$ film grown with MBE.

The growth temperature was changed between 450 °C and 700 °C. All temperatures resulted in polycrystalline films (revealed by *in situ* RHEED measurements and *ex situ* XRD measurements). Best results were obtained at 450 °C, although there is no clean phase formation but only a small portion of the desired $LaNiBiO_{1-x}$ phase. Higher temperature led to La_2O_3 formation. Figure 6.2a shows an XRD pattern of a $LaNiBiO_{1-x}$ film grown at 450°C.

Mostly, the influence of the oxidation conditions and the growth temperature were studied. The radical oxygen flow was varied in a range of 0.15 sccm to 1.0 sccm at a radical power of 200 W. For that, the growth temperature were kept at 450 °C. The films grown at radical oxygen flow rates between 1.0 sccm and 0.4 sccm were insulating and transparent. No clear peaks could be identified in XRD measurements. Below 0.4 sccm the films were conducting and the room temperature resistivity decreased monotonically with decreasing flow rate. For oxygen flow rates below 0.25 sccm the films showed a superconducting transition onset. The highest temperature for the onset of ~ 5.5 K were achieved for 0.17 sccm. Figure 6.2b shows a typical $\rho - T$ curve of the films grown at 450 °C and 0.17 sccm.

The major challenge in growing this compound as a thin film by MBE is to set the right parameters to get the correct stoichiometry and good crystallinity. Higher temperature usually leads to better results regarding the crystal quality. But since the Bi sticking

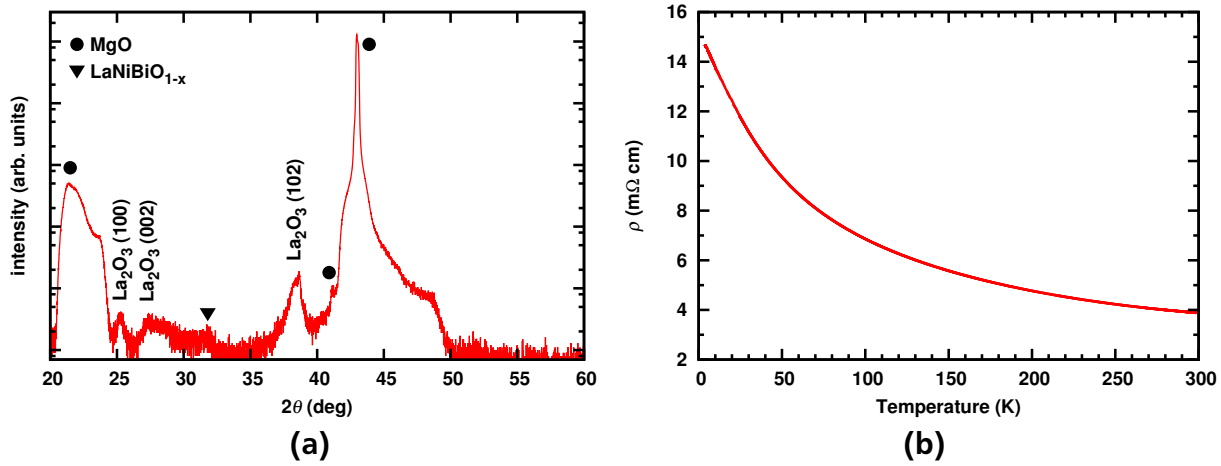

Figure 6.3: a) $2\theta - \theta$ measurement of the $LaNiBiO_{1-x}$ film grown at adjusted parameters according to the ICP-OES measurement. b) Resistivity vs. temperature measurement of the $LaNiBiO_{1-x}$ film grown at corrected parameters. The behaviour is clearly semiconducting with a room temperature resistivity of ~ 4 mΩ cm. The measurements were done on the Siemens D5000.

coefficient is very low, higher deposition temperatures lead to a huge Bi loss. In addition, growing two different anions (O^{-2} and Bi^{-3}) within the same structure is very challenging. And the oxygen content is crucial for the superconducting properties of the samples. The next section describes the attempts to optimize the growth parameters for the deposition of $LaNiBiO_{1-x}$ thin films.

6.2 Optimization of deposition parameters for $LaNiBiO_{1-x}$ thin film growth

As mentioned before optimization of the growth parameters in MBE is a very challenging task to perform since all the parameter influence each other. One important factor is the correct ratio of the elemental rates. This assign mainly the composition of the grown films. For that, the grown films are analyzed for their stoichiometric composition and the rates are set accordingly. Since some starting parameters were already established from the work done before in the diploma thesis and also an ICP-OES measurement for composition study was done, it was tried to adjust the rates according to the values gained from the measurement to set a stoichiometry of 1:1:1 for lanthanum, nickel and bismuth. Table 6.1 shows the values from ICP-OES measurement and the rates before and after the adjustment. Since the lanthanum is very sensitive to oxygen and the overall stability of the lanthanum source at higher rates is rather critical the lanthanum rate was reduced a little bit and the other rates were changed accordingly. The other parameters like oxygen flow (0.17 sccm), radical source power (200 W), substrate temperature (480 °C) and duration of deposition (10 min) were kept the same. Figure 6.3a shows the corresponding X-ray diffraction pattern of the film grown with corrected rates on a MgO substrate. It can be seen, that the film is polycrystalline in nature which was already known from the RHEED picture taken during deposition. The (200) substrate peak at 42.93° can be clearly seen. The reflection at 21.45° corresponds to the $\lambda/2$ peak of the (200) MgO reflection. The reflections at 38.43° and

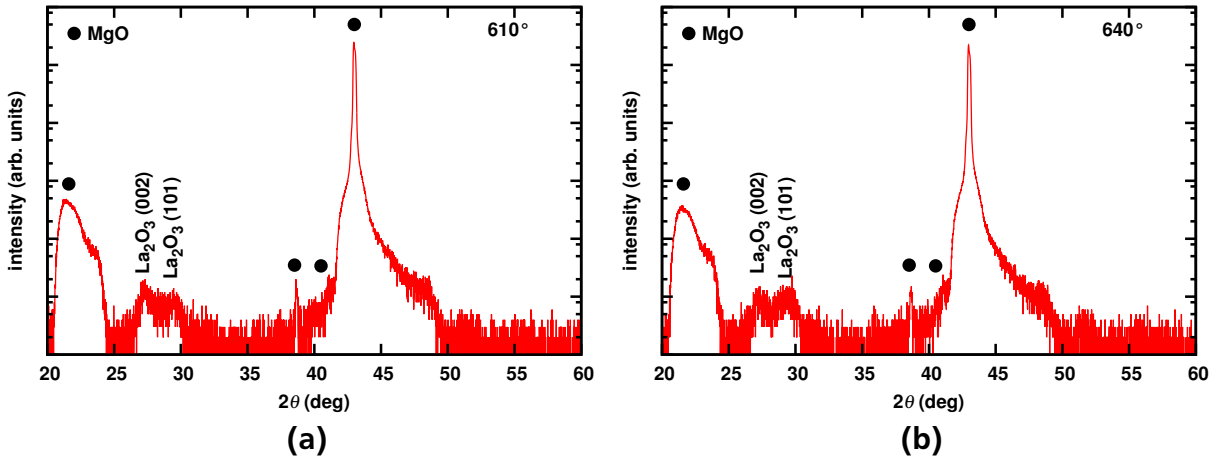

Figure 6.4: $2\theta - \theta$ measurements of the $LaNiBiO_{1-x}$ films grown with higher bismuth rates and substrate temperatures of a) 610 °C and b) 640 °C. The measurements were done on the Siemens D5000.

41.20° are from Cu-K_β and tungsten radiation, respectively. At 25.24°, 27.5° and 38.1° reflections of a La_2O_3 phase are observed [129]. Only at 31.56° a very small peak could be identified to be from the $LaNiBiO_{1-x}$ phase. This result is not very convincing. In addition, the resistivity measurements show a clear semiconducting behaviour with a room temperature resistivity of ~ 4 mΩ cm (figure 6.3b).

Table 6.1: ICP-OES results of the superconducting $LaNiBiO_{1-x}$ films. The table shows the rates before the adjustment, the composition ratio according to lanthanum and the rates after the adjustment to get a stoichiometry of 1:1:1.

Element	rate (Å/s)	ratio	adjusted rate (Å/s)
La	0.75	1	0.68
Ni	0.22	0.95	0.21
Bi	0.8	0.74	0.9

These results show the difficulty in finding the correct growth parameters. The challenge is to suppress the formation of the La_2O_3 phase and enhance the growth and crystallinity of the $LaNiBiO_{1-x}$ phase. To do that some attempts at higher growth temperatures were done. Here the bismuth content is a crucial point. Since the sticking coefficient of bismuth is rather low it is challenging to control the bismuth content in the structure at elevated temperatures. To perform the growth experiments at higher deposition temperatures (610°C) the bismuth rates were increased by more than 25% to compensate the expected loss. For a growth temperature of 640°C the bismuth rate was increased by 40%. In addition, since the last results with reduced lanthanum rate were not that promising the lanthanum and nickel rates were changed back to the former values (corrected according to the ICP-OES results).

Figure 6.4 shows the $2\theta - \theta$ measurements of the films grown at elevated temperatures of 610 °C and 640 °C. The image on the left side shows the film grown at 610°C. It can

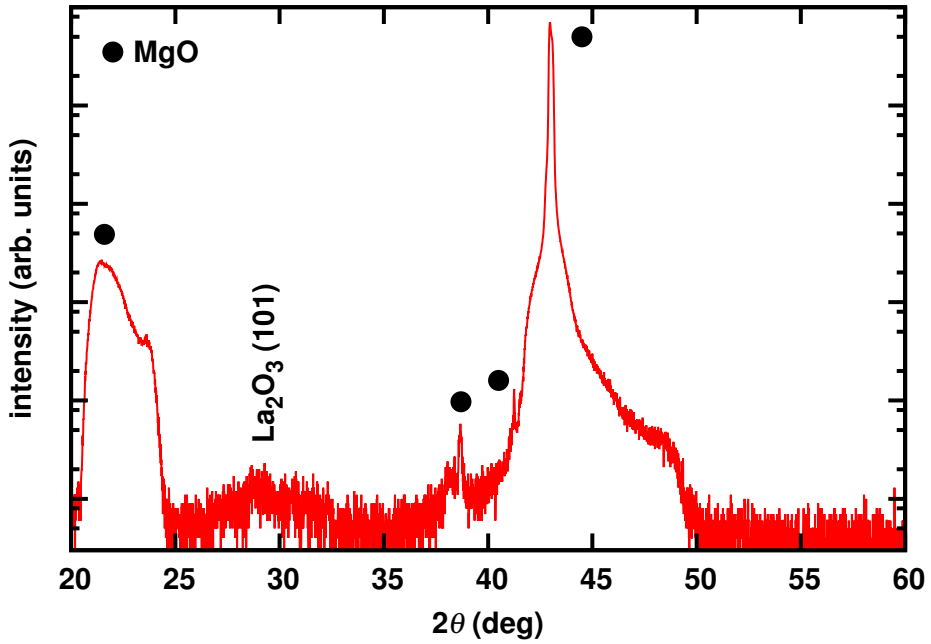

Figure 6.5: $2\theta - \theta$ measurement of the $LaNiBiO_{1-x}$ film grown at a radical source power of 175 W. The measurements were done on the Siemens D5000.

be seen that, although it was grown at higher temperatures, the film is polycrystalline and only La_2O_3 has formed [129]. There is no evidence for the formation of the $LaNiBiO_{1-x}$ phase. Same applies for the film grown at 640°C shown on the right side of figure 6.4. Only the La_2O_3 phase is more prominent. Consequently, the films were insulating directly after deposition. That means, higher deposition temperatures do not favor the formation of $LaNiBiO_{1-x}$ phase, but rather the formation of La_2O_3. In addition, it can be expected that the bismuth content in the film is too low because of the high deposition temperatures which was confirmed by an ICP-OES measurement. The ratio was estimated to be 1:1.4:0.19 for La:Ni:Bi. It can be seen that the bismuth content is very low compared to the other components. This suggests the requirement of a much higher bismuth rate for obtaining stoichiometric $LaNiBiO_{1-x}$ films. But a rate of 1.4 Å/s is already a very high rate and the QCM life is considerably reduced which lead to failure of the crystal in a short time.

Adjusting growth temperature and growth rates according to the composition of the films seems to be challenging. One important factor of the growth of oxygen containing compounds are the oxidation conditions. Strong oxidation conditions can lead to the formation of metal oxides instead of forming the desired phase. In the films grown so far La_2O_3 is the most prominent impurity phase indicating a too strong oxidation. Different parameters were already tried during the experiments in the diploma thesis to vary the oxygen flow rate at a radical power of 200 W. So first attempts to affect the oxidation of the films was to reduce the power of the radical source. Too low radical powers lead to an unstable plasma and so the power was decreased in small steps. For the first attempt. the power was decreased to a value of 175 W at the best conditions where a transition onset was observed (temperature of 450°C, 0.17 sccm flow rate and elemental source rates according to the not adjusted rates in table 6.1). Below this value the plasma starts to

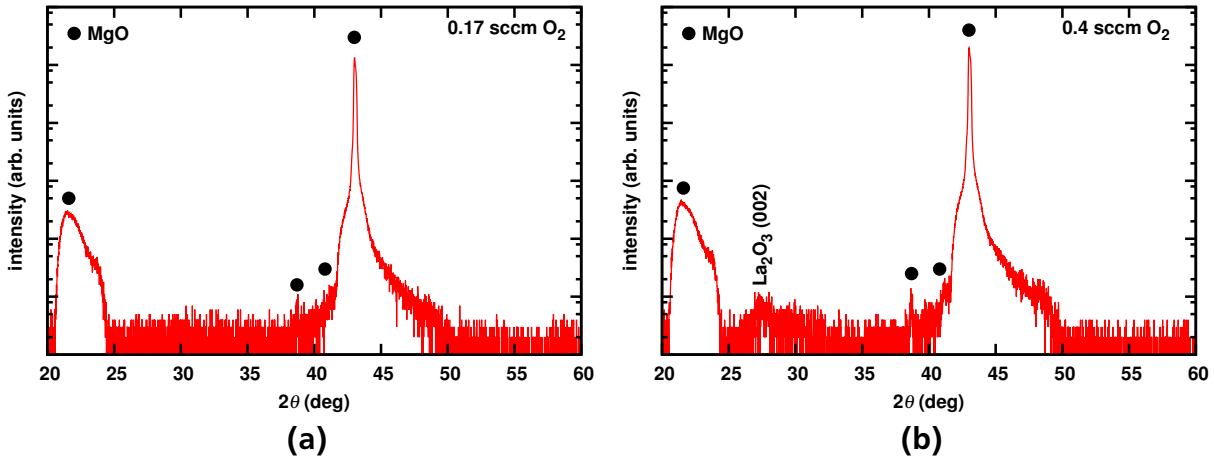

Figure 6.6: $2\theta - \theta$ measurements of the $LaNiBiO_{1-x}$ films grown with molecular oxygen at various flow rates with a) 0.17 sccm and b) 0.4 sccm. The measurements were done on the Siemens D5000.

become unstable at these low flow rates. Figure 6.5 shows the XRD measurement of the resulting film.

However, the La_2O_3 is present in the X-ray diffractogram but not the desired $LaNiBiO_{1-x}$ phase. In the MBE set up used in this work lower oxygen flow rates and lower radical source powers are not possible. As already mentioned a lower radical power would lead to an unstable plasma and the mass flow controller used in this set up is not capable of controlling lower flow rates. But still, lower oxidation conditions for the deposition of $LaNiBiO_{1-x}$ films would be interesting. To achieve lower oxidation conditions molecular oxygen was used instead of the radical oxygen. Two attempts have been done, one with same oxygen flow rate of 0.17 sccm molecular oxygen and one at higher flow rates of 0.4 sccm molecular oxygen. The results are shown in figure 6.6.

The film grown at lower flow rates of molecular oxygen shows no phase formation at all. Only the substrate peaks of MgO can be observed (figure 6.6a). The XRD measurement shown in figure 6.6b shows the results of the film grown at 0.4 sccm molecular oxygen. Beside the substrate peaks only a small peak of the La_2O_3 phase can be seen. In conclusion, the formation of the lanthanum oxide seems to be more favored than the formation of $LaNiBiO_{1-x}$. In addition, the molecular oxygen seems to be too weak to support the formation of the $LaNiBiO_{1-x}$ structure. Since the best results were made with radical oxygen, one last attempt was tried to grow a superconducting film of the $LaNiBiO_{1-x}$ structure. For that the lowest possible oxidation conditions for the MBE set up were set and the rates of the so far best results were used. The X-ray measurements were performed on a new Rigaku machine with high power so more details in the film can be seen. The results are shown in figure 6.7.

It is obvious that with the present set up of the MBE machine it is not possible to decrease the oxidation conditions any further. That means to grow the oxygen containing '1111'-type iron pnictide superconductors with this MBE set up some modifications are necessary like a new mass flow controller for lower flow rates. Kawaguchi *et al.* [87] noticed that a film formation with excess oxygen does not happen for the '1111'-type superconductors.

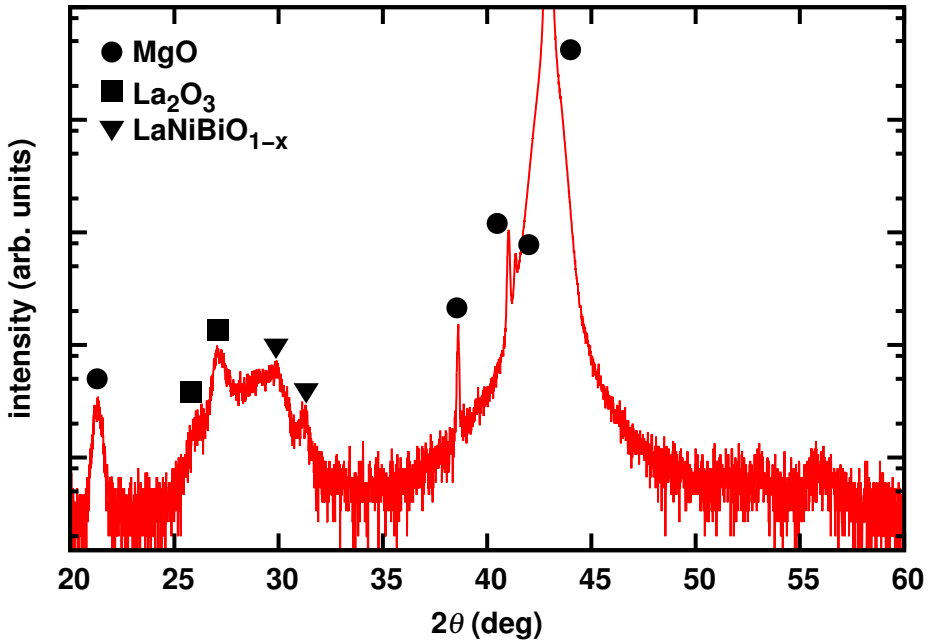

Figure 6.7: $2\theta - \theta$ measurement of a $LaNiBiO_{1-x}$ film grown at the so far best conditions. The film consists of a mixed phase of $LaNiBiO_{1-x}$ and La_2O_3.

They tried to grow a fluorine doped samarium compound of the '1111'-type pnictide superconductors with MBE. Instead of molecular or radical oxygen, iron oxide was used as an oxygen source. The iron oxide was evaporated by effusion cells. With an additional pure iron source they could adjust the oxygen content to their need and even achieve very low oxygen contents. At that time the MBE set up used in this work was not equipped with effusion cells. The evaporation of oxides using electron gun evaporators is not possible.

The work shown here was published in [130].

7 Growth of oxygen free pnictide superconductors

As it was shown in the last section it is challenging to grow oxygen containing thin films with the molecular beam epitaxy. In addition it is special in this compound that there are two anions: oxygen and bismuth. To bring bismuth, naturally a cation, in a negatively charged state while oxygen is present is not that easy. For the bulk samples it is done through a precursor of LaBi. In that compound Bi takes the part of 3- charged cation. From that precursor the '1111'-type superconductors are prepared.

For the film growth in this study the oxidation conditions were too strong. With the MBE set up, used it is not possible to decrease the oxidation any further. Luckily, as shown in chapter 3, there are also pnictide superconductors which do not contain any oxygen. Since the oxygen makes the most trouble for the film growth of pnictide superconductors using MBE, the oxygen free variants are a good starting point to study the general behaviour of such a layered structure containing a pnictide, a rare earth and a transition metal.

For that, the results of the last section give a hint for the choice of parameters to start growing oxygen free '122'-type superconductors, namely $LaNi_2Bi_2$. But one have to keep in mind that the '122'-type compounds do not contain a rare earth but an alkaline earth metal (barium or strontium) which is doped with an alkali metal. This partial substitution results in a hole doping in the structure which leads to superconductivity with T_C as high as 38 K. The idea now is to use lanthanum as a rare earth to grow an electron doped and lanthanum deficient novel class of '122'-type superconductors. The attempts to do this and the results what structure was grown eventually is described in the following sections.

7.1 Growth of "$La_xNi_2Bi_2$" thin films and the process of parameter optimization

The results of the last section about growing $LaNiBiO_{1-x}$ thin films showed the difficulty in handling structures which contain oxygen. And although the results were not the desired one, they gave a more or less good starting point for growing oxygen free compounds. From the ICP-OES measurements (see section 6.2) the ratio of lanthanum to nickel to bismuth is known. For a starting, it was tried to take these values and decrease the lanthanum rate by half to fulfill the requirement of a ratio of 1:2:2 for La:Ni:Bi (table 7.1). But as already mentioned in the introduction to this section, a full 1:2:2 ratio is not possible due to the +3 state of lanthanum. Since, the goal is to grow a lanthanum deficient compound, the lanthanum rate was reduced more than by half and the other rates of bismuth and nickel were slightly increased.

The growth temperature was not changed from the $LaNiBiO_{1-x}$ films to this composition and was set to a value of 480°C (pyrometer measurement on the stainless steel holder near the substrate). The RHEED pattern during the run shows that the film is mostly polycrystalline with a weak indication of a single crystalline phase. Figure 7.1 shows the results of this film. The reflections at $\sim$ 21.5°, at $\sim$38.7° and at $\sim$ 43° of the $2\theta - \theta$

Table 7.1: Starting rates of lanthanum, nickel and bismuth for the growth of $La_xNi_2Bi_2$

Element	rate (Å/s)
La	0.3
Ni	0.24
Bi	0.95

measurement are from the MgO substrate. The two additional reflections at $\sim 25.8°$ and $\sim 27.3°$ can not be identified. They do not belong to a '122'-type structure or to any possible structure of a LaNi, LaBi or $NiBi/NiBi_3$ composition. With the metallic composition of the film one would expect a metallic behaviour of the resistivity versus temperature. Figure 7.1b shows this behaviour at least down to 100 K with a room temperature resistivity of ~ 1 mΩcm. Below 100 K the resistivity starts to increase and the behaviour becomes a more semiconducting one. Reason for that could be the polycrystalline nature of the film and mixture of different phases. In addition it was observed that the film starts to decompose rather quickly when stored in air. This behaviour was discovered in X-ray measurements where no reflections were observed anymore after one day of exposure of the film to air. In addition the temperature behaviour of the resistivity changed. The room temperature resistivity changed from ~ 1 to ~ 10 mΩcm and the overall behaviour changed to a total semiconducting one with increasing resistivity with decreasing temperature (see the inset of figure 7.1b).

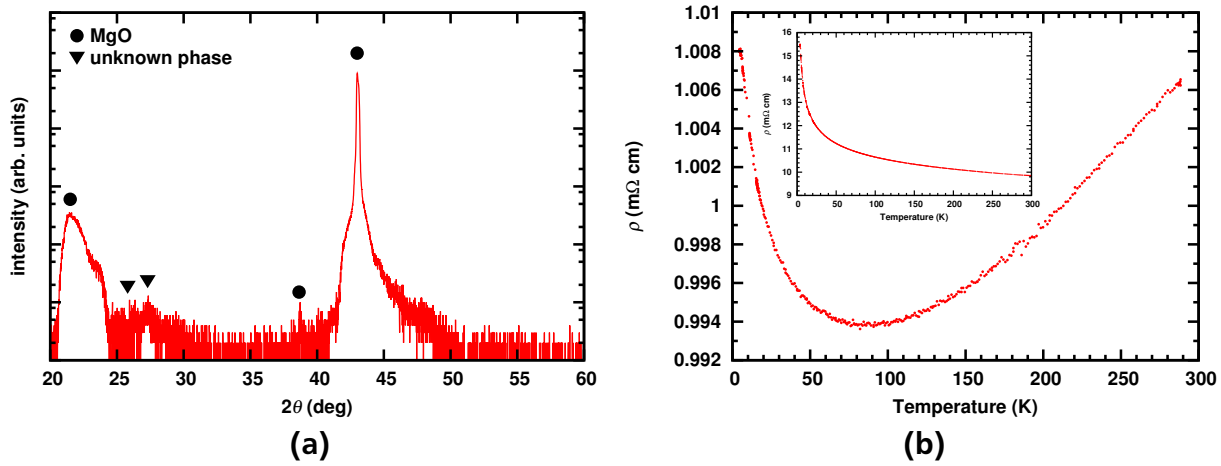

Figure 7.1: a) $2\theta - \theta$ measurement of the first attempt to grow a $La_xNi_2Bi_2$ film. The measurement was done with the Siemens D5000. b) Resistivity versus temperature measurement of the $La_xNi_2Bi_2$ film. The inset shows the resistivity versus temperature measurement of the film after one day of exposure to ambient atmosphere.

The weak reflections of the X-ray measurement suggest a substrate temperature increase to improve the crystal quality of the film and to support a proper phase formation. For that the substrate temperature is increased by 120 °C from 480 °C to 600 °C. To overcome the bismuth loss because of the higher temperature, the bismuth rate was increased by

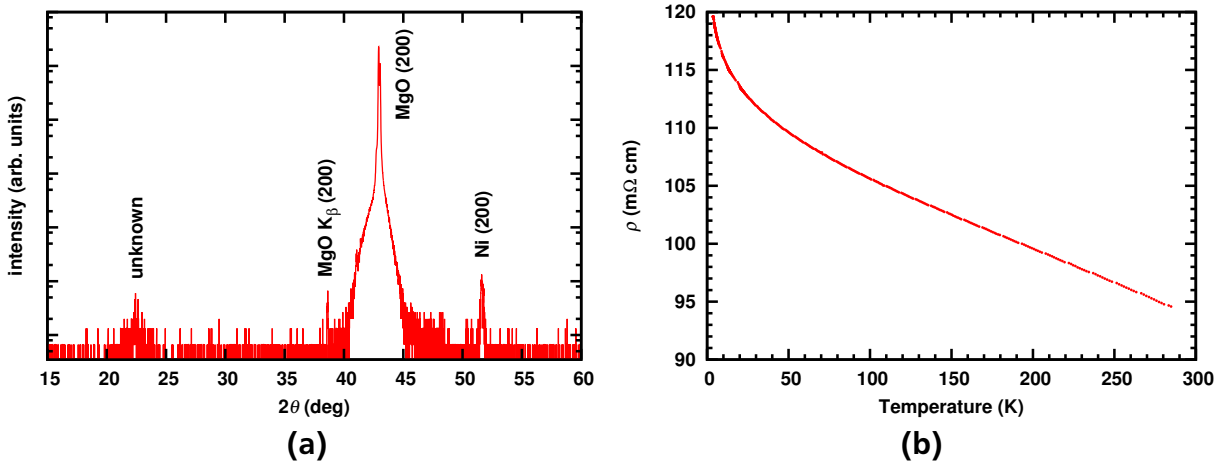

Figure 7.2: a) X-ray measurement of the $La_xNi_2Bi_2$ film grown at a substrate temperature of 600 °C. b) shows the temperature behaviour of the resistivity of the $La_xNi_2Bi_2$ film.

∼10 % to 1.05 Å/s. The other parameters were kept the same. The RHEED pattern of the film observed at the end of the deposition process reveals a polycrystalline nature of the film. Figure 7.2 shows the characterization results of the film. The X-ray measurement shown in figure 7.2a confirms the polycrystalline phase of the $La_xNi_2Bi_2$ film. Beside the substrate peak an unknown phase at ∼ 22.5° is observed which seems to be polycrystalline. In addition the (200) peak of $Fm\bar{3}m$ crystallized nickel can be seen at ∼ 51.75° [131].

The resistivity vs. temperature measurement shown in figure 7.2b reveals an increasing resistivity with decreasing temperature. Down to a temperature of ∼ 50 K the resistivity increases in a linear manner. Below 50 K the increase is more than proportional. The absolute resistivity value is also rather high and varies in a range from ∼ 95 mΩ cm at 300 K to almost 120 mΩ cm at 4.2 K. The RHEED observation of the $La_xNi_2Bi_2$ compound shows streaky nature at the beginning of the growth. As the film growth proceeds, the streaky RHEED pattern changes to a faint ringlike pattern and continues like that till the end of the film growth. One possible scenario is that initially the '122' phase tries to grow epitaxially on the substrate and as the growth proceeds further, off composition or unfavorable growth conditions lead to the formation of a polycrystalline film. The nickel observed in the X-ray measurement is not seen in the RHEED pattern. It is likely that it precipitates on top of the film as small islands. The resistivity of the film is not affected by the nickel since the resistivity for pure nickel is 69.3 $\mu\Omega$ cm [132] which is much lower than the measured 100 mΩ cm for the $La_xNi_2Bi_2$ films. The higher temperature used for film growth leads to a bismuth loss which could not be compensated by the higher bismuth rate. As already mentioned earlier an even higher bismuth rate leads to crystal failure of the QCM system rather quickly. It is known from the fabrication of MgB_2 films by MBE that a high growth temperature is not possible because of the high vapor pressure of Mg. Above a temperature of 300 °C there is a significant loss of magnesium observed inside the structure. To overcome the Mg loss the films are prepared at lower growth temperatures in a range of 260–280 °C [133]. The knowledge about this fact lead to the idea to lower the growth temperature to compensate the bismuth loss of the films. Since it was already seen that a

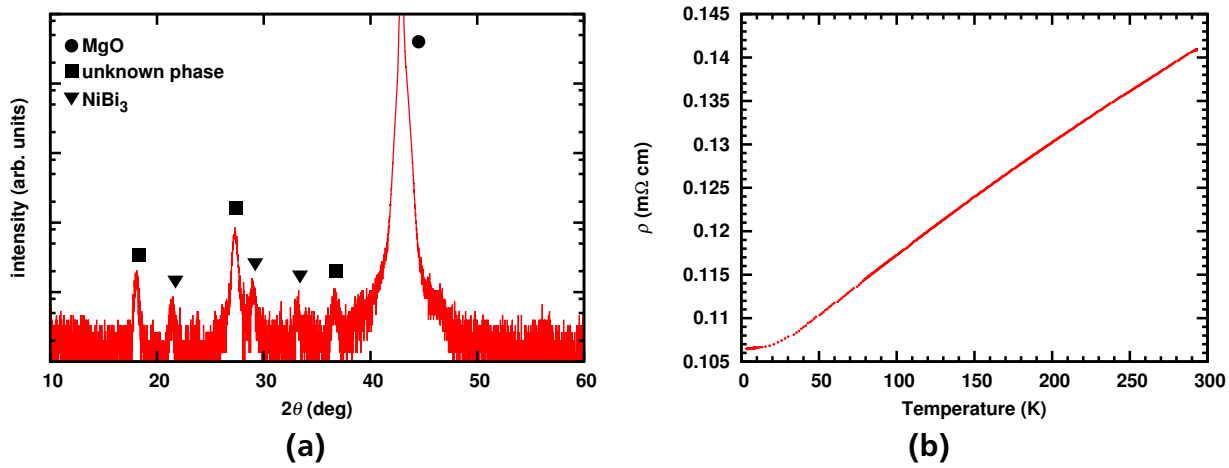

Figure 7.3: a) X-ray measurement of the $La_xNi_2Bi_2$ film grown at 420 °C. Beside a polycrystalline $NiBi_3$ phase another at this point unknown phase is observed. It is interesting to see that the unknown phase seems to grow epitaxially. b) temperature behaviour of the resistivity. Over the whole temperature range a metallic behaviour can be observed until it flattens below 10 K.

temperature of 480 °C also does not lead to a phase formation the deposition temperature was lowered further by another 60 °C to a value of 420 °C. The other parameters including the bismuth rate were kept the same.

Figure 7.3a shows the results of the lower growth temperature attempts. This time there are more reflections in the diffractogram. Again there is the unknown phase already seen in the last film grown at 600 °C. But this time there are much more reflections which appears at positions of 18.2°, 27.4° and 36.6°. The periodical repetition of the reflections suggest a *c*-axis oriented growth of a compound with *c*-axis lattice parameter of 9.8 Å, which mean the observed reflections correspond to (002), (003) and (004) reflections. This does not correspond to a *c*-axis of the '122' pnictide phase. The '122' pnictides crystallize in the body-centered-tetragonal $ThCr_2Si_2$-type structure (space group *I4/mmm*) in which the odd reflections are forbidden. The information gained from the X-ray measurement are not enough to determine the correct crystal structure. So at this point it is not clear, what compound is growing here.

Beside the unknown epitaxial phase, a polycrystalline $NiBi_3$ phase is observed. This is an indication that the Bi loss could be compensated by the reduction of the growth temperature. The additional nickel which lead to the metallic Ni peak at higher temperature now forms the $NiBi_3$ [134, 135]. Figure 7.3b shows the temperature behaviour of the resistivity. Between 300 K and 10 K the resistivity shows a metallic behaviour with a room temperature resistivity of ~ 0.14 mΩ cm and a resistivity of 0.106 mΩ cm at 10 K. Below 10 K the curve flattens and no superconducting transition onset could be observed down to 4.2 K.

Although the formation of the unknown phase is not expected and the desired '122' phase is not achieved the results are promising to grow a novel compound with a high quality. To grow the new phase and study the physical properties could be interesting. So in the next paragraphs it is described how the growth parameters were varied to find optimal growth conditions for the unknown phase and to identify the compound. Since

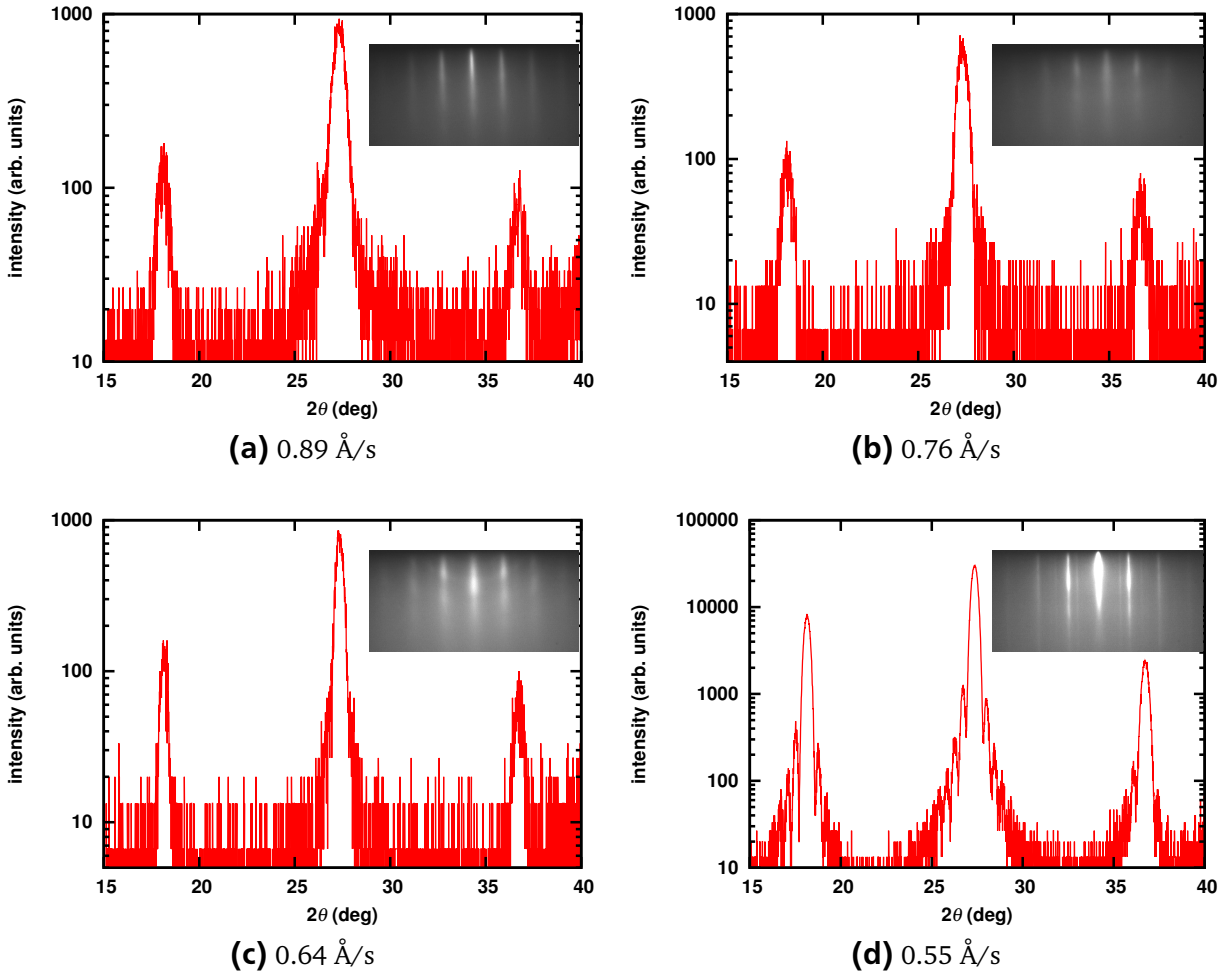

Figure 7.4: $2\theta - \theta$ measurements of a series of $La_xNi_2Bi_2$ films grown at different bismuth rates. The insets of each image represents a RHEED picture taken directly after the film growth. The average thickness of the films is ∼30 nm.

the deposition temperature of 420 °C seems to be sufficient for the growth of the unknown phase, the bismuth rate was decreased systematically in steps of 15% beginning with 0.89 Å/s. Figure 7.4 shows the results of these attempts. As it can be seen, that the phase forms at all these bismuth rates, but the quality of the films increase with decreasing bismuth rate. As a measure for the film's quality the FWHM of the (003) reflection of the $2\theta - \theta$ was determined by a Gaussian fit of the peak.

Figure 7.4a shows the XRD measurement of the film grown at 0.89 Å/s and the inset shows the RHEED image taken directly after growth. The RHEED azimuth was along <100> of the MgO substrate and indicates a smooth and epitaxial growth of the film. The X-ray measurement does not show any impurity phase in the scanned range between 15° to 40°. Only three reflections at 18.1°, 27.4° and 36.7° are observed which could be indexed as (002), (003) and (004) reflections for a film with a *c*-axis lattice parameter of 9.8 Å confirmed by the Nelson-Riley Method of the reflections. The intensity of the (003) reflection is around 1000 counts/s and the FWHM of the (003) reflection determined from the Gaussian fit is around 0.61°.

With decreasing bismuth rate the quality of the RHEED patterns improves. While the RHEED image of the film grown at a bismuth rate of 0.76 Å/s shown in the inset of figure 7.4b is very similar to the one of the film grown at 0.89 Å/s and no improvement can be seen, the RHEED pattern of the film grown at 0.64 Å/s shows a brighter appearance. The best results are obtained with the film grown at a bismuth rate of 0.55 Å/s. The RHEED pattern of this film is shown in the inset of figure 7.4d and shows bright and thin streaks indicating a very smooth and epitaxial film growth. So, according to the RHEED pattern of a $La_xNi_2Bi_2$ film deposition at lower bismuth rates seems to be more promising for the growth of high quality films.

The better deposition conditions for the $La_xNi_2Bi_2$ films at lower bismuth rates are also confirmed by the intensity of the (003) reflection of the $2\theta - \theta$-scan. While the X-ray intensity of the (003) peak for the films grown at a bismuth rate of 0.76 Å/s and 0.64 Å/s is similar to the one for the film grown at 0.89Å/s, the intensity increases significantly for the films grown at 0.55 Å/s (figure 7.4d). The (003) reflection of the $2\theta - \theta$-scan of this film has an intensity of roughly 50.000 counts/s, which differs by a factor of 50 to the films grown at the higher bismuth rates. This measurement also shows a unique feature in this series of films. It can be seen that the reflections have Laue oscillations which is an indication for a good coherence between film and substrate. The Laue oscillations are asymmetric on both sides of the reflections indicating a variation of composition along the film thickness. From the Laue oscillations it is possible to roughly estimate the film thickness. It was estimated to be 25.6 ± 0.1 nm.

To gain a rough idea about the films quality the FWHM of the (003) reflections of the various films was compared. Of course, one has to be careful about the conclusion which can be made out of the FWHM of the $2\theta - \theta$ measurement. This value does not reflect the crystal quality of the films directly. For that one should rely on the FWHM of the rocking curve (omega scan) of a specific reflection. The FWHM of the $2\theta - \theta$ measurement is a measure for the crystallite size. It only can give a rough indication for the films quality and to compare different films within a series with each other. From the film grown at the highest bismuth rate in this series (0.89 Å/s) with a FWHM of the (003) peak of 0.61° to one grown at the lowest rate of 0.55 Å/s the FWHM decreases constantly. The lowest value is reached for the last mentioned film with a FWHM of 0.33°. This is less than half of the value determined for the film grown at the highest bismuth rate and indicates the better crystallinity of the film. The *c*-axis lattice parameter of the $La_xNi_2Bi_2$ films does not vary much in this series of bismuth rates. The value determined by the Nelson-Riley method is in the range between 9.78 Å and 9.79 Å. With an estimated error of 0.1 Å, it can be said that the *c*-axis lattice parameter is constant for the whole series and is independent of the bismuth content.

To get an idea about the crystal quality the rocking curve of the best film was measured and is shown in figure 7.5. The curve is fitted with a Gaussian function to determine the FWHM. From the fit, a FWHM of 0.07° was estimated. This value confirms the good crystal quality of the film which was already indicated by the RHEED pattern, the Laue Oscillation and the FWHM of the $2\theta - \theta$ scan and the higher intensity of the X-ray peaks. However, it should be noticed that the background of the curve is rather high which is an indication for a high density of defects in the interface of substrate and film. Another property of the film was observed after one day while the film was exposed to ambient atmosphere. The film starts to decompose within one day and no X-ray reflections can be observed anymore.

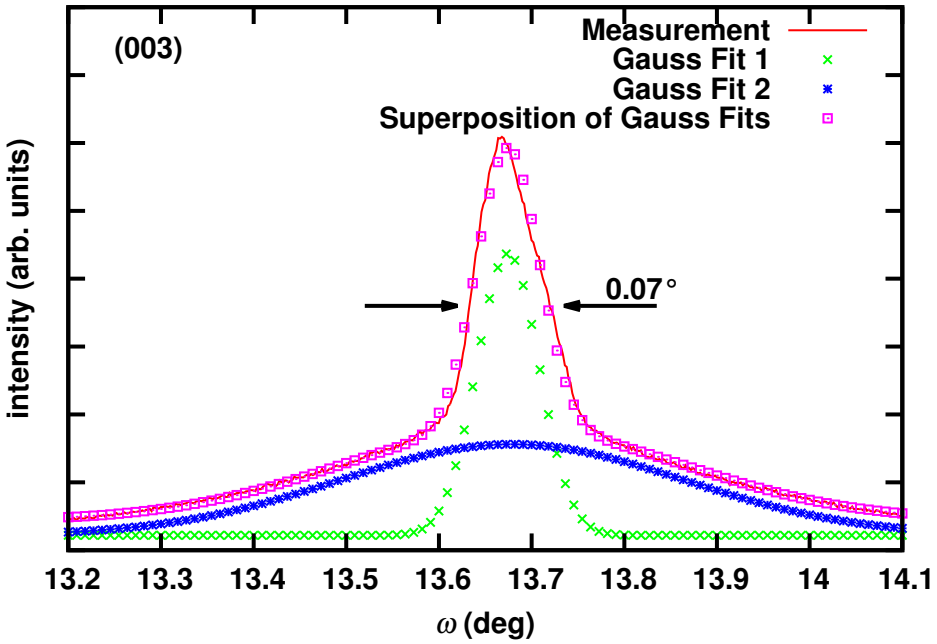

Figure 7.5: Omega scan of the $LaNi_2Bi_2$ film grown with a bismuth rate of 0.55 Å/s.

Parameters of 0.3 Å/s for the lanthanum rate, 0.24 Å/s for the nickel rate, 0.55 Å/s for the bismuth rate and a growth temperature of 420 °C result in quite good RHEED and X-ray patterns. Based on these results another attempt to grow a $LaNi_2Bi_2$ film was done. The results for this attempt are shown in figure 7.6a. Only (00l) reflections are observed. The reflections up to the (006) peak show Laue oscillations. From the Nelson-Riley method, a c-axis lattice parameter of 9.77 Å ± 0.01 Å is determined. Although the phase formation was successful and only (00l) reflections are observed, there is an additional impurity reflection at 51.8° which can be identified as nickel as already described before. The temperature behaviour of the resistivity of the film is purely metallic with a room temperature resistivity of 100 $\mu\Omega$ cm and a resistivity of $\sim$ 77 $\mu\Omega$ cm at 2 K. No superconducting transition was observed for this film down to 2 K. Similar to the films before, this film also decomposes very fast after exposure to air. The combination of an additional nickel peak which indicates an excess of nickel and the forbidden odd reflections for the desired $LaNi_2Bi_2$ *I4/mmm* structure suggests a different compound. From the epitaxial nature of film it is not possible to determine the crystal structure from out-of-plane measurements since only (00l) reflections are present. For that, in-plane measurements are necessary. Because of the instability of the films it was not possible to perform these scans at that time. There was a report on a superconducting pnictide containing nickel and bismuth with a superconducting transition at $\sim$ 4.0 K [136]. The compound has a '112'-type stoichiometry (RENiBi$_2$, RE = La, Ce, Nd ...) and a similar crystal structure as the '1111'-type pnictides with a *P4/mmn* space group (for further information on this compound see section 7.2). In this space group all the observed reflections in figure 7.6 can be indexed. So to further optimize the growth parameters the nickel rate was decreased by 50% whereas all the other parameters were kept the same.

The results of this attempt are shown in figure 7.7. The $2\theta - \theta$ measurement shown on the left side (a) is without any impurity reflections. No nickel or NiBi/$NiBi_3$ compound

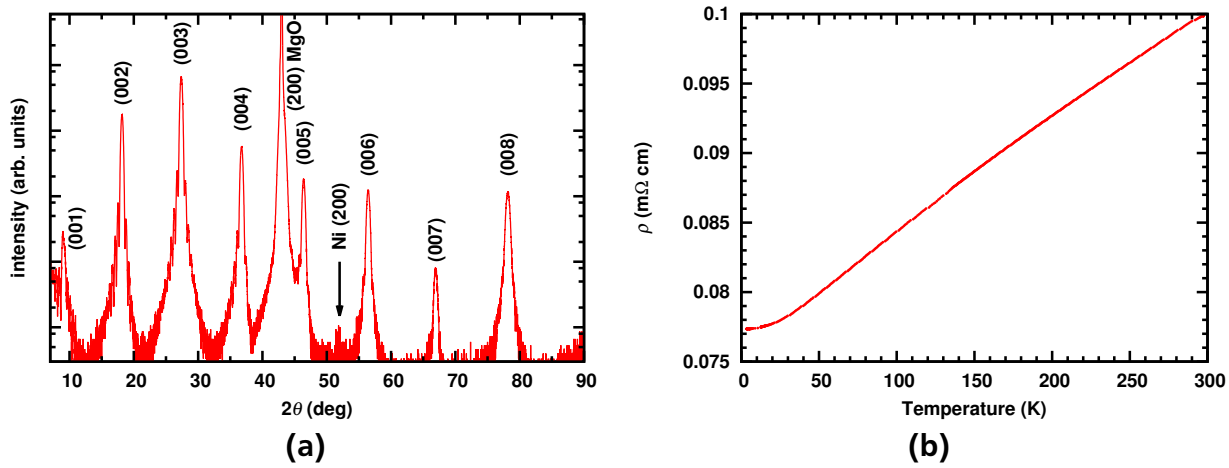

Figure 7.6: a) X-ray measurement of the $LaNi_2Bi_2$ film grown at the optimized parameters. b) resistivity versus temperature measurement.

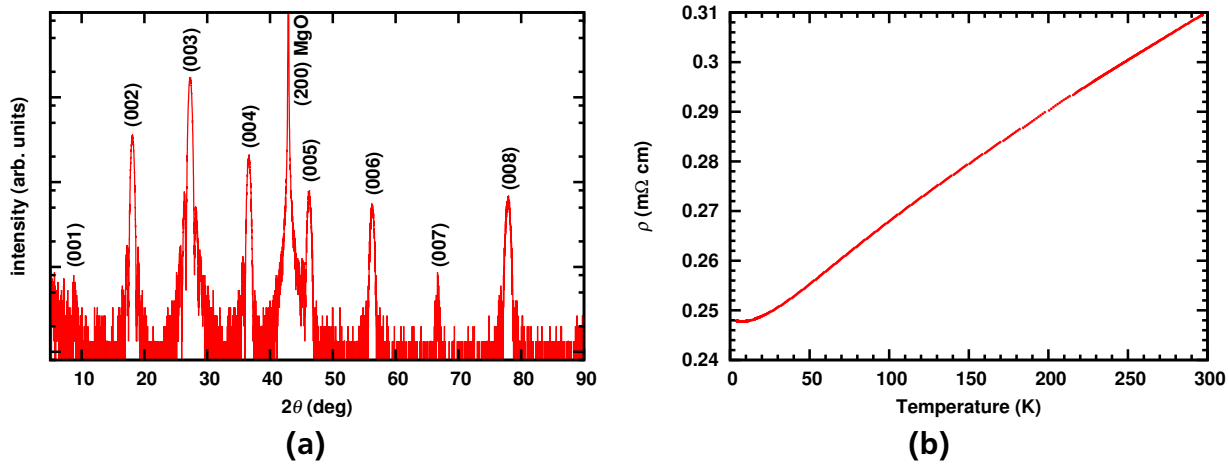

Figure 7.7: a) X-ray measurement of the film grown at decreased nickel rate. b) resistivity versus temperature.

impurities are observed. Only (00l) reflections are present in the X-ray pattern and the reflections from the (002) to the (004) show Laue oscillations. This is the first time, that a pnictide superconductor was grown as a thin film without impurity phases. All films grown so far and reported in literature had impurities of FeAs or similar compounds (see section 3.5. The temperature-resistivity behaviour shown on the right side (b) shows a clean metallic behaviour. The room temperature resistivity is $\sim$ 310 $\mu\Omega$ cm and the resistivity at 2 K is $\sim$ 258 $\mu\Omega$ cm. Still a superconducting transition is not observed. To determine the stoichiometry of the film ICP-OES measurements were done and the composition was determined to be 1:0.94:1.86 for La:Ni:Bi. The results reveal an almost perfect '112' stoichiometry. Nickel as a deficiency of 6% and for bismuth a deficiency of 14% is determined. Since bismuth and nickel deficiency leads to different doping conditions (bismuth deficiency leads to electron doping while nickel deficiency leads to hole doping) the grown film is an almost non doped composition. It is known from Mizoguchi *et al.* [136] that doping on the nickel site leads to superconductivity. The group also revealed

a very interesting feature of this compound. The bismuth present in the structure exhibit two different valence states and provide two different charge carriers: one light one and one heavy one. This features make this compound interesting to study. One challenge in characterizing the samples of RENiBi$_2$ is the instability when exposed to air. Mizoguchi *et al*. [136] state that the sample decompose as soon as they get in contact with air. Although the films grown in this thesis also show a similar behaviour of decomposing in air, they are far more stable compared to the bulk samples reported in literature since they stay at least for one to two days. The stability issue will be handled by a short section. The next sections deal with the growth of LaNi$_x$Bi$_2$ and CeNi$_x$Bi$_2$ and the dependence of the superconducting transition temperature to the growth parameters. After that a short section will show some first attempts on substituting the nickel and the bismuth site and will give an outlook on possible future work.

7.2 The '112' compounds – an arsenic free pnictide superconductor with peculiar properties

The results obtained in the last section suggest the film growth of a novel class of pnictide superconductors. So far, there are only a few reports on this new superconducting compound. Shortly before the stoichiometry of the grown films were found during this work, Mizoguchi *et al*. [136] reported on a novel and mostly unknown compound of an arsenic free pnictide superconductor, RENiBi$_2$ with RE = La, Ce, Nd and other rare earths. In contrast to the compounds described in chapter 3, in this structure nickel sits on the iron site. Instead of arsenic, the much heavier bismuth occupies the pnictide site. The '112'-type compound crystallizes in the ZrCuSiAs structure like it is found for the '1111'-type compounds. The crystal structure is shown in figure 7.8. The similarity of the both structures ('1111' and '112') is obvious. Structure relevant parameters for some of the RENiBi$_2$ compounds are shown in table 7.2.

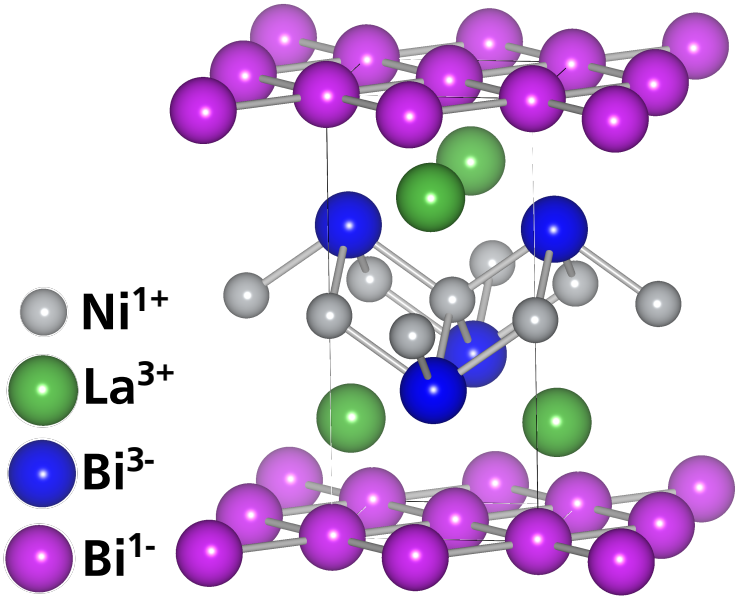

Figure 7.8: Crystal structure of RENiBi$_2$.

Table 7.2: Some parameters of the superconducting $RE\mathrm{NiBi_2}$ compounds.

RE	T_C (K)	H_{C1} (Oe)	a (Å)	c (Å)
La	4.0	90	4.560	9.754
Ce	4.2	65	4.544	9.641
Nd	4.1	55	4.519	9.532
Y	4.1	67	4.483	9.300

But there is one peculiar feature in this structure. While in the '1111'-type compounds two different anions occur (oxygen/fluorine and arsenic) in the '112' compounds only bismuth acts as an anion but in two different valence states. The $\mathrm{Bi}(1)^{3-}$ forms with Ni^{1+} the NiBi counterpart to the FeAs layers in the iron-based superconductors. But the most outstanding feature of these compounds is the existence of a two dimensional $\mathrm{Bi}(2)^{1-}$ square net layer. This layer if formed due to the Coulomb attraction driven relaxation of the Ce^{3+} ions. This relaxation is towards the NiBi(1) layer. As a result a conducting $\mathrm{CeNi}_x\mathrm{Bi}(1)$ layer forms and the aforementioned square-net Bi(2) layer.

It was found in these compounds that there are two different types of electrons, which is a key difference to the "conventional" fluorine doped '1111' pnictide superconductors. The $\mathrm{CeNi}_x\mathrm{Bi}(1)$ layer contain heavy electrons what was observed in conductivity, magnetic susceptibility and heat capacity measurements [136, 137]. These heavy electrons are responsible for the magnetic properties of the compound. In contrast to that the Bi(2) square-net layer contains light electrons which are responsible for the superconducting properties of the compound. In addition, Kodama *et al*. [137] found that the magnetic structure of the Ce^{3+} is antiferromagnetic with a Néel temperature $T_N \approx 5$ K. The antiferromagnetic order coexists with superconductivity which is observed for temperatures below 4 K. That means the magnetic fluctuations are not coupled to the superconductivity in the compound. These properties suggest the possibility of even higher T_C for compounds where antiferromagnetic interactions with much higher T_N could be incorporated.

The peculiar bismuth square net is also found in $\mathrm{SrMnBi_2}$ where anisotropic Dirac fermions and quantum oscillations were observed [138]. The above mentioned antiferromagnetic interaction with much higher T_N due to the Mn^{2+} ions could induce much higher superconducting transition temperatures than reported for the $\mathrm{CeNi_xBi_2}$ compound since the Ni^{1+} is almost nonmagnetic [137, 139]. Of course, an optimal doping must be provided for superconductivity.

Beside the '112' compounds with the iron-pnictide layer there were also reports of bulk superconductivity in intermetallic '112' compounds with same structure such as $\mathrm{HfCuGe_2}$[140]. But T_C was reported to be rather low with a value of 0.6 K. Another superconducting '112' compound reported is $\mathrm{LaNiC_2}$ with a T_C of 2.7 K, but different crystal structure: $Amm2$ instead of the $P4/nmm$ space group [141]. Other $P4/nmm$ compounds containing rare earth elements were studied by Zelinska and Mar [142]. They synthesized zinc deficient $RE\mathrm{Zn_{1-x}Sb_2}$ (RE = La, Ce, Pr, Nd, Sm, Gd, Tb). T_C were not found in these compounds down to 2 K.

7.3 Growth of superconducting "$LaNi_xBi_2$" thin films.[2]

As described in the last section $LaNiBi_2$ films were successfully grown using the molecular beam epitaxy method. The ICP-OES measurements shown at the end of the section revealed an almost perfect '112' stoichiometry. The goal in this section is to optimize the growth parameters and to determine the dependence of the superconducting transition temperature of different growth parameters like growth temperature, nickel rate and bismuth rate. Furthermore the section describes the crystal quality of the grown films and the epitaxial relation between substrate and film.

7.3.1 Influence of growth temperature

In the field of thin film growth, the deposition temperature of the substrate is one of the most important parameters to investigate. In MBE, not only the phase formation of a specific compound depends on the growth temperature, but also the way how a film grow on the substrate can be temperature dependent. E.g. for $YBa_2Cu_3O_{7-\delta}$ thin film growth, the growth temperature determines whether a c-axis or an a-axis oriented growth mode dominates. In the case of MgB_2, the temperature must not be too high because of the volatile magnesium. A similar case was found here in the bismuth containing compounds. If the growth temperature is too high, the phase does not form. Because of that, it is important to study the dependence of growth temperature to determine the window in which it is possible to grow the best quality films. The following paragraphs describes the results on the variation of the deposition temperature. The temperature was varied between 380 °C and 460 °C. The average thickness of the films was $\sim$ 30 nm. The individual growth rates of the elemental sources are 0.2 Å/s for lanthanum, 0.054 Å/s for nickel and 0.55 Å/s for bismuth. One may wonder about the reduction of the lanthanum and the nickel rate. The reduction of the rates was done due to a better stability of the sources. In addition, the idea was to grow nickel deficient films so that the nickel rate was decreased a bit more.

On a first view, it is obvious that the upper and lower limit of the growth temperature where a phase formation is not possible is rather sharp (figure 7.9). The lower limit for the substrate temperature is 390 °C. Only ten degree lower at 380 °C no phase reflections can be observed in the $2\theta - \theta$ measurement (figure 7.9a). The same applies for the upper temperature limit. Already at 460 °C a phase formation is not observed and no reflections are visible in the X-ray measurement. But one has to notice that the top layers of the grown film seem to be fine as suggested by the RHEED image taken directly after deposition (inset of figure 7.9f). The RHEED image clearly shows streaks which is an indication for a smooth and epitaxial growth of the film. The upper limit where a growth of the films is still possible is at 450 °C (figure 7.9e). A phase formation still can be observed although the reflections are already lower in X-ray intensity compared to the measurements performed for the films grown between 410 °C and 430 °C. In that small temperature window the best results were obtained. A possible reason for the observed lack of a phase formation in the X-ray scan at higher growth temperatures could be a massive loss of bismuth. Because of the low sticking coefficient of bismuth the structure is deficient in bismuth at higher growth temperature. This leads to defects which cause a fast decomposition of the films when exposed to ambient

[2] The results shown here are published in [143]

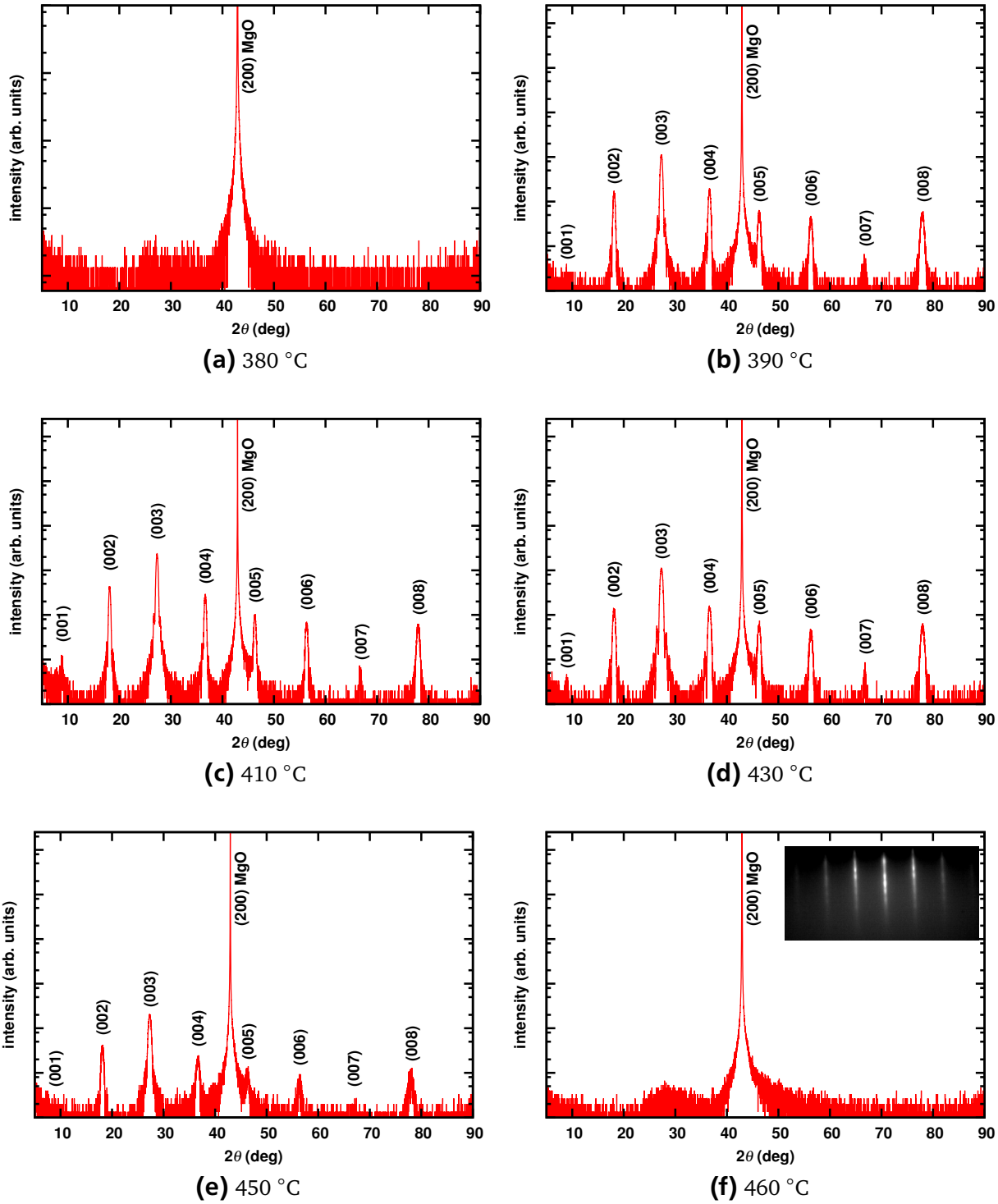

(a) 380 °C **(b)** 390 °C

(c) 410 °C **(d)** 430 °C

(e) 450 °C **(f)** 460 °C

Figure 7.9: X-ray measurements of $LaNi_xBi_2$ films grown at various temperatures.

atmosphere. This would explain the RHEED streaks observed after growth, but no X-ray peaks. The heavy bismuth loss leads to a unstable system. In the temperature range of 410 °C to 430 °C the bismuth loss can be compensated and the structure is much more stable, although these films also decompose after some time when exposed to air.

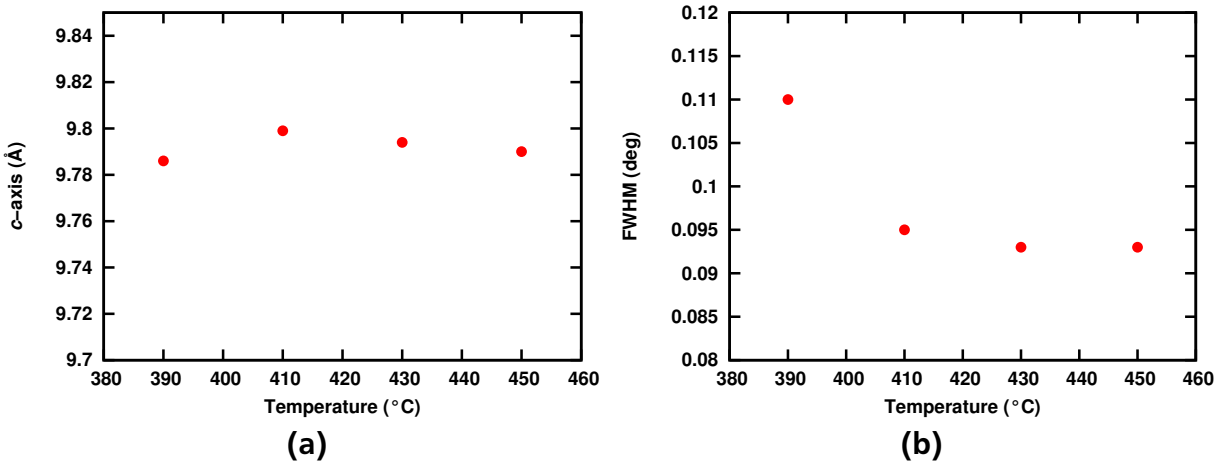

Figure 7.10: a) Variation of c-axis lattice parameter versus growth temperature of and b) FWHM of the $2\theta - \theta$ measurement versus growth temperature of $LaNi_xBi_2$ films grown with rates of 0.2 Å/s for lanthanum, 0.054 Å/s for nickel and 0.55 Å/s for bismuth.

The c-axis lattice parameter determined by the Nelson-Riley method varies between 9.786 Å and 9.799 Å (figure 7.10a). That means there is not much variation in the lattice parameter connected to a change in growth temperature. Figure 7.9b shows the FWHM of the (003) reflection from the $2\theta - \theta$ measurement versus the growth temperature. It can be seen that the film grown at 390 °C exhibit the highest FWHM at a value of 0.11°. With higher temperature the FWHM decreases down to a value of 0.093°. Between 430 °C and 450 °C the FWHM stays constant. As already stated before the FWHM of the $2\theta - \theta$ measurement is not a real measure for the film crystallinity but gives a good impression of the film quality.

The before described temperature dependence is valid for *in situ* growth of the $LaNi_xBi_2$ phase. However, it is possible to grow the film at much lower temperatures and then anneal it at the usual growth temperature of 430 °C. The results for this experiments are shown in figure 7.11. The figure shows a RHEED image which is taken directly after the growth process. The growth temperature was as high as 230 °C. As it can be seen in the image, the films seem to be polycrystalline in nature. The RHEED image is dark with no clean features. After this image was taken the substrate temperature was raised to the usual growth temperature of 430 °C and held there for ten minutes. The results of this annealing process in vacuum are shown in the right RHEED image of figure 7.11. The rings disappeared and instead a streaky RHEED image can bee seen now indicating a smoothing of the surface and a formation of single crystal thin films. The X-ray measurement performed after the annealing process confirmed the formation of the $LaNi_xBi_2$ phase. The diffraction pattern shown in the bottom image of figure 7.11 exhibit only (00l) reflections. The c-axis lattice parameter is determined to be 9.807Åand thus is in the range of the the c-axis

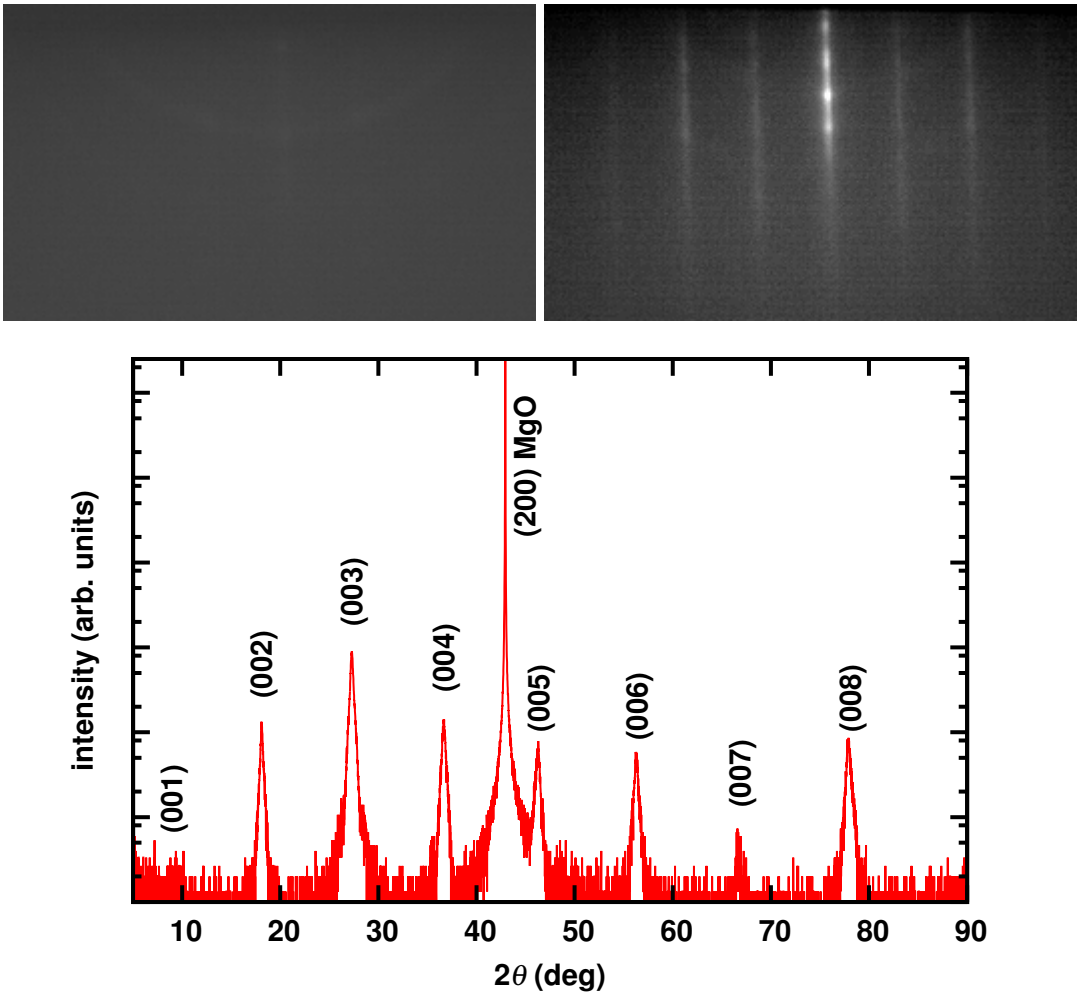

Figure 7.11: Top: RHEED images of the film grown at 230 °C after deposition (left) and after ten minutes of annealing at 430 °C (right). Bottom: $2\theta - \theta$ measurement of the annealed film.

lattice parameter determined for the $LaNi_xBi_2$ films grown for the temperature scan. Laue oscillations can not be observed and the $2\theta - \theta$ FWHM of the (003) reflection is with 0.37° significantly larger than the FWHM of the films grown directly in the temperature range of 430 °C. One explanation for this is a polycrystalline phase formation of the $LaNi_xBi_2$ phase at lower temperatures. With the annealing procedure singe crystals start to grow and the films surface also smoothens.

To summarize, it can be said that a phase formation could only be achieved in a small window of 60 °C in the range of 390 °C and 450 °C. Substrate temperatures above or below do not lead to either an *in situ* phase formation or to an unstable phase. The optimal growth temperature is between 410 °C and 430 °C. However, it is possible to grow single crystal films at lower temperatures like 230 °C and form the phase "*ex situ*" through an annealing step at the optimal growth temperature of 430 °C after the actual growth procedure.

7.3.2 Influence of the bismuth rate

One of the most crucial factors for the growth of the $LaNi_xBi_2$ films is the bismuth rate used during deposition. As often seen before, the control of the bismuth content of the film is challenging because of its high volatileness. It is already known from section 7.1 that higher bismuth rates lead to a formation of the $LaNi_xBi_2$ phase with poor crystal quality and unstable phase but also can lead to the formation of $NiBi_3$ impurity phase. For that reason the bismuth rate was decreased and varied in a rather small window. The results described in the last section suggest an optimal growth temperature of 430 °C to grow the $LaNi_xBi_2$ phase on MgO single crystal substrates and for nickel and lanthanum rates of 0.054 Å/s and 0.2 Å/s, respectively. The typical film thickness was $\sim$ 30 nm. As a measure for the film quality again the $2\theta - \theta$ measurements and the temperature behaviour of the resistivity were taken. Figure 7.12 shows the results of the measurements. It can be seen that all the chosen bismuth rates 0.55 Å/s, 0.515 Å/s and 0.49 Å/s lead to a phase formation of the desired $LaNi_xBi_2$ phase. In the $2\theta - \theta$ measurements, only the $(00l)$ reflections can be observed. The highest X-ray intensity is determined for the film grown at 0.49 Å/s (figure 7.13a). With increasing bismuth rate the intensity decreases. The c-axis lattice parameter for the three films is almost identical and varies only in the third digit. It is determined to be between 9.798 Å and 9.801 Å. With a tolerance of 0.005 Å it can be said that the lattice parameter is the same for the bismuth rates and thus is independent of the bismuth content in the structure.

A real difference can be seen in the ρ-T measurements (figure 7.12b, d and f). With a room temperature resistivity of 750 $\mu\Omega$ cm the film grown at 0.55 Å/s bismuth rate is more than three times as high as the room temperature resistivity of the other two films, which are close to each other at 190 $\mu\Omega$ cm for 0.515 Å/s and 210 $\mu\Omega$ cm for 0.49 Å/s (figure 7.13b). The last mentioned films exhibit a metallic behaviour with an almost linear decrease in resistivity with temperature. The film grown at 0.55 Å/s has an almost constant resistivity with decreasing temperature. At low temperatures around 50 K the resistivity starts to increase slightly. For all of the grown films the ratio of room temperature resistivity and the resistivity at 10 K $\rho_{300\ \mathrm{K}}/\rho_{10\ \mathrm{K}}$ was determined. The ratio is in all cases close to one which indicates a poor metallic behaviour. All the films show an onset of a superconducting transition, but no T_C zero down to 1.8 K. This indicates a wrong doping and structural reasons for the superconducting compound. Nevertheless the superconducting onset temperature can be determined. The lowest T_C onset with a temperature of 3.5 K is determined for the film grown at 0.55 Å/s.The films grown at 0.515 Å/s and 0.49 Å/s exhibit a T_C onset of 3.9 K and 4.1 K respectively. Figure 7.13d visualizes the trend of the T_C onset with bismuth rate. The trend of lower bismuth rates giving a higher T_C onset indicates an excess bismuth content inside the structure. Since a T_C zero could not be obtained, the T_C onset is the measure of choice to determine the best parameters for the film growth of the $LaNi_xBi_2$ phase. Because of that a bismuth rate of 0.49 Å/s is most promising in the process of the optimization for thin film deposition of superconducting $LaNi_xBi_2$.

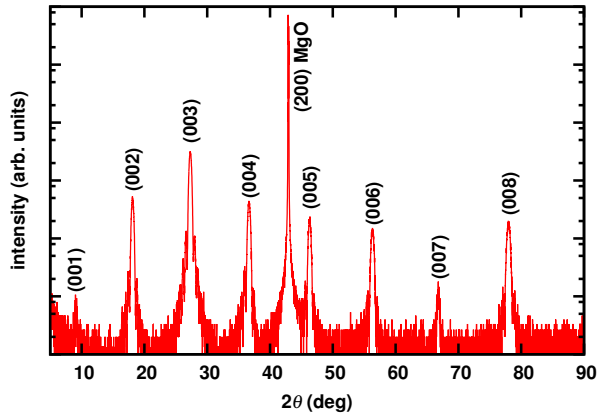

(a) $2\theta - \theta$ (0.490 Å/s)

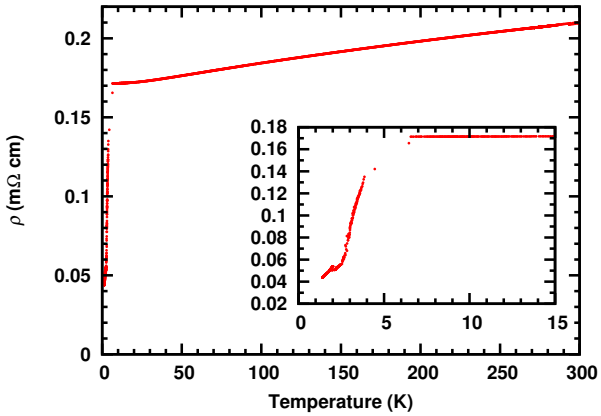

(b) Resistivity vs. Temperature (0.490 Å/s)

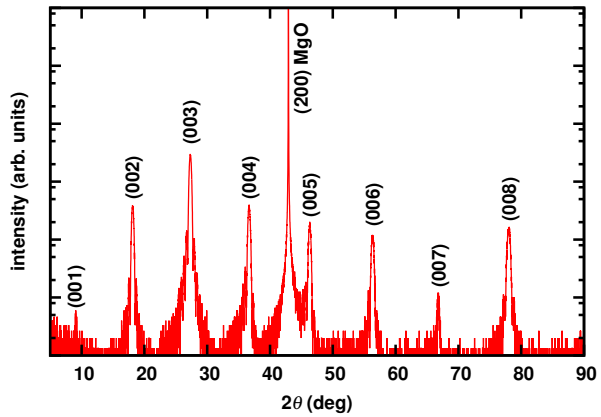

(c) $2\theta - \theta$ (0.515 Å/s)

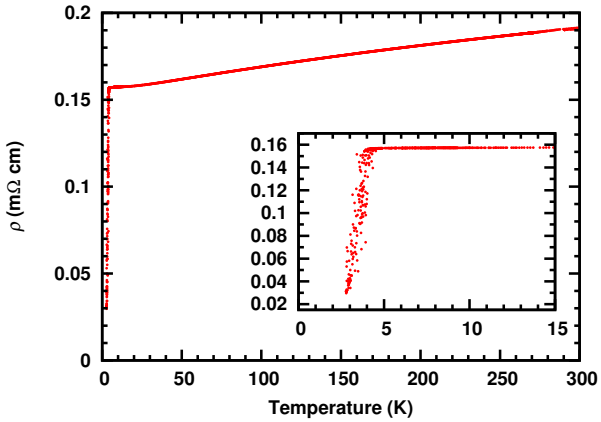

(d) Resistivity vs. Temperature (0.515 Å/s)

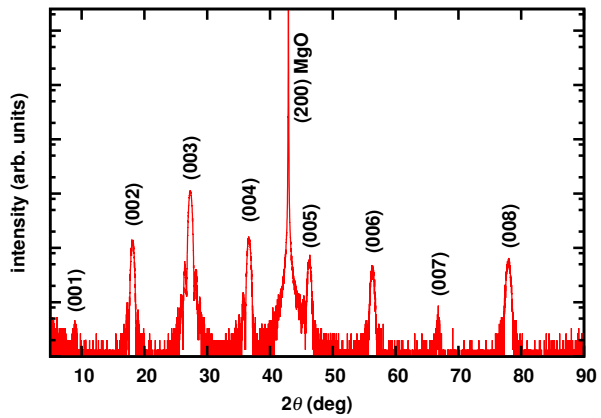

(e) $2\theta - \theta$ (0.550 Å/s)

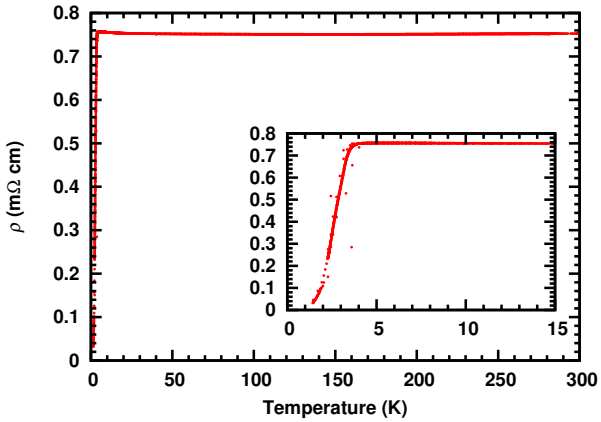

(f) Resistivity vs. Temperature (0.550 Å/s)

Figure 7.12: X-ray measurements and the temperature behaviour of the resistivity of $LaNi_xBi_2$ films grown at various bismuth rates.

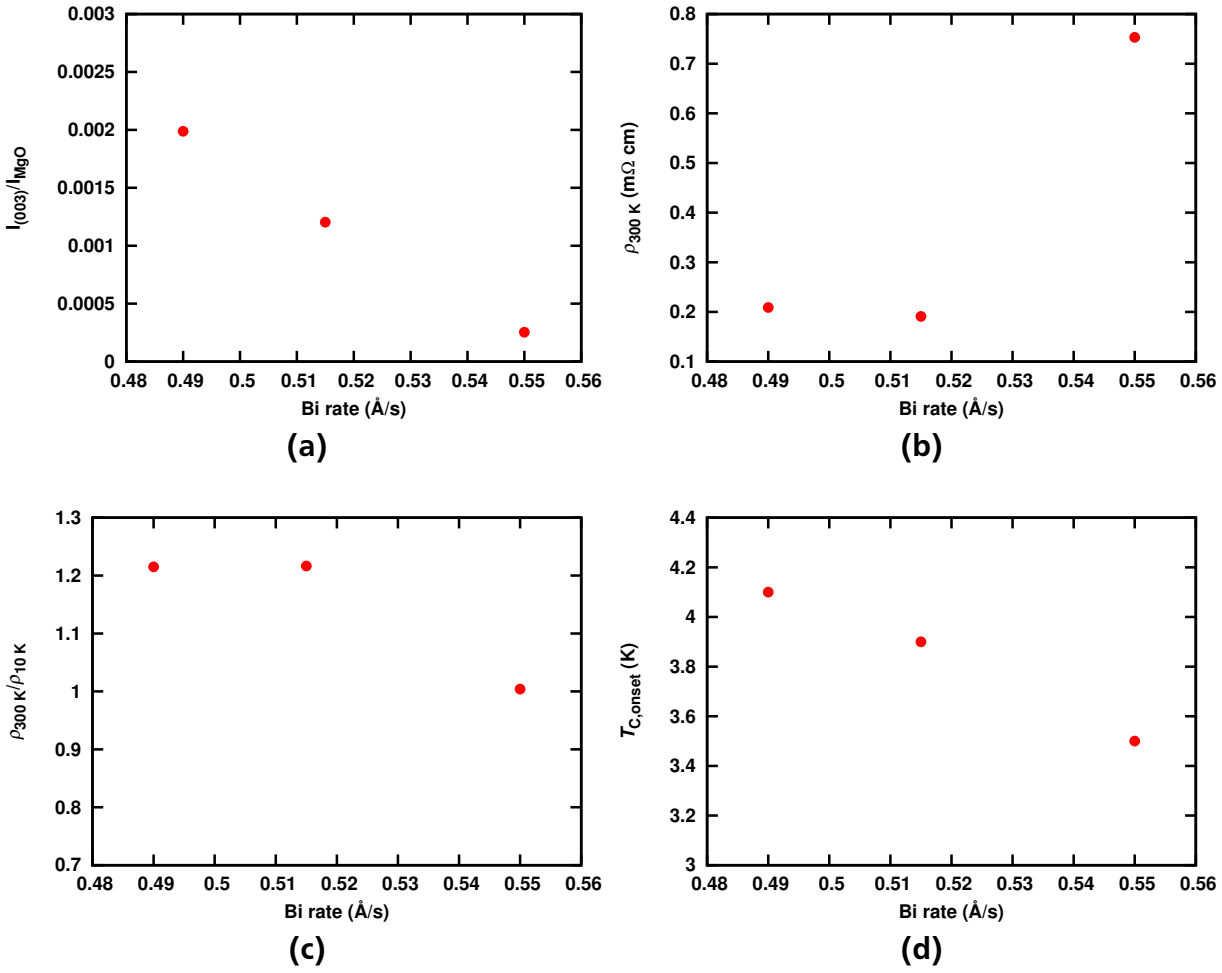

Figure 7.13: a) Intensity ratio of the (003) $LaNi_xBi_2$ reflection and the (002) MgO reflection versus bismuth rate. b) Room temperature resistivity versus bismuth rate. c) Ratio of room temperature resistivity and resistivity at 10 K versus bismuth rate. d) Superconducting transition onset temperature versus bismuth rate of the $LaNi_xBi_2$ films.

7.3.3 Influence of the nickel rate

After the optimization of the growth temperature and the bismuth rate which are crucial parameters for the formation of the $LaNi_xBi_2$ phase, it is necessary to have a deeper look on the influence on the electrical transport properties. Theoretically, it is possible to dope through bismuth deficiencies. Another way of doping in this compound is through nickel deficiencies. Because of the temperature dependence of bismuth inside the structure, doping through nickel deficiencies is a more controllable way of inducing superconductivity in this compound. Beside the temperature dependence of bismuth another reason why the nickel site is more controllable is the structural feature of the $LaNi_xBi_2$ phase. Since the bismuth is present in two different valance states in the structure, it is not sure that a variation in the bismuth rate leads to a doping suitable for superconductivity. Theoretically, bismuth deficiencies can be induced in the Bi^{-1} or in the Bi^{-3} site. The following section deals with the effect of a nickel rate variation on the film growth and the superconducting properties.

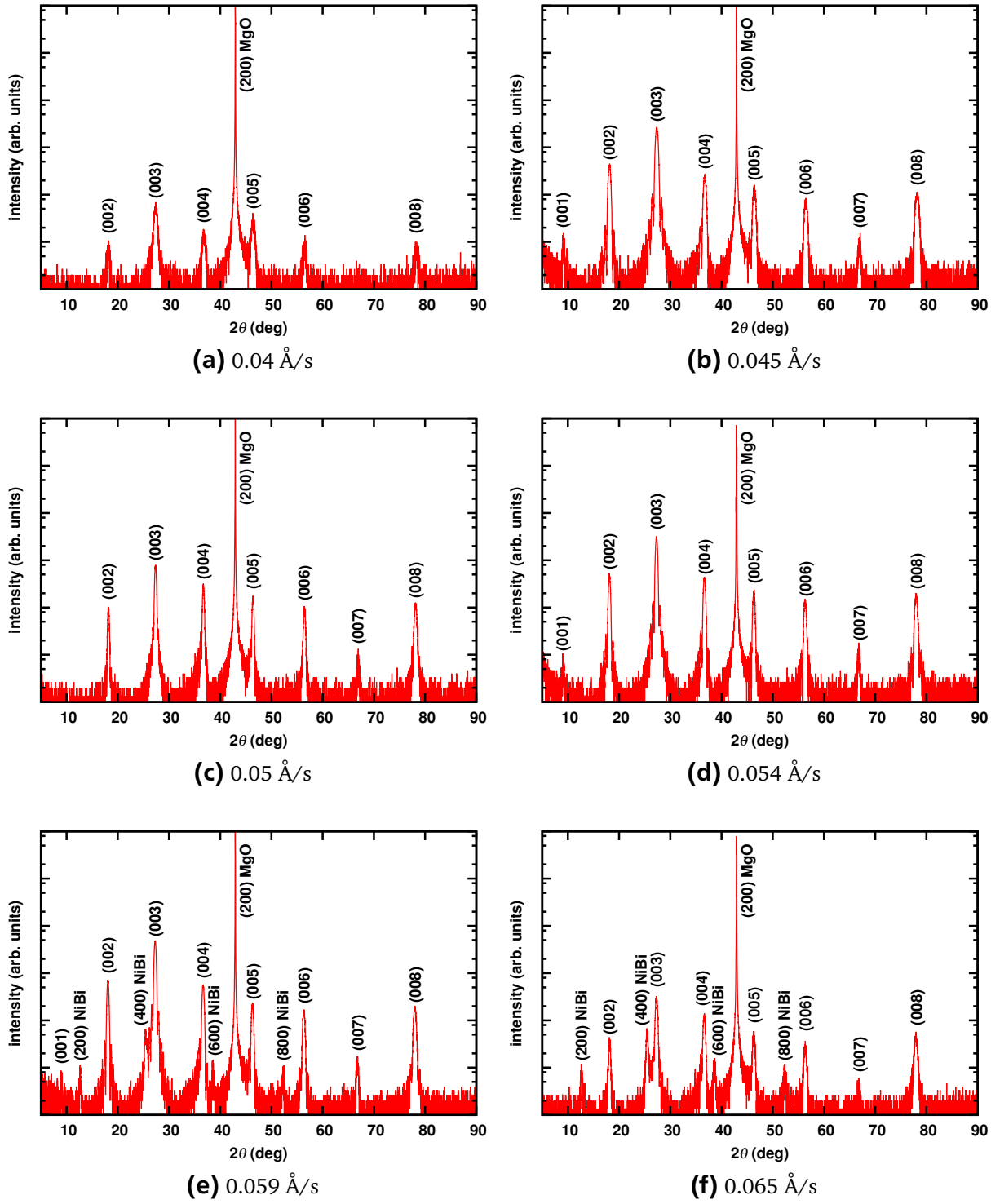

(a) 0.04 Å/s **(b)** 0.045 Å/s

(c) 0.05 Å/s **(d)** 0.054 Å/s

(e) 0.059 Å/s **(f)** 0.065 Å/s

Figure 7.14: $2\theta - \theta$ measurements of $LaNi_xBi_2$ films grown at various nickel rates.

The parameters for the growth temperature and the bismuth rate were set to the optimal values as described in the last sections (0.2 Å/s for the lanthanum rate, 0.49 Å/s for the bismuth rate and 430 °C as growth temperature). The nickel rates were varied in steps of 10% starting from the rate which was used for the bismuth variation (0.054 Å/s). The rates were varied in both directions, down to a minimal rate of 0.04 Å/s and up to a maximum nickel rate of 0.065 Å/s. The typical film thickness again was ∼ 30 nm.

The results of the $2\theta - \theta$ measurements of the grown films are shown in figure 7.14. For all nickel rates a phase formation of $LaNi_xBi_2$ on MgO as a substrate was possible, but the quality varies with the nickel content. Figure 7.14a shows the X-ray measurement of the film grown at the lowest rate of this series of 0.04 Å/s. Although the diffraction pattern is free from impurity reflections and only (00l) peaks are, observable the intensity of the peaks is very weak. The lowest intensity reflections (001) and (007) are not observable in this measurement. The c-axis lattice parameter was determined to be 9.783 Å which is in the same range as the films grown at different bismuth rates. With increasing nickel rate a change in the c-axis lattice parameter can be observed (figure 7.15). For the film grown at 0.045 Å/s nickel rate the c-axis lattice parameter was determined to be 9.769 Å. Further increase in the nickel rate leads to an increasing c-axis lattice parameter. The films grown at 0.05 Å/s and 0.054 Å/s nickel rate exhibit a c-axis lattice parameter of 9.785 Å and 9.802 Å respectively. Going higher in nickel rate, a further increase in the c-axis lattice parameter can not be observed and the c-value is determined to be in the range of 9.8 Å. The shrinking c-axis lattice parameter at lower nickel rates can directly be derived from the crystal structure. The nickel deficiencies occur in the interlayer of the structure and thus lead to a shorter c-axis. Although, for all nickel rates a phase formation can be observed, a second phase appears as evident from the $2\theta - \theta$-scan for the films grown at nickel rates above 0.054 Å/s. In these films grown at nickel rates of 0.059 Å/s and 0.065 Å/s impurity peaks are detected which can be identified as NiBi reflections (figure 7.14e and f). The intensity of the NiBi phase peaks increases with increasing nickel rate. This indicates a stronger formation of this phase. Since the reflection intensity for the $LaNi_xBi_2$ phase decreases it seems to be that at these growth conditions with higher nickel rate the formation of NiBi is more favoured. The NiBi impurity phase seem to grow textured and could be the reason for the constant c-axis lattice parameter at higher nickel rates. The excess nickel now incorporates in the NiBi structure and, thus, can not influence the $LaNi_xBi_2$ compound. However, for all of the films within this series Laue oscillations can be observed. In the films grown with nickel rates in the range of 0.045 Å/s to 0.059 Å/s the Laue oscillations are most prominent and are seen for reflections from (001) to (006) indicating a good coherence between film and substrate.

The main reason for the study by varying the nickel rate was to determine the influence of nickel deficiencies inside the structure on the superconducting properties of $LaNi_xBi_2$. For that the $\rho - T$ curves of each film were measured (figure 7.16). Since the NiBi impurities for the films grown at 0.059 Å/s and 0.065 Å/s are also reported to be superconducting, the temperature-resistivity-curves are not shown here. It can not be distinguished whether the superconducting transition is originated from the NiBi phase or the $LaNi_xBi_2$ phase. Except for the film grown at 0.054 Å/s all the films exhibit a T_C zero.

The film grown at 0.04 Å/s has a relatively high room temperature resistivity of ∼3 mΩ cm and stays almost constant over the whole measurement range from 300 K down to 1.8 K. At 3.78 K the resistivity starts to drop and a superconducting onset is observed. T_C zero is

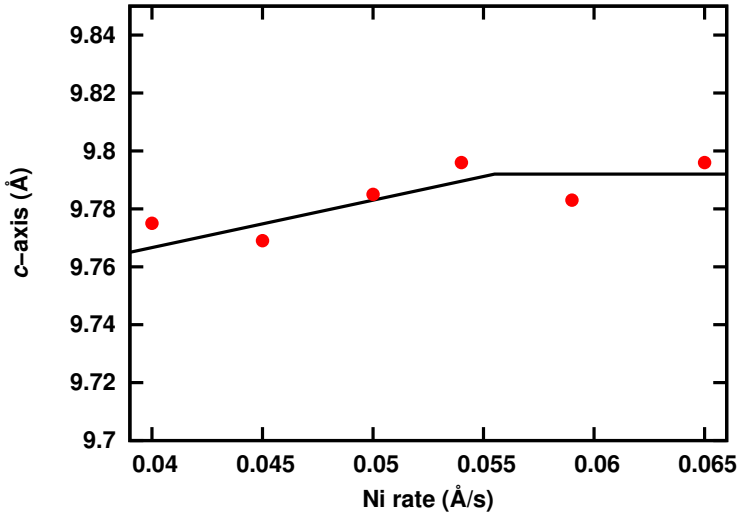

Figure 7.15: Variation of c-axis lattice parameter of the $LaNi_xBi_2$ films grown at various nickel rates.

reached at 3.04 K which leads to a ΔT of 0.59 K. ΔT is the transition width and is defined as the change from 90% to 10% of the resistivity above the transition. The best results are obtained for the film grown at 0.045 Å/s. The room temperature resistivity is much lower compared to the film grown at 0.04 Å/s and has a value of ∼500 $\mu\Omega$ cm. The general behaviour of the resistivity of the $LaNi_xBi_2$ film is metallic and decreases with decreasing temperature. At 3.95 K the resistivity starts to drop and T_C zero is reached at 3.75 K. With a ΔT of 0.15 K, the transition is rather sharp. The measurement for the film grown at 0.05 Å/s shows some peculiar features which could be results of contact issues between the electrical contacts of the measurement stick and the sample. The resistivity increases with decreasing temperature. The room temperature resistivity is with 330 $\mu\Omega$ cm lower than the before mentioned film. Nevertheless, a superconducting transition is observed at 3.5 K and a T_C zero of 2.62 K (ΔT of 0.68 K). The last film grown at a nickel rate of 0.054 Å/s shows a strong metallic behaviour with a room temperature resistivity of 210 $\mu\Omega$ cm. The transition onset is determined to be 3.2 K but a T_C zero is not observed.

To determine the actual nickel content in the structure, EDX measurements of the $LaNi_xBi_2$ films were performed. A visualization of the correlation of T_C onset and T_C zero versus the nickel content is shown in figure 7.17. It can be seen that the best results are received for the film grown at 0.045 Å/s which corresponds to a nickel content of 0.72. This value is slightly larger compared to the x which Mizoguchi *et al.* [136] determined for there optimal doping in $LaNi_xBi_2$ which is at 0.65. But one has to keep in mind, that the bulk samples were reported to be very unstable in air which makes measurements very difficult. In addition, a volume fraction of only 1% was reported for the samples.

While the T_C onset does not change that much with the nickel content on both sides of the optimum at 0.72 the T_C zero shows an influence of the nickel variation. This behaviour is similar to the '1111' compounds [144] and indicates that the nickel deficiencies induce superconductivity in the '112' structure like oxygen deficiencies do in the '1111' compounds. The nickel deficiencies necessary to induce superconductivity in the structure could also

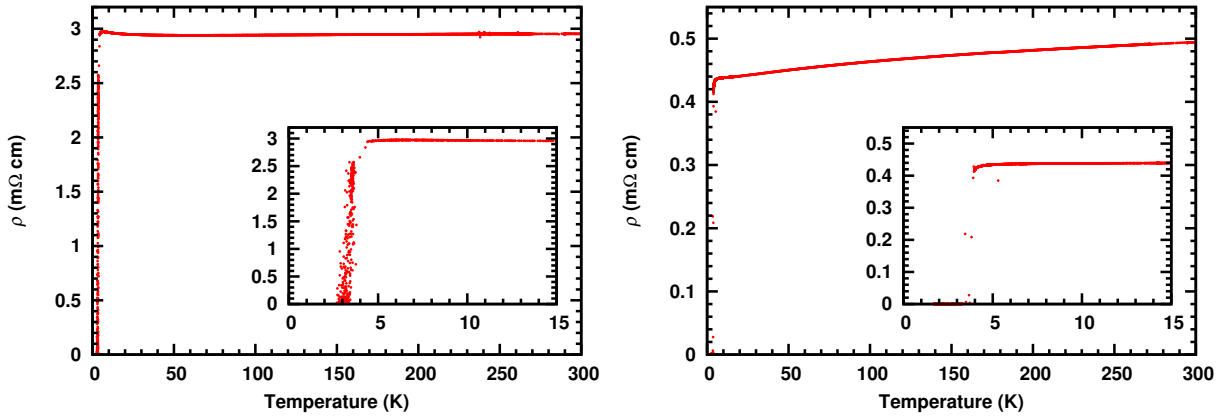

(a) 0.04 Å/s **(b)** 0.045 Å/s

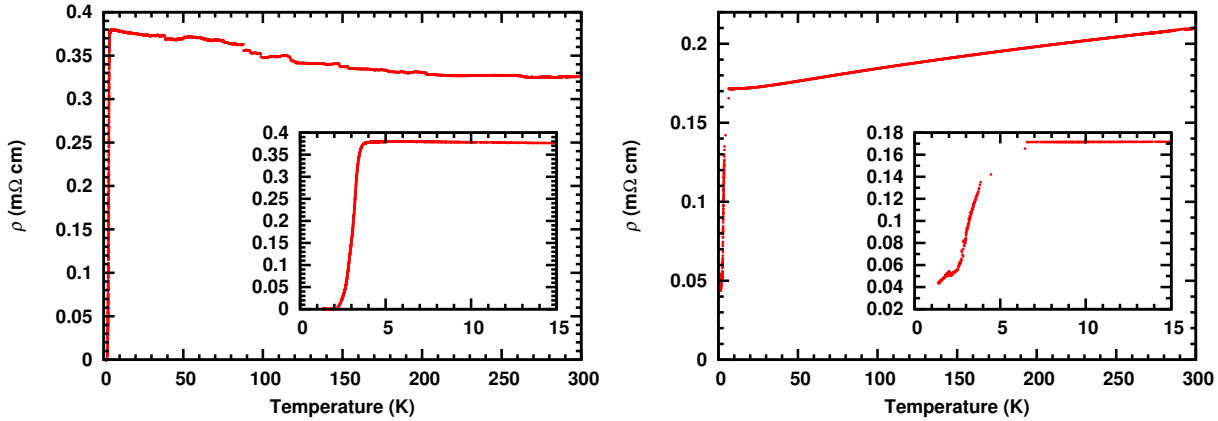

(c) 0.05 Å/s **(d)** 0.054 Å/s

Figure 7.16: $\rho - T$ measurements of $LaNi_xBi_2$ films grown at various nickel rates.

be a reason for the higher resistivity observed for the films with higher T_C. The nickel deficiencies would act as a defect scattering zone for the electrons.

The results obtained here are from films with a thickness of only ∼30 nm. Especially electrical transport properties can vary with film thickness and, thus, based on these results a thicker film with ∼100 nm thickness was grown. The results are shown in figure 7.18.

The X-ray measurement is shown in figure 7.18a. Only (00l) reflections are observed. The c-axis lattice parameter is determined to be 9.770 Å which is in good agreement with the value gained for the thin film grown at the optimum conditions. The inset in figure 7.18a shows a RHEED image of the film taken directly after the deposition. The image shows bright streaks indicating the smooth nature of the film surface and an epitaxial growth. The good crystal quality of the film is shown in the ω scan (figure 7.18b). The low FWHM of only 0.06° indicates a high crystallinity and shows an improvement in the thicker film. As already expected the electrical properties improved for the thicker film. The room temperature resistivity increased slightly to 580 $\mu\Omega$ cm. The thicker $LaNi_xBi_2$ film gave a T_C onset of 4.05 K and a T_C zero of 3.95 K. The superconducting transition is quite narrow with a ΔT of 0.1 K. The inset of figure 7.18c shows an enlarged portion of the superconducting transition and figure 7.18d is the diamagnetic response of the film measured in a superconducting quantum interference device. It confirms the superconducting nature of the $LaNi_xBi_2$ films.

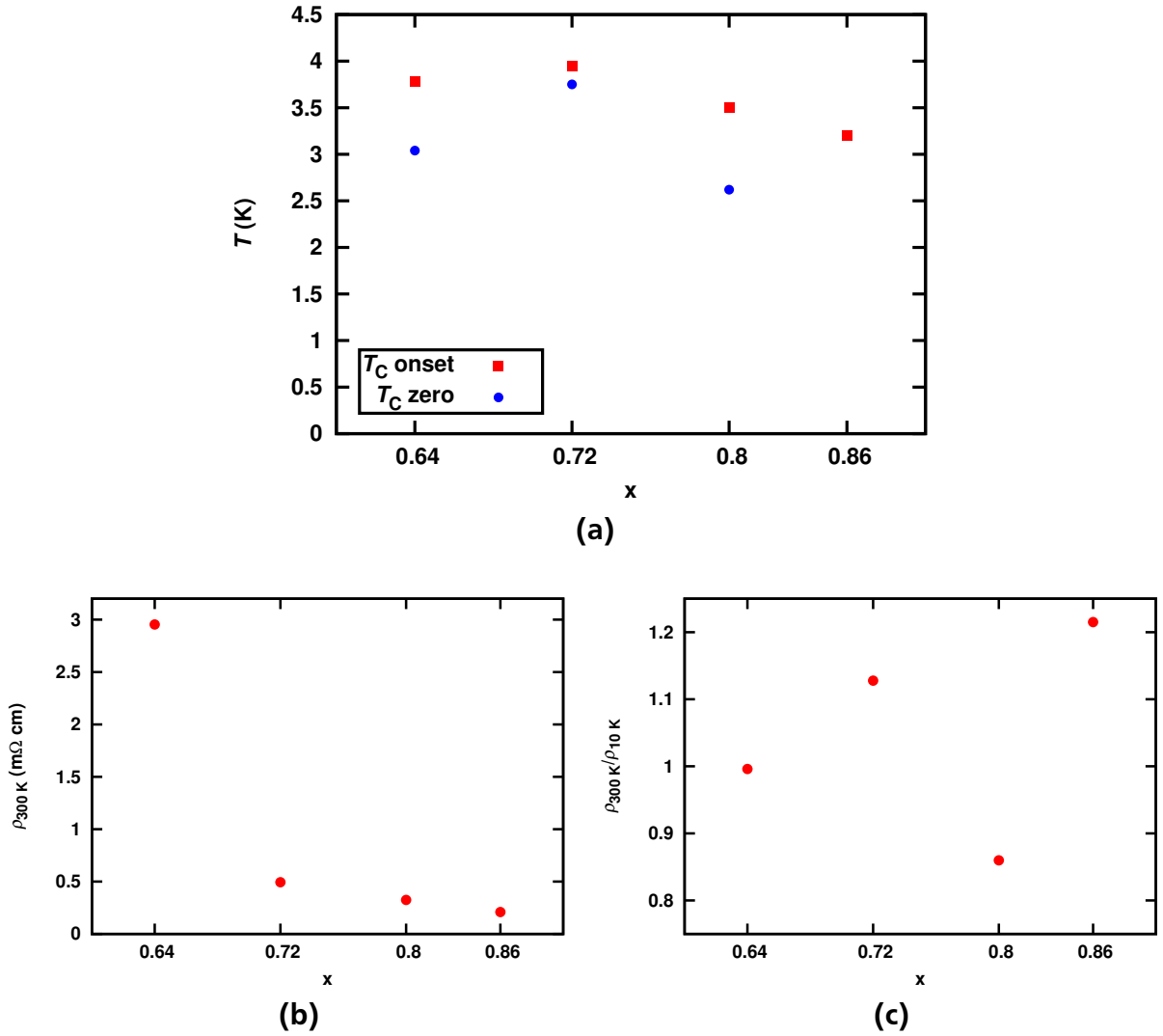

Figure 7.17: a) T_C onset and T_C zero versus x in $LaNi_xBi_2$.b) Variation of room temperature resistivity versus nickel rate. c) Variation of ratio of room temperature resistivity and resistivity at 10 K versus nickel rate.

7.3.4 Epitaxial relation to the substrate

In the last sections it was shown how to grow high quality superconducting $LaNi_xBi_2$ films and the dependence of the crucial deposition parameters (growth temperature, bismuth rate and nickel rate). The films grown at optimum growth conditions show good crystal quality and good physical properties. But the epitaxial relation of the $LaNi_xBi_2$ film to the MgO substrate needs to be clarified.

A first suggestion of the epitaxial relation of the film to the substrate came from the *in situ* RHEED images which were taken during the deposition. Figure 7.19 shows a series of such RHEED images. Figure 7.19a shows the bare MgO surface before the deposition had started along the <100> azimuth. The clean and smooth surface with Kikuchi lines can be seen. Figure 7.19b shows the RHEED image of the film during the deposition roughly 30 s after the phase formation has started (roughly corresponds to ∼15Å). The electron beam azimuth is still <100> along the MgO surface. It can be seen that the streaks corresponding

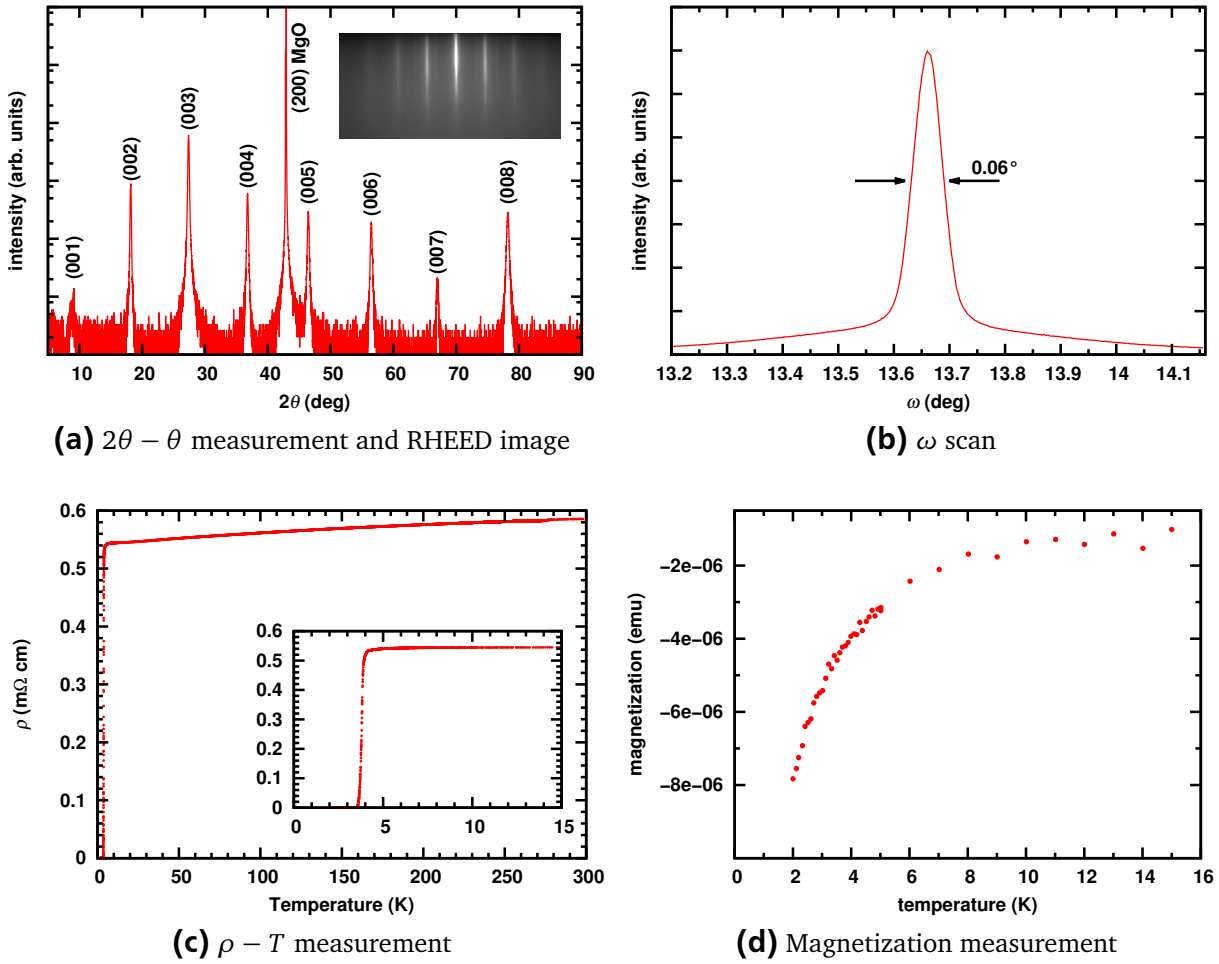

(a) $2\theta - \theta$ measurement and RHEED image **(b)** ω scan

(c) $\rho - T$ measurement **(d)** Magnetization measurement

Figure 7.18: X-ray measurement, RHEED image and ω scan of the ∼100 nm thick $LaNi_xBi_2$ film (top) and $\rho - T$ behaviour and the diamagnetic response measured in a superconducting quantum interference device (bottom)

to the $LaNi_xBi_2$ film appearing in between in that of the MgO substrate. Figure 7.19c shows the RHEED image of the film after deposition. That means the film does not grow directly "cube-on-cube" on the substrate but rotated. Since the film streaks are directly in between in that of the substrate streaks one would suggest a 45° rotated growth of the $LaNi_xBi_2$ phase on top of the MgO. The rotation of the substrate by 45° brings the RHEED pattern with streak spacing close to the one for MgO along <100>. This suggests a 45° rotated growth of $LaNi_xBi_2$ thin films on MgO.

To further confirm the RHEED indicated 45° rotation of the film with respect to the substrate, a ϕ scan of the thicker $LaNi_{0.72}Bi_2$ film (∼100 nm) was carried out. For the film, the (112) plane was chosen since it has the strongest intensity of all the $LaNi_xBi_2$ peaks. For MgO the (111) plane was chosen. The results are shown in figure 7.20, where a) shows the ϕ scan of the $LaNi_{0.72}Bi_2$ film. The four fold symmetry can be clearly seen by the four reflections with a distance to each other of 90°. From the 2θ position of the (112) reflection, the a-axis lattice parameter of $LaNi_xBi_2$ can be determined. For the grown $LaNi_{0.72}Bi_2$ film, an a-axis lattice parameter of 4.57 Å was found. This is in very good agreement with values reported in literature [136]. Figure 7.20b shows the ϕ scan of the

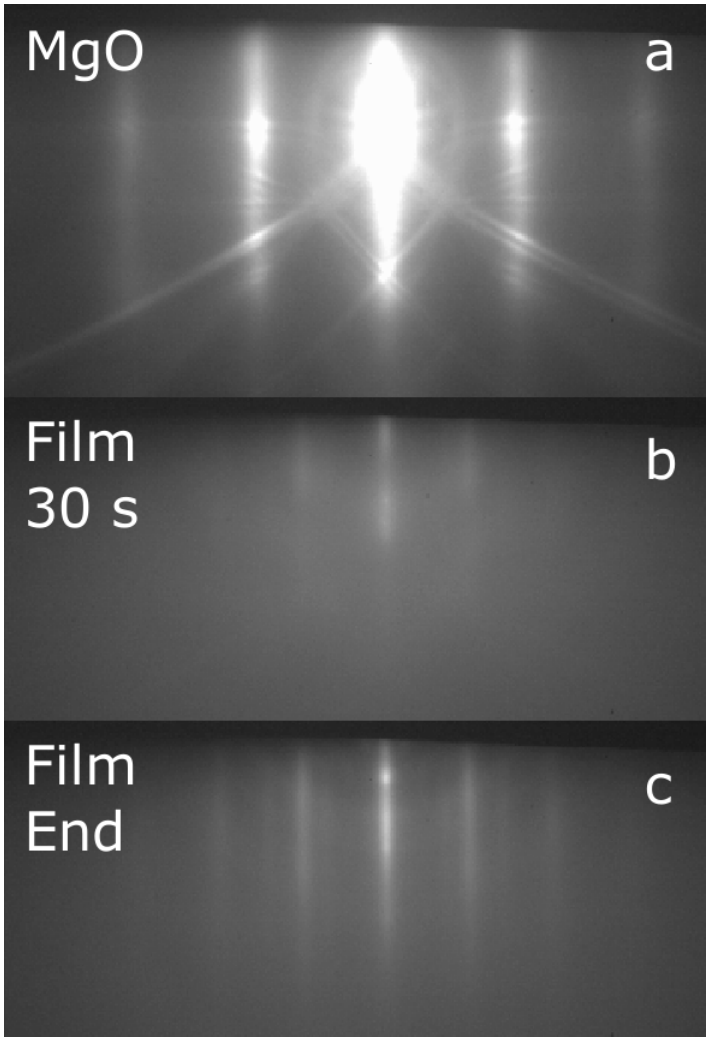

Figure 7.19: Series of RHEED images taken during the deposition of $LaNi_xBi_2$. a) shows the bare MgO substrate before deposition, b) shows the film 30 s after the deposition had started and c) shows the film at the end after the growth process has stopped. The RHEED beam azimuth was along <100> direction of MgO.

MgO substrate. Here also the cubic four fold symmetry can be seen. It is obvious that the film indeed grow 45° rotated with respect to the substrate. However, there are some small reflections in between the film peaks with a distance of 90° from each other, which correspond to the MgO substrate. That means there are some domains which do not grow rotated but grow directly "cube-on-cube" on top of the MgO substrate. From that results the epitaxial relation between substrate and film can be derived as $LaNi_xBi_2$ [100] || MgO [110] and $LaNi_xBi_2$ (001) || MgO (001). A similar behaviour was observed for the growth of Fe-Te-Se epitaxial films on MgO. There the films also grow 45° rotated with respect to the MgO substrate [145]. It is clear that the epitaxial relation can not be driven by the lattice mismatch since this is only 8%. A reason could be the crystal field of the ions at the interface. The large negative ions oxygen and bismuth, favour a reorientation of the atomic arrangement directly at the interface. Figure 7.21 suggests how it could look like on an atomic scale. The figure shows the (001) Bi layer of the $LaNi_xBi_2$ phase (transparent)

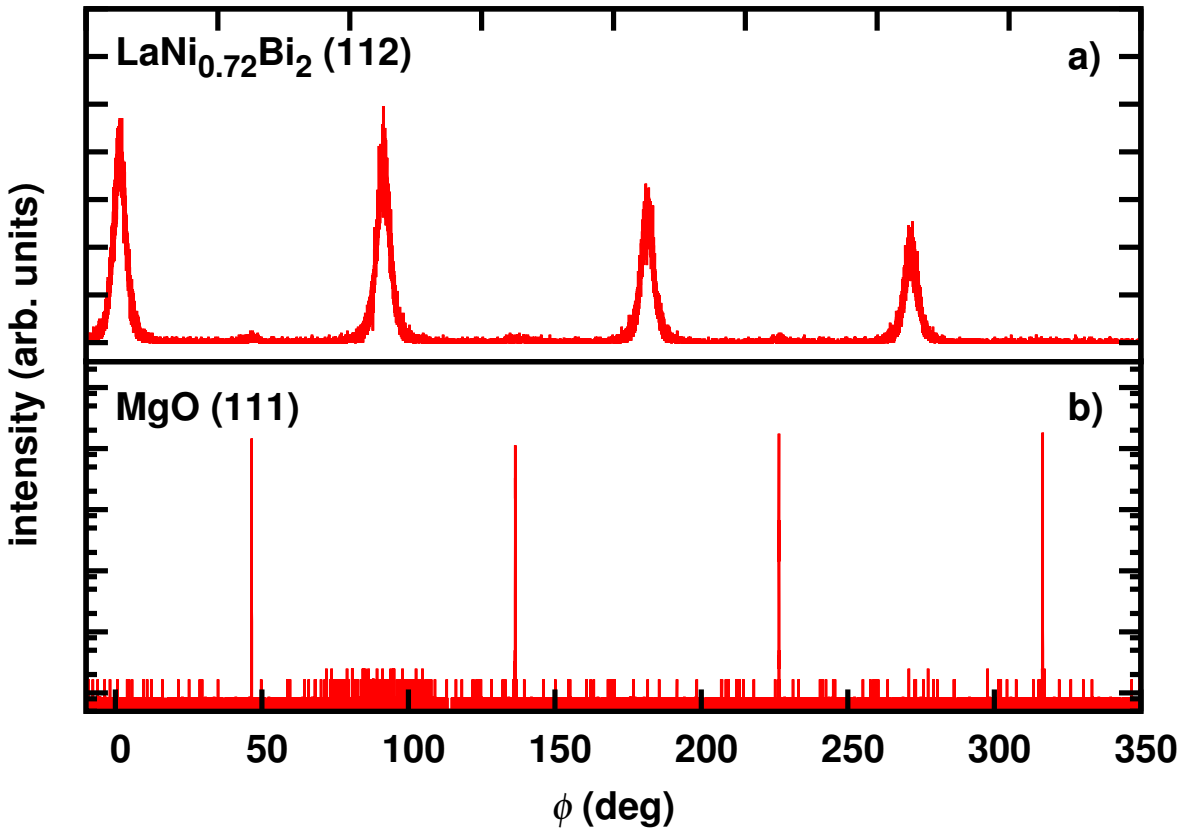

Figure 7.20: a) ϕ-scan of the $LaNi_{0.72}Bi_2$ film and b) of the MgO substrate.

rotated by 45° on top of an MgO (001) layer. With this arrangement the negatively charged bismuth and oxygen almost do not touch each other.

7.3.5 Stability of the films

One issue in analyzing the grown $LaNi_xBi_2$ films was the instability of the phase as soon as the samples were exposed to ambient atmosphere. A similar behaviour was reported for bulk samples of $RENiBi_2$ by Mizoguchi *et al.* [136]. The $LaNi_xBi_2$ films stored in air used to undergo decomposition typically around 2–3 days as evident from the $2\theta - \theta$ scans. After that time no reflections could be observed anymore. This behaviour was observed for samples which were exposed to ambient atmosphere only for the time of characterization. In between the characterization procedures, the samples were stored in vacuum or dried air with a humidity of ∼10–20%. A difference in stability could not be observed for the films stored in dried air or in vacuum. Although the samples decompose in relatively short time, it was possible to perform different characterization techniques even in under ambient conditions. In the report of Mizoguchi *et al.* [136] the characterization had to be done in vacuum or inert atmosphere. Other than that, no characterization was possible since the samples decompose directly after the exposure to air. This means, the high crystal quality obtained in the thin films grown during this work are more stable than the polycrystalline bulk samples which were prepared in a conventional solid state route. It is worthwhile to mention that the films after growth and cooled down to room temperature and remained in

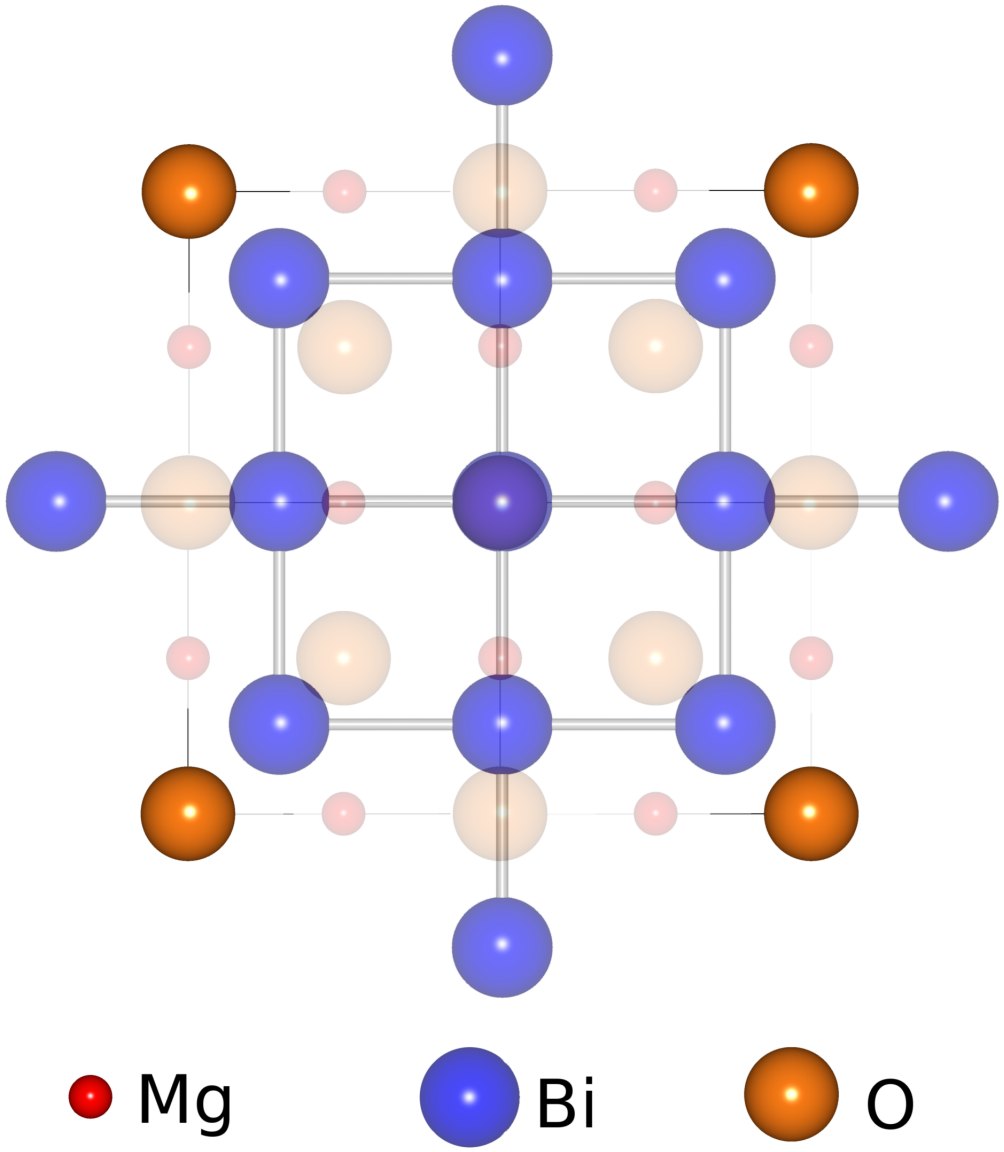

Figure 7.21: $LaNi_xBi_2$ (001) layer on top of an MgO (001) layer.

the growth chamber for over six hours did not show any decomposition as there was no variation in the RHEED pattern of the films. At the same time, the films exposed to the ambient atmosphere for a short time and then reintroduced into the growth chamber did not show any RHEED pattern indicating the decomposition of the surface.

However, there is a huge difference for films exposed to humid air. Figure 7.22 shows two $2\theta - \theta$ measurements of one sample with a thickness of ~90 nm. The $2\theta - \theta$-scan shown in figure 7.22a was done directly after growth. The X-ray diffraction pattern only exhibit $(00l)$ reflections of the $LaNi_xBi_2$ phase and does not show any impurity peaks. The same film was measured again in the same set up after it was stored over night in an air conditioned environment with a humidity of 60%. The measurement performed after this kind of storage is shown in figure 7.22b and it is clear that the films decompose when exposed to humid air. The whole film decomposed in that short time period of around 14 h. Only the (003) reflection could still be observed but much less in intensity. The other reflections which where seen before are not present in the diffraction pattern anymore (they

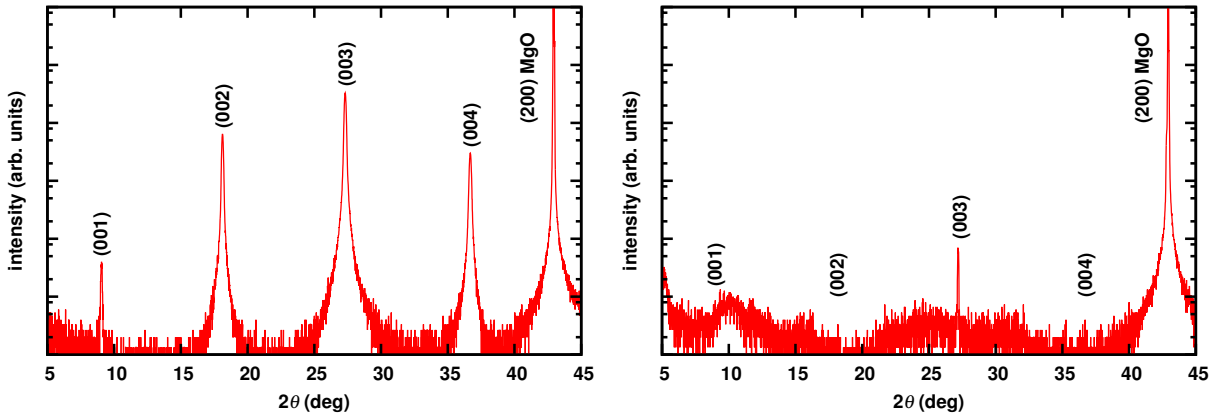

(a) After deposition

(b) After 14 h in ambient atmosphere with a humidity of 60%.

Figure 7.22: $2\theta - \theta$ scan of a $LaNi_xBi_2$ film directly after growth and after 14 h exposed to ambient atmosphere with a humidity of 60%.

are still indicated by the Miller indices to show their actual positions). This result suggests a high dependence of the film's stability to humidity. To perform studies like reciprocal space mapping (RSM) it is necessary to use a vacuum chamber or at least inert gas atmosphere. In the optimal case, the sample does not get exposed to atmosphere after growth at all. During this work a vacuum chamber for that purposes was not present.

7.3.6 X-ray reflectivity measurement of $LaNi_xBi_2$

Since the epitaxial relation and other crystal information is known about the $LaNi_xBi_2$ films it is also interesting to gain information about the layer set up of the film itself. The asymmetry of the Laue oscillations observed in the $2\theta - \theta$-scans indicate a density gradient perpendicular to the substrate plane. To confirm that, an X-ray reflectivity measurement of the film grown at optimal parameters was carried out. The results can be seen in figure 7.23. The fit was done with the software GXRR3 of the Rigaku Corporation. The XRR results show oscillations up to an angle of 3°. The total reflection angle is determined to be ∼0.1°. The model for the fit is shown in table 7.3 and in the inset of figure 7.23. It can be seen that the film seem to consist of a multilayer structure. The bottom layer between substrate and $LaNi_xBi_2$ film is a ca. 3 nm thick Ni layer. On top of the film there seems so be a Bi layer, again with a thickness of ca. 3 nm. The $LaNi_xBi_2$ layer is in between these two layers and has a thickness of roughly 22 nm.

The fit for the $LaNi_xBi_2$ layer was done with a linear variation of density over the layer thickness. While the density of the film at substrate surface was determined to be 10.21 g/cm^3, the density decreases to a value of 7.49 g/cm^3. This density variation was already suggested by the asymmetry of the Laue oscillations of the $2\theta - \theta$-scan. The theoretical density of $LaNi_xBi_2$ is 9.75 g/cm^3. That means, that the density at the bottom of the layer is ∼4 % higher than the theoretical density. Reason for that could be the mismatch in lattice parameters of MgO (or Ni) and the $LaNi_xBi_2$. The lattice parameter of $LaNi_xBi_2$ has to shrink to fit and thus increases the density. The density on top of the layer is almost

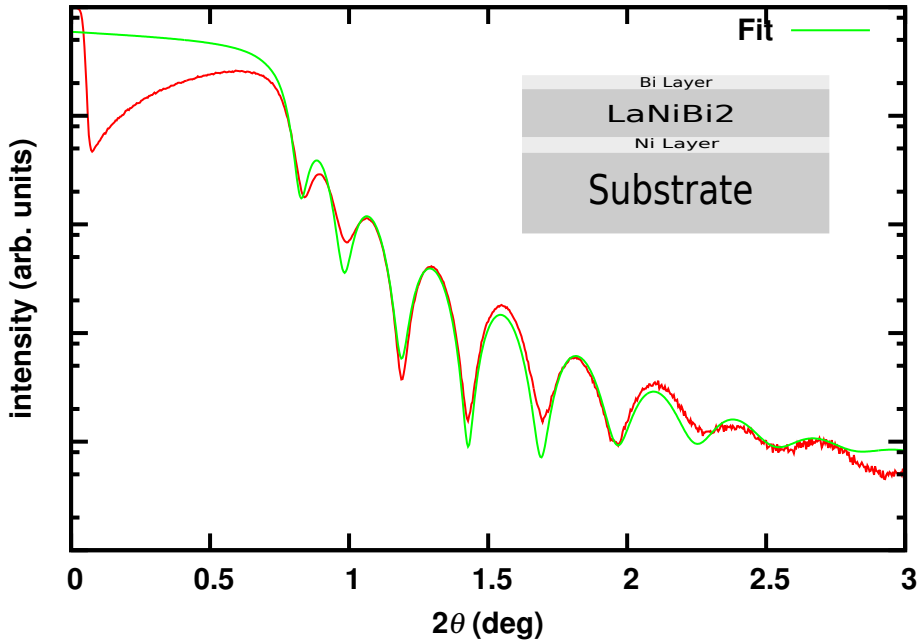

Figure 7.23: X-ray reflectivity measurement and the results of a fit of the $LaNi_xBi_2$ film grown at optimum parameters. The inset shows the model of the layer set up for the fit.

Table 7.3: Fitting results for the X-ray reflectivity measurement of the $LaNi_xBi_2$ film.

Layer	Thickness (nm)	Density ($\frac{g}{cm^3}$)	Roughness (nm)
3 (Bi)	3.164	7.738	1.261
2 ($LaNi_xBi_2$)	22.83	10.21/7.49	1.774
1 (Ni)	3.2	8.88	1.307
Sub (MgO)	—	3.585	0.376

25 % below the calculated value of 9.75 g/cm^3. Here a loss in bismuth could be a reason for the low density of the $LaNi_xBi_2$ layer. For the theoretical density the unit cell mass was calculated considering the nickel deficiency and divided by the unit cell volume determined from the lattice parameters.

The reason for this density variation over the film thickness is not clear at this point. One possible reason could be a decomposition of the film starting from the surface and going through the whole film to the substrate. Experiments performed on $CeNi_xBi_2$ films indicate a start of the decomposition directly after the film is exposed to air (see section 7.4.4). Another possible reason could be a stoichiometry variation along the c-direction which could be a result of unstable sources or even a temperature gradient during the run. To clarify this further experiments have to be done.

7.4 Growth of superconducting "$CeNi_xBi_2$" thin films.[4]

One of the big advantages of the molecular beam technique in comparison with conventional bulk synthesis is the relative easy possibility of substitution. As soon as the growth parameters for a specific compound are established it is relatively easy to exchange one element by another. Since Mizoguchi *et al.* [136] reported the best superconducting properties for the '112'-type pnictides in $CeNi_xBi_2$ and the growth parameters for $LaNi_xBi_2$ were established the lanthanum was substituted by cerium. The deposition conditions were optimized to grow high quality thin films of $CeNi_xBi_2$. The following section deals with the optimization process to find the parameters for the growth of $CeNi_xBi_2$ and the influence of the bismuth and nickel rate on the crystal and electrical properties of the film.

7.4.1 Substitution of lanthanum by cerium and the influence of the bismuth rate

The obvious starting point for a substitution is to take the already established parameters for a compound. The parameters for the first attempt were 0.2 Å/s for cerium, 0.054 Å/s for nickel, 0.55 Å/s for bismuth and 430 °C as growth temperature. The goal was to get as close as possible to a stoichiometric $CeNi_xBi_2$ phase with $x = 1$. For that reason the nickel rate as well as the bismuth rate were increased compared to the optimal parameters for the superconducting $LaNi_xBi_2$ films. The idea is the chemical similarity of the rare earth elements. So a change from lanthanum to cerium should not change the growth conditions that much and parameter's optimization for the cerium rate is not an issue. Crucial for the growth of high quality thin film superconductors is the correct stoichiometry of the films [147].

Figure 7.24 shows the $2\theta - \theta$ measurements of the first attempts to grow $CeNi_xBi_2$ films. In the first deposition run shown in figure 7.24a the starting parameters mentioned above were set. A phase formation could not be observed at all. Neither the RHEED image (not shown here) nor the X-ray measurement shows any formation of the desired phase. Only at 27.7° and at 32.4° two weak peaks could be identified. The peak at 27.7° could belong to the '112' phase but without any other hint, this is too speculative. The second peak observed at 32.4° can not be identified. The next step in growing the $CeNi_xBi_2$ phase was to increase the bismuth rate from 0.55 Å/s to 0.8 Å/s and set the growth temperature to a value of 560 °C. To overcome the bismuth loss because of the higher substrate temperature the bismuth rate was also increased. The results of the X-ray measurement is shown in figure 7.24b and the inset is a RHEED pattern taken after deposition. The RHEED image shows rings indicating a polycrystalline phase formation. The bright spots suggest the presence of a single crystalline phase growing in an island growth mode. In the $2\theta - \theta$-scan a phase formation of the desired $CeNi_xBi_2$ phase is not observed. But at 32.4° the unknown phase appeared again, this time stronger in intensity. The island growing phase seen in the RHEED pattern probably has its origin here. The origin of this reflection could not be clarified and was not of interest in this work.

As already mentioned earlier, a higher growth temperature could result in Bi poor films. For that reason the temperature was decreased to a value of 520 °C while the bismuth rate was increased by 10% to a value of 0.88 Å/s. The RHEED image did not show an

[4] The results shown here are published in [146]

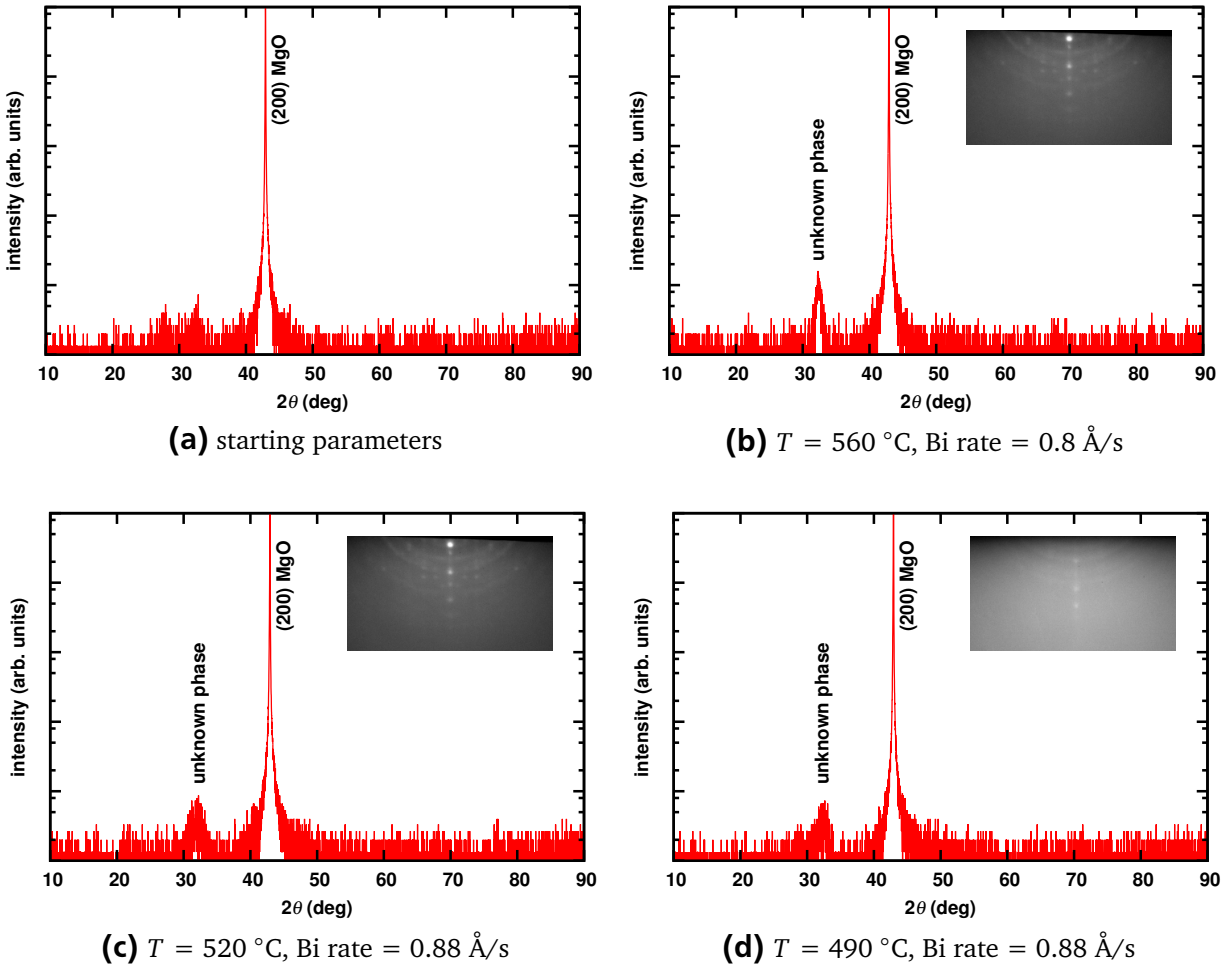

(a) starting parameters

(b) T = 560 °C, Bi rate = 0.8 Å/s

(c) T = 520 °C, Bi rate = 0.88 Å/s

(d) T = 490 °C, Bi rate = 0.88 Å/s

Figure 7.24: X-ray measurements and RHEED images of $CeNi_xBi_2$ films grown at various bismuth rates and temperatures.

improvement in phase formation (inset of figure 7.24c) and the results of the X-ray scan is shown in figure 7.24c. There is still no phase formation of the desired $CeNi_xBi_2$ compound. However, the peak of the unknown phase is weaker in intensity. The reason for that could be the decreased deposition temperature. A higher temperature seems to favour the formation of the unknown phase. Since this is not the desired $CeNi_xBi_2$ phase, the growth temperature is again decreased to 490 °C while the bismuth rate stays the same at 0.88 Å/s. This procedure lead to a further suppression of the unknown phase (see figure 7.24d), although no hint for a formation of $CeNi_xBi_2$ is there. One has to notice that the bismuth rate now has reached almost twice the rate which was necessary for the growth of $LaNi_xBi_2$.

Because of the promising results of the higher bismuth rate it was increased further to a value of 0.968 Å/s and the temperature was decreased to the initial value of 430 °C. Nickel and cerium rates were kept the same. The results of the X-ray measurements are shown in figure 7.25a. It can bee seen, that a $CeNi_xBi_2$ phase has formed with a highly textured growth. Only (00l) reflections are present and the (002) to (004) reflections exhibit Laue oscillations. The pattern looks very similar to the one obtained for the $LaNi_xBi_2$ films. The Laue oscillations are asymmetric which indicates a composition gradient through the film in c-direction. The film thickness is determined to be ∼32 nm and the c-axis lattice parameter

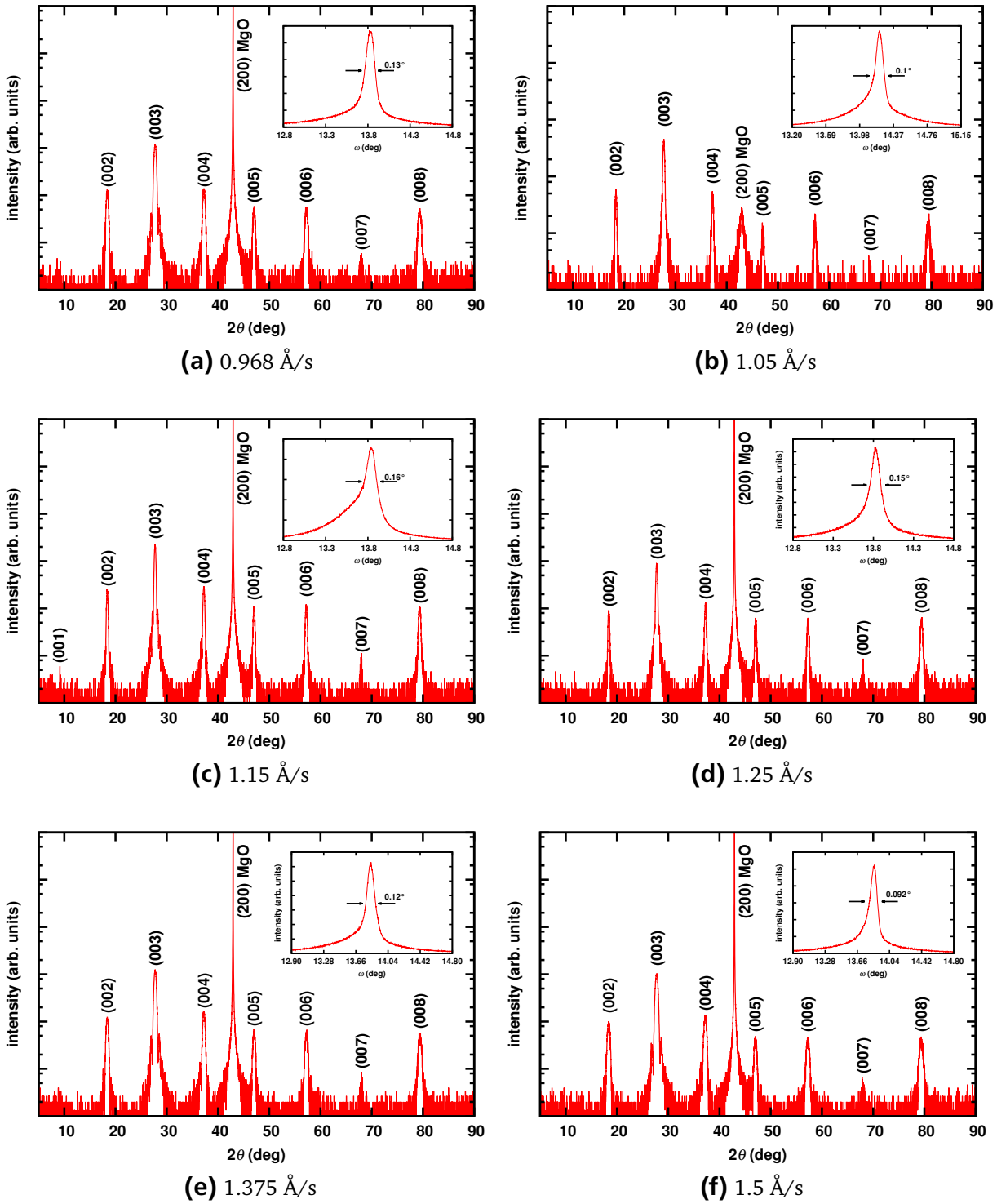

(a) 0.968 Å/s **(b)** 1.05 Å/s

(c) 1.15 Å/s **(d)** 1.25 Å/s

(e) 1.375 Å/s **(f)** 1.5 Å/s

Figure 7.25: $2\theta - \theta$ measurements of $CeNi_xBi_2$ films grown at various bismuth rates. The insets show the corresponding ω-scans of the (003) reflection of the $CeNi_xBi_2$ phase.

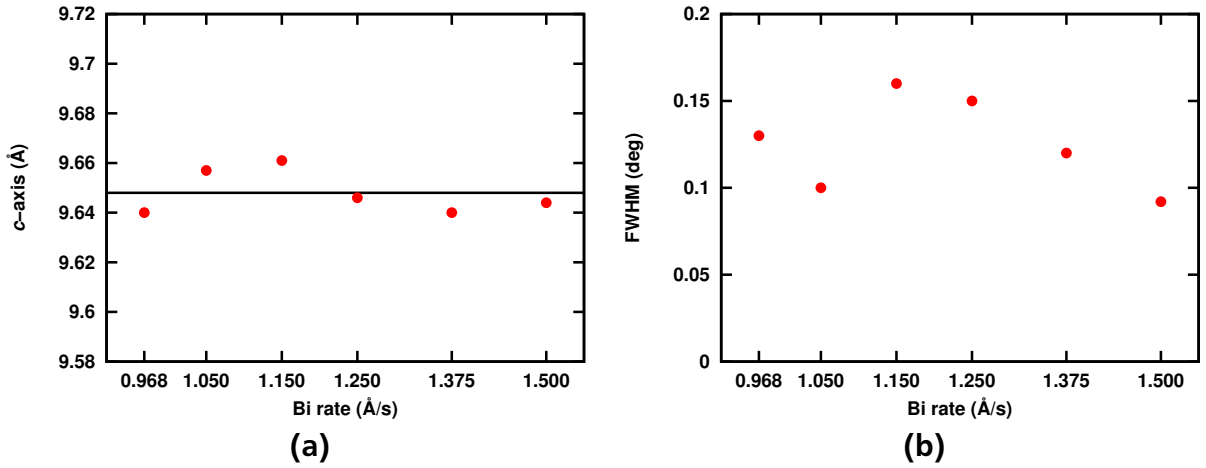

Figure 7.26: Trends of c-axis lattice parameter and FWHM of the ω-scans versus bismuth rate of the $CeNi_xBi_2$ films.

is 9.64 Ådetermined from the Nelson-Riley method. The inset of figure 7.25a shows the rocking curve of the grown $CeNi_xBi_2$ film. The FWHM determined through a fit of a Lorentz function is 0.13° which indicates a good crystal quality. The asymmetric nature of the ω-scan reflection indicates a strain in the film which is expected since the asymmetric Laue oscillations also indicate that [148]. Figure 7.25b–f show the $2\theta - \theta$-scans of the films grown with bismuth rates varying from 1.05 Å/s to 1.5 Å/s. The change in bismuth rate only had a minor effect on the c-axis lattice parameter. Figure 7.26a visualizes the variation of the c-axis lattice parameter with increasing bismuth rate. It can be seen that the c-axis value is in the range of 9.64 Å and 9.661 Å. A trend can not be derived from this data indicating an independent c-axis lattice parameter of the bismuth content. This was also the case for the $LaNi_xBi_2$ phase. For the c-axis lattice parameter of the $CeNi_xBi_2$ films an average value of 9.648 Å can be determined. This is in good agreement with the literature value of 9.641 Å reported by Kodama *et al.* [137].

But an increasing bismuth rate has an effect on the crystal quality of the $CeNi_xBi_2$ films. From the ω-scans of the (003) reflection of the $CeNi_xBi_2$ films shown in the insets if figure 7.25a–f the FWHM were determined. The results are summarized in figure 7.26b. It can be seen that the FWHM increases with increasing bismuth rate up to a maximum of 0.16° for the films grown at a bismuth rate of 1.15 Å/s. The reason for the low value at a bismuth rate of 1.05 is not clear at this point. Interestingly, a further increase in bismuth rate leads to a decrease in the FWHM and, thus, indicating a higher crystal quality for higher bismuth rates. One possible explanation for that could be excess bismuth which forms a liquid phase on top of the surface of the film and acts as a flux. The flux supports the crystal growth because of higher mobility of the atoms. The best crystallinity was achieved for the film grown at 1.5 Å/s with a FWHM of 0.092°.

Although, the film's quality is of importance in general, the scope of this thesis is on the superconducting properties of the grown films. Of course, the crystal quality of the films directly influences the superconducting properties. An important factor for superconductivity is the superconducting transition temperature T_C. For that reason attention, has to be turned to the influence of the bismuth rate on the transition temperature. For that the

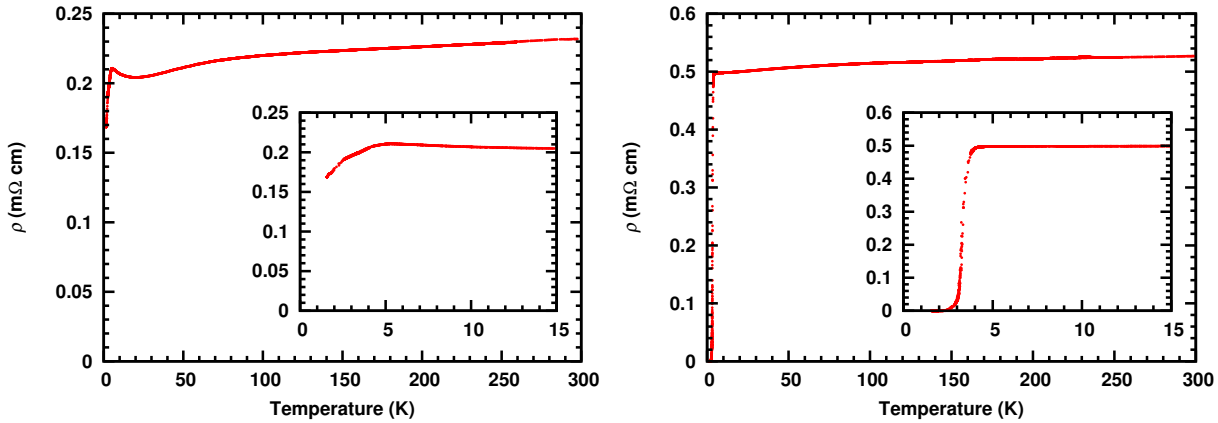

(a) 0.968 Å/s

(b) 1.05 Å/s

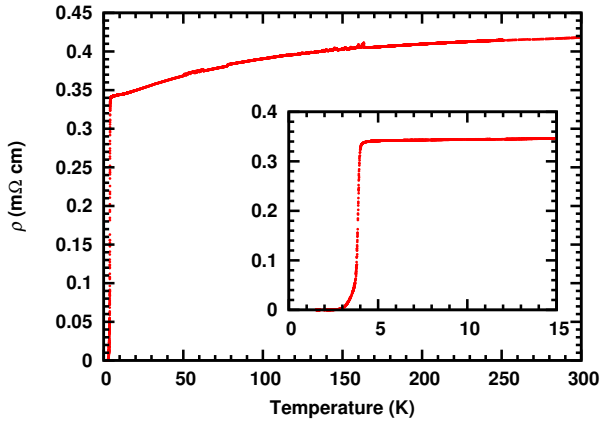

(c) 1.15 Å/s

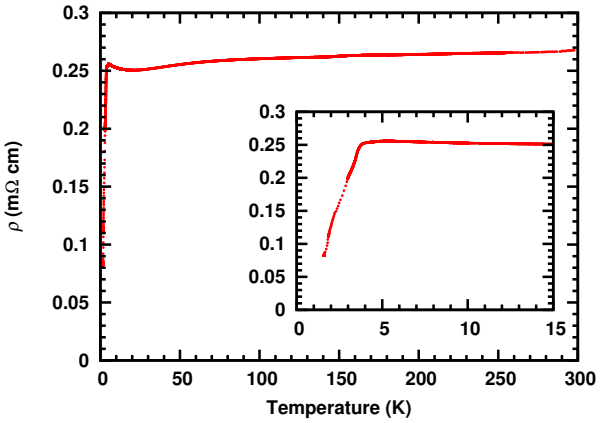

(d) 1.25 Å/s

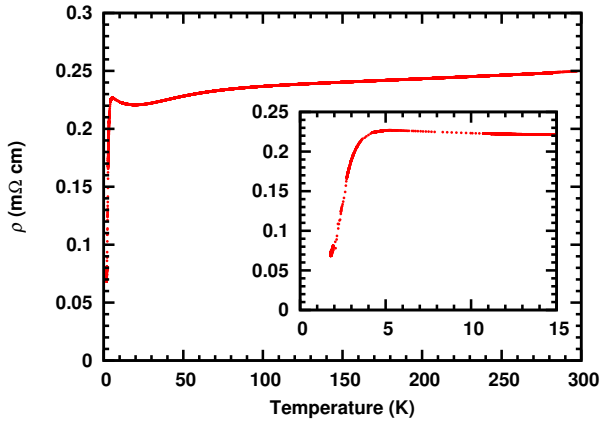

(e) 1.375 Å/s

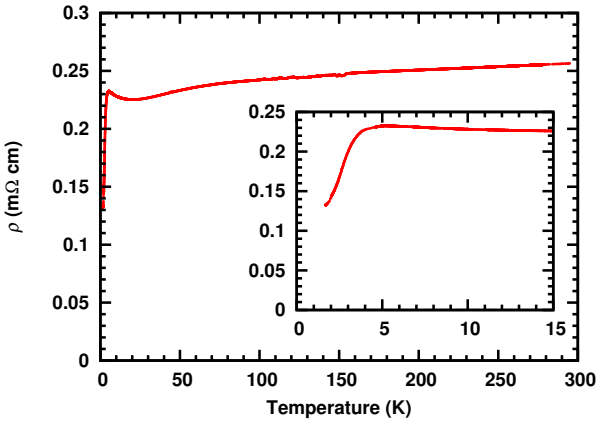

(f) 1.5 Å/s

Figure 7.27: ρ-T measurements of $CeNi_xBi_2$ films grown at various bismuth rates. The insets show an enlarged portion of the superconducting transition.

resistivity was measured in a temperature range of 300 K down to 1.5 K. The results are shown in figure 7.27. All the measured films reveal a superconducting transition onset, but only two of them exhibit a T_C zero.

The $CeNi_xBi_2$ film grown at a bismuth rate of 0.968 Å/s has the lowest room temperature resistivity of all the films in this series of various bismuth rates with a value of 232 $\mu\Omega$ cm. At the beginning of the temperature range, the resistivity shows a metallic behaviour. At ∼60 K, the slope changes and become steeper. At ∼20 K the resistivity reaches a minimum of 204 $\mu\Omega$ cm. At a temperature of 3.6 K, the T_C onset can be observed. The resistivity drops by 20% to a minimum of 169 $\mu\Omega$ cm at 1.5 K.

An increase in bismuth rate to a value of 1.05 Å/s leads to a different behaviour of the resistivity with decreasing temperature. First of all the room temperature resistivity is more than twice as high as for the film grown at 0.968 Å/s with a value of 527 $\mu\Omega$ cm. The resistivity stays almost constant over the whole temperature range with a slight trend down. At 3.65 K the resistivity reaches a value of 497 $\mu\Omega$ cm, only 5.7% below the room temperature value. At 3.65 K the resistivity drops until at 3 K T_C zero is observed. The ΔT could be determined to be 0.54 K.

The best results according to the superconducting properties have been achieved with the film grown at a bismuth rate of 1.15 Å/s. With a value of 418 $\mu\Omega$ cm the room temperature resistivity of this film is in the same range as the former film. The resistivity decreases over the whole range of measured temperature although the behaviour is not linear. The minimum resistivity of the normal state is reached at 4.1 K with a value of 340 $\mu\Omega$ cm. The superconducting transition can be observed at 4.13 K and with a ΔT of 0.31 K T_C zero is reached at 3.7 K. This is the highest measured value in this series of $CeNi_xBi_2$ films grown at various bismuth rates. Mizoguchi *et al.* [136] reported a T_C zero of 4 K for $CeNi_xBi_2$ which is still higher than the value measured for the film. But it has to be noticed that this series only concentrates on the bismuth content in the structure. The nickel is not optimized so far and one has to take other film specific properties like strain and the low film thickness itself into account. A further increase in bismuth rate leads to a room temperature resistivity of a value of 268 $\mu\Omega$ cm. The room temperature resistivity again reached values in the range of the film grown at 0.968 Å/s. A T_C onset can be observed at 3.74 K and a drop in resistivity by 76% occurs. A T_C zero is not detected.

The resistivity behaviour of the films grown at bismuth rates of 1.375 Å/s and 1.5 Å/s is similar to the other films. The room temperature resistivity is 250 $\mu\Omega$ cm for the film grown at 1.375 Å/s and 257 $\mu\Omega$ cm for the film grown at 1.5 Å/s. The minimum for both films is at ∼ 12% of the room temperature resistivity (221 $\mu\Omega$ cm for 1.375 Å/s and 225 $\mu\Omega$ cm for 1.5 Å/s). A T_C onset can be observed for both of the films. The film grown at 1.375 Å/s shows an onset at 3.67 K and a drop in resistivity of 69% while the film grown at 1.5 Å/s has an onset at 3.73 K and a drop in resistivity of 42%.

A summary of the results is visualized in figure 7.28. It is interesting to see that the films which exhibit a T_C zero have higher room temperature resistivities, while all the other films without T_C zero are in the same range around 230 $\mu\Omega$ cm. A similar picture can be observed for the T_C onset (figure 7.28b). Almost all the films have T_C onsets close to each other. Only the film which seems to have the optimal bismuth content exhibit a much higher onset and shows the highest T_C zero of 3.7 K. The gray area in figure 7.28b indicates the optimum bismuth rate for the growth of superconducting $CeNi_xBi_2$ films and was used to optimize the nickel content of the structure. In comparison to reported bulk data in

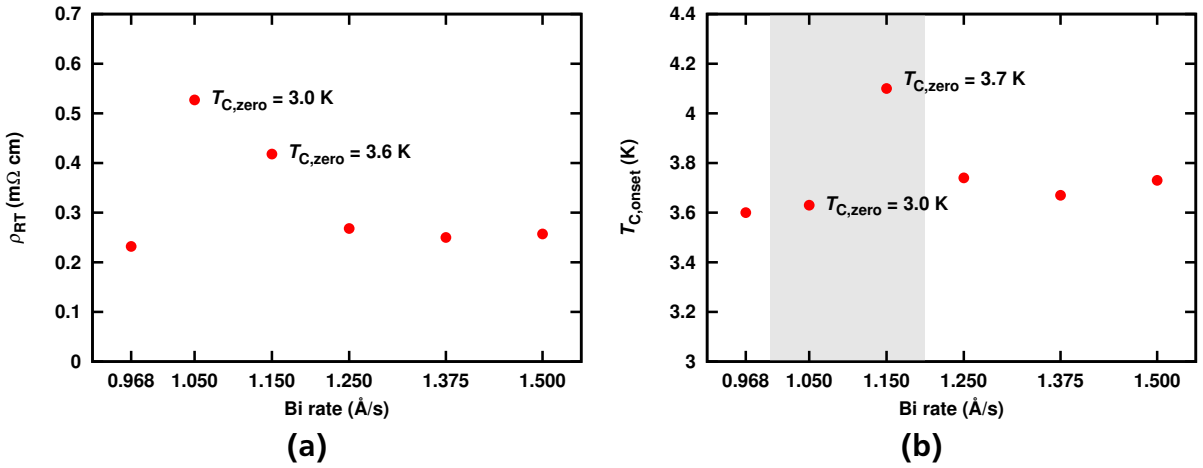

Figure 7.28: a) Variation of room temperature resistivity and b) and variation of T_C onset of the $CeNi_xBi_2$ films grown at various bismuth rates.

literature, the $CeNi_xBi_2$ films grown here exhibit a much higher quality than it was achieved for the bulk samples. Kodama *et al*. [137] report about the synthesis of $CeNi_xBi_2$. They deal with high level of impurities of Ni, NiBi and $NiBi_3$. While the NiBi impurities are only observed for films grown at higher bismuth rates, the other mentioned do not appear in the $CeNi_xBi_2$ films grown by RMBE. Since for characterizing the superconducting properties it is necessary to have high quality samples, the approach of sample preparation via MBE as a thin film technique is superior over the bulk preparation. And for a study of the influence of nickel deficiencies on the physical properties of the $CeNi_xBi_2$ compound MBE is a much more flexible tool because of the relative easy way of producing samples with different compositions. This is described in the next section.

7.4.2 Influence of the nickel rate

Similar to the $LaNi_xBi_2$ compound not only the bismuth content plays a role for the superconducting properties of the thin films but also the nickel content is of importance. From ICP-OES measurements it is known that a nickel rate of 0.054 Å/s lead to an almost stoichiometric compound. For this reason only a series of decreasing nickel rates was done and the attention was turned on the resistivity measurements since the superconducting properties of the films are of major interest. For the bismuth rate the best result for superconductivity was chosen and thus a bismuth rate of 1.15 Å/s was used for film deposition. The results of the resistivity measurements are shown in figure 7.29. All films grown within this series of various nickel rates show a metallic temperature behaviour of the resistivity and exhibit a superconducting transition with a T_C zero. The $CeNi_xBi_2$ film grown at 0.054 Å/s nickel rate has a room temperature resistivity of 418 $\mu\Omega$ cm. With decreasing temperature the resistivity decreases constantly. The ratio $\rho_{300\ K}/\rho_{10\ K}$ is ~1.2 indicating a poor metallic behaviour. At 4.1 K the superconducting transition occurs and a drop in resistivity down to zero can be observed. T_C zero is determined to be 3.7 K with a ΔT of 0.31 K.

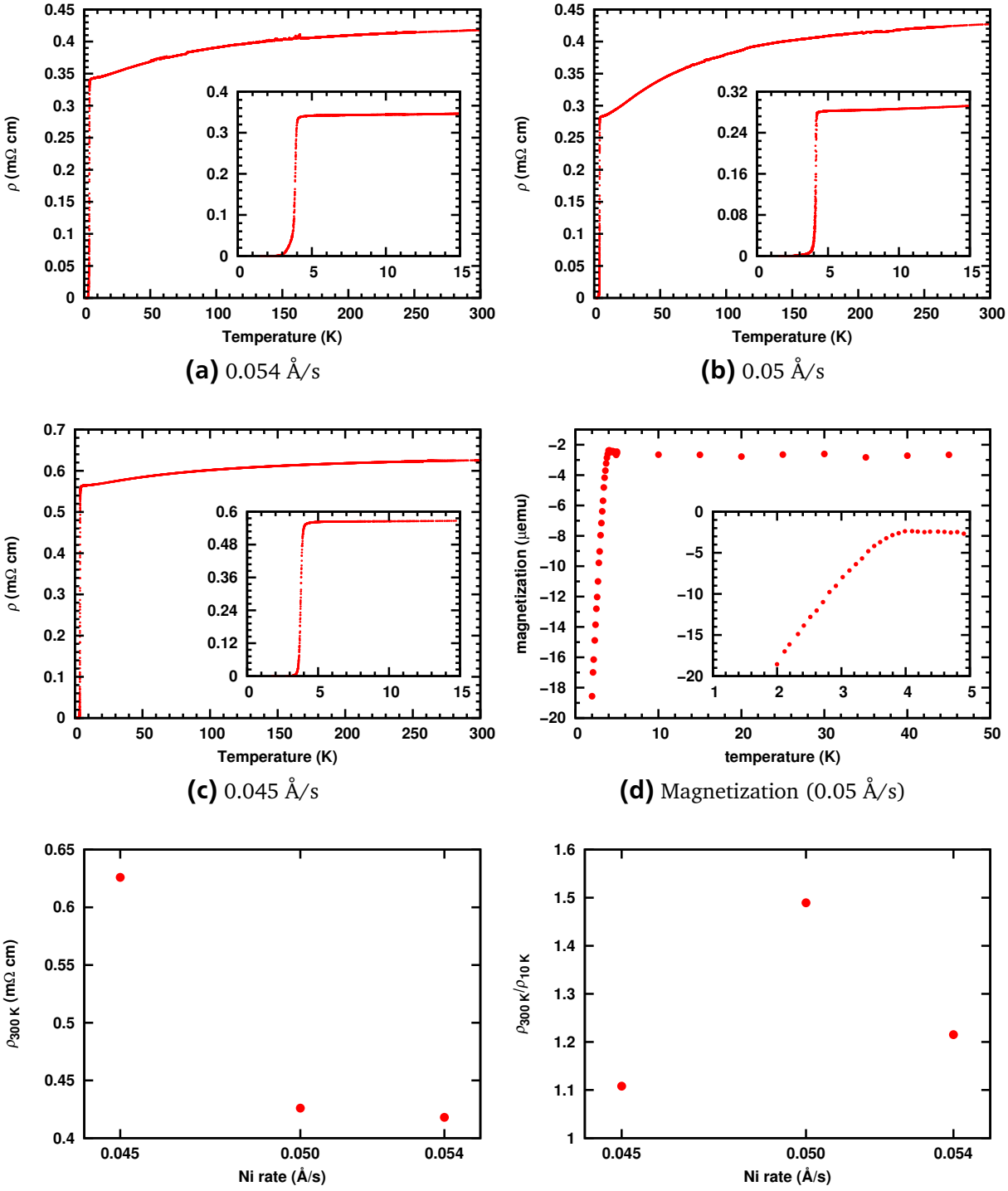

(a) 0.054 Å/s **(b)** 0.05 Å/s

(c) 0.045 Å/s **(d)** Magnetization (0.05 Å/s)

(e) Room temperature resistivity versus nickel rate. **(f)** Ratio of room temperature resistivity and resistivity at 10 K versus nickel rate.

Figure 7.29: a) – c) resistivity measurements of $CeNi_xBi_2$ films grown at various nickel rates and d) diamagnetic response of the superconducting $CeNi_xBi_2$ film measured with magnetic field of 10 Oe perpendicular to film surface. The insets show an enlarged portion of the superconducting transition. e) Room temperature resistivity and f) ratio of room temperature resistivity and resistivity at 10 K of the $CeNi_xBi_2$ films grown at various nickel rates.

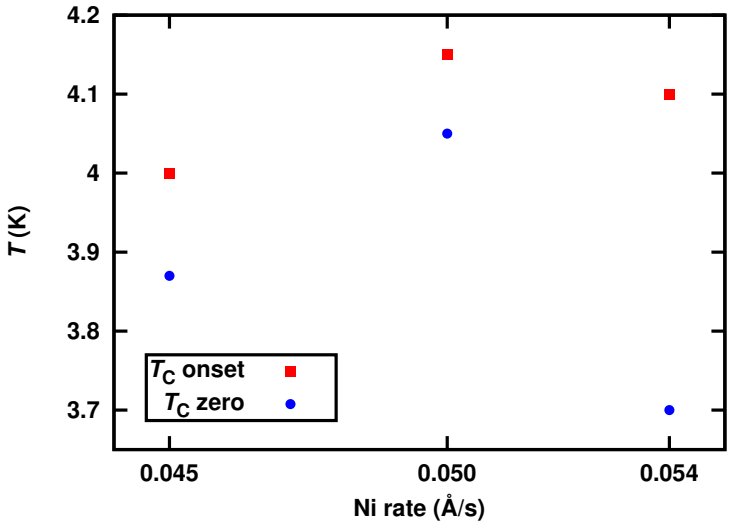

(a) T_C onset and T_C zero versus nickel rates.

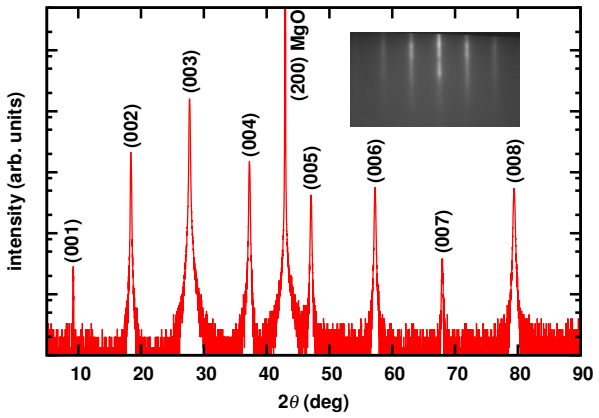

(b) $2\theta - \theta$-scan, inset shows the RHEED pattern after deposition.

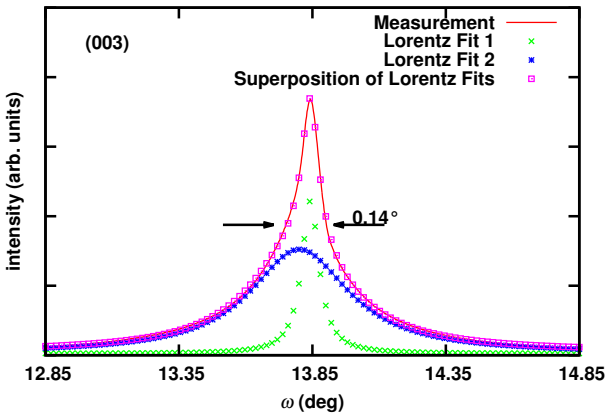

(c) ω-scan

Figure 7.30: a) T_C onset and T_C zero versus nickel rates and b–c) X-ray measurements of the $CeNi_xBi_2$ film grown at a nickel rate of 0.05 Å/s.

The best results in this series of $CeNi_xBi_2$ films grown at various nickel rates were obtained with a nickel rate of 0.05 Å/s. The room temperature resistivity is very close to the one of the former film with a value of 426 $\mu\Omega$ cm. In this film the ratio of $\rho_{300\ K}/\rho_{10\ K}$ has a value of ∼1.5. This is still a bad metal but more metallic than the films grown at 0.054 Å/s and 0.045 Å/s of nickel rate. A visualization of the variation of $\rho_{300\ K}/\rho_{10\ K}$ with nickel rates is shown in figure 7.29f. At 4.15 K the superconducting transition occurs and with a ΔT of 0.08 K T_C zero is determined to be 4.05 K. This value is in very good agreement with reported values by Mizoguchi *et al.* [136] and Kodama *et al.* [137]. In a temperature range of 6 to about 20 K a highly metallic behaviour can be observed for the resistivity. The dependence follows a quadratic $\rho(T) = \rho_0 + AT^2$ function with $A \approx 50$ nΩcm/K^2. This value is 2 to 5 times higher than reported values for $SrMnBi_2$ or pure bismuth [138, 149]. In figure 7.29d the diamagnetic response measured with a SQUID magnetometer is shown and confirms the superconducting nature of the $CeNi_xBi_2$ film.

Beside the fact that the film grown at 0.05 Å/s shows a T_C comparable to values reported in literature a second indication for optimum nickel content at this nickel rate is a decreasing T_C with further decrease in nickel rate. Figure 7.29c shows the resistivity measurement of the film grown at 0.045 Å/s. The room temperature resistivity is significantly higher compared to the films grown at higher nickel rates with a value of 626 $\mu\Omega$ cm. Although this film also shows a decreasing resistivity with decreasing temperature the decrease is not as strong as for the optimal doped film and the ratio of $\rho_{300\ K}/\rho_{10\ K}$ is with a value of ∼1.1 in the same range of the $CeNi_xBi_2$ film grown at 0.054 Å/s nickel rate. This also indicates the poor metal nature of the $CeNi_xBi_2$ films. The T_C onset is observed at 4.0 K and T_C zero is measured at 3.87 K with a ΔT of 1 K.

The film grown at a nickel rate of 0.05 Å/s which shows the best superconducting properties has a thickness of ∼100 nm. $2\theta - \theta$ measurement and ω-scan are shown in figure 7.30b and c. The inset of figure 7.30b shows the RHEED image of the $CeNi_xBi_2$ film after the growth process. The streaky pattern indicates the smooth and epitaxial growth of the film. The $2\theta - \theta$ measurement presented in figure 7.30b exhibit only $(00l)$ reflections of the desired $CeNi_xBi_2$ compound and no impurity phase can be observed. All the $(00l)$ reflections from (001) to (008) are present. Because of the thickness of 100 nm Laue oscillations can not be seen in this $2\theta - \theta$-scan of the film. The c-axis lattice parameter is determined to be 9.651 Å from the Nelson-Riley method which is in good agreement with literature values for $CeNi_xBi_2$ [136, 137]. The ω-scan for this film is shown in figure 7.30c. Also this film exhibit the already observed asymmetry of the ω-scan indicating strain in the film. The FWHM is rather high with a value of 0.14° compared to the $LaNi_xBi_2$ films and corresponds to the FWHM determined for the best $CeNi_xBi_2$ film grown in the bismuth series (section 7.4.1). The FWHM of 0.14° is not as good as for other thin films grown of the $CeNi_xBi_2$ compound but still indicates a good crystal quality. To determine the stoichiometry of the $CeNi_xBi_2$ films ICP-OES measurements of the superconducting films were carried out and the x in $CeNi_xBi_2$ could be determined to be 0.86 for the film grown at a nickel rate of 0.05 Å/s. This results in a compound of $CeNi_{0.86}Bi_2$ and is in good agreement with the reports of Mizoguchi *et al*. [136] who reported their best T_C for an $x = 0.8$.

However, to be sure that doping only happens on the nickel site and not on the bismuth site, a set of films with various nickel content were deposited at a higher bismuth rate of 1.5 Å/s. The high bismuth rate makes sure that the bismuth site in $CeNi_xBi_2$ is fully occupied. The results of the resistivity measurements are shown in figure 7.31. In this set of measurements only the films grown between nickel rates of 0.045 Å/s and 0.062 Å/s are shown. Films grown above a nickel rate of 0.062 Å/s exhibit strong impurity peaks of the NiBi compound (see figure 7.32a) and thus the resistivity measurements are not reliable any more because it can not be distinguished whether a observed T_C is from the $CeNi_xBi_2$ phase or the NiBi phase. All films grown in this series of various nickel rates exhibit a T_C onset but no T_C zero. All the T_C onsets are close to 4 K (see figure 7.31f). The T_C onset of the film grown at 0.066 Å/s is significantly higher compared to the other T_C onsets and is probably a results of the NiBi impurities which were observed in the X-ray measurements (figure 7.32).

Figure 7.32a and b show the $2\theta - \theta$ measurements of the $CeNi_xBi_2$ films grown at a nickel rate of 0.062 Å/s and 0.066 Å/s with a bismuth rate of 1.5 Å/s. As it can be seen already at a nickel rate of 0.062 Å/s the NiBi impurity phase starts to form, although it is not very prominent at this stage. As described above this film still had a T_C onset comparable to the

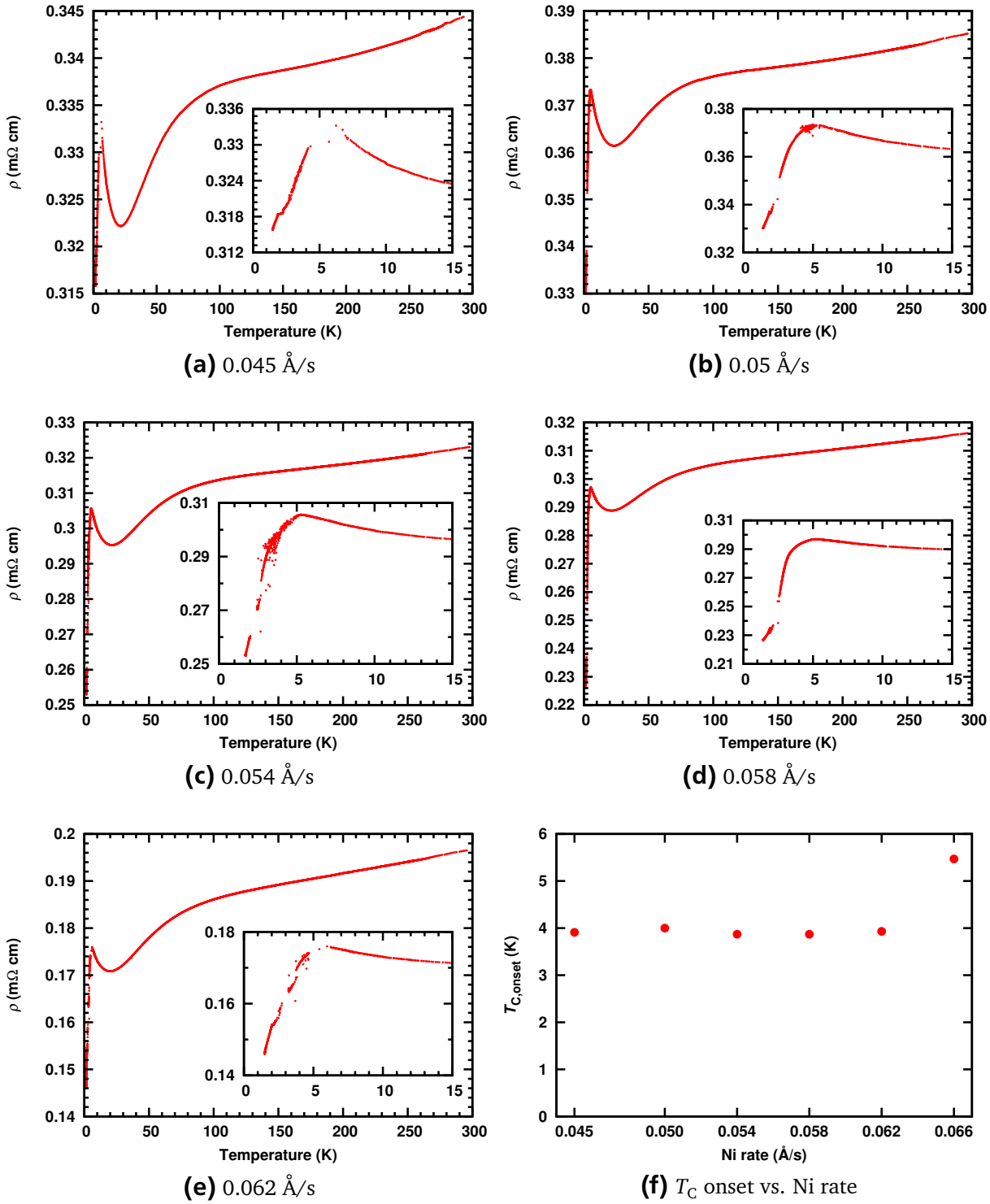

Figure 7.31: a) – e) ρ-T measurements of $CeNi_xBi_2$ films grown at different nickel rates with a bismuth rate of 1.5 Å/s. The insets show an enlarged portion of the superconducting transition. f) T_C onset versus nickel rate.

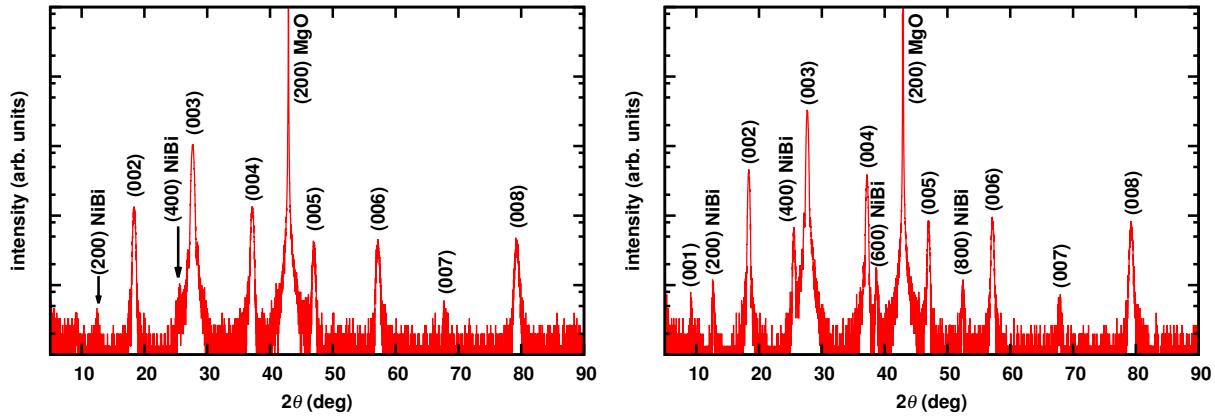

(a) $2\theta - \theta$ measurement of film grown at 0.062 Å/s **(b)** $2\theta - \theta$ measurement of film grown at 0.066 Å/s

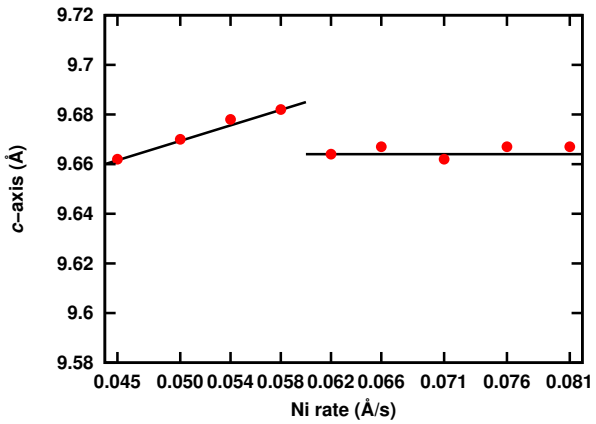

(c) c-axis lattice parameter vs. Ni rate

Figure 7.32: a) $2\theta - \theta$ measurement of the $CeNi_xBi_2$ film grown at a nickel rate of 0.062 Å/s and b) a nickel rate of 0.066 Å/s. Both were grown at a bismuth rate of 1.5 Å/s. c) Variation of c-axis lattice parameter with Ni rate.

films which do not exhibit the NiBi impurity phase in the $2\theta - \theta$ measurement. On the other hand, the c-axis lattice parameter is already different compared to the other films within this study grown at lower nickel rates. Figure 7.32c visualizes the variation of c-axis lattice parameter with various nickel rates. It can be seen that the c-axis lattice parameter increases with increasing nickel rate. This is valid for nickel rates between 0.045 Å/s an 0.058 Å/s. At 0.062 Å/s, where the first evidence of the NiBi impurity phase was observed, the c-axis lattice parameter exhibit a drop to lower values which stay constant with further increase in the nickel rate at a value of ∼9.668Å. This indicates that excess nickel incorporates in the NiBi structure and not in the $CeNi_xBi_2$ structure.

The results suggest, that the optimum bismuth rate for the thin film deposition of $CeNi_xBi_2$ is 1.15 Å/s. In addition, the optimum nickel rate was found to be 0.05 Å/s. The optimal source rates were found to be 0.2 Å/s for cerium, 0.05 Å/s for nickel and 1.15 Å/s for bismuth. The optimum growth temperature was found to be 430 °C. With these parameters it is possible to grow high quality superconducting $CeNi_{0.86}Bi_2$ thin films with reactive molecular beam epitaxy. The films grown with these parameters have a T_C zero as high as 4.05 K which is in very good agreement with reported values in literature [136]. Although

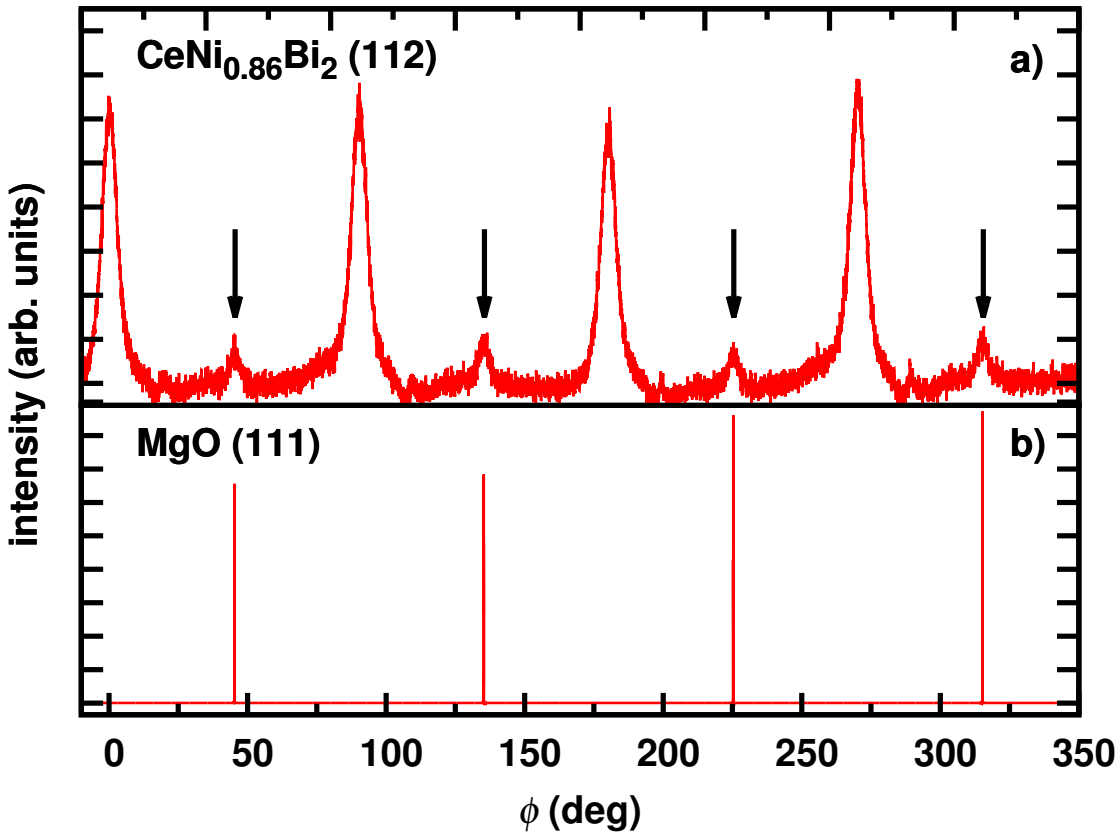

Figure 7.33: a) ϕ-scan of the (112) reflection of the $CeNi_xBi_2$ film and b) of the (111) reflection of the MgO substrate.

the films grown at the optimal parameters exhibit good superconducting qualities the best films in terms of crystallinity were grown at higher bismuth rates of 1.5 Å/s and nickel rates slightly above the optimum at 0.054 Å/s. With these parameters rocking curves with a FWHM of 0.092° were observed while the optimum rates exhibit a rocking curve FWHM of 0.14°. Nevertheless, the stability is similar to the on of the $LaNi_xBi_2$ films described in section 7.3.5. Samples stored in dried air at ∼10–20% humidity decomposed after roughly 2–3 days while samples exposed to humid air of 60% humidity decomposed within a few hours.

7.4.3 Epitaxial relation to the substrate

After the optimal parameters for good crystal quality and good superconducting properties have been found, the epitaxial relation of the $CeNi_xBi_2$ film to the substrate had to be clarified. In the case of $LaNi_xBi_2$ the phase grows 45° rotated with respect to the substrate.

For that a ϕ-scan of the (112) reflection of $CeNi_xBi_2$ and the (111) reflection of the MgO substrate was done. The results are shown in figure 7.33. As it can be seen, the growth feature is similar to the one of the $LaNi_xBi_2$ phase. The $CeNi_xBi_2$ phase also grows 45° rotated with respect to the MgO substrate. But in this case of the $CeNi_xBi_2$ phase the domains which grow "cube-on-cube" on the substrate are more prominent (see arrows in figure 7.33a). However, the ϕ-scan clearly reveal that the major part of the domains of

the $CeNi_xBi_2$ films and the MgO peaks exhibit a offset of 45°. This lead to an epitaxial relation of $CeNi_xBi_2$ [100] || MgO [110] and $CeNi_xBi_2$ [001] || MgO [001]. Also from the ϕ-scan the a-axis lattice parameter can be determined to be 4.565 Å which is in good agreement with reported literature values [136]. As in the case of the $LaNi_xBi_2$ compound, also here the rotation of 45° can not be due to a mismatch of the lattice parameters between substrate and film since that is only 8%. The most likely reason for the rotation is due to the atomic rearrangement which was already suggested for the $LaNi_xBi_2$ films (figure 7.21 in section 7.3.4). However, the energy difference between rotated and not rotated films seems to be small since a considerable number of domains are aligned $CeNi_xBi_2$ [100] || MgO [100]. Reason for that could be small differences in interfacial atomic composition of the $CeNi_xBi_2$ film and the substrate. If the reason is an energetic one, various growth temperatures should lead to single domains with either non-rotated or 45° rotated grains. Because of the small temperature window for the formation of the $CeNi_xBi_2$ phase this is a challenging task which was not attempted.

7.4.4 X-ray reflectivity measurement of $CeNi_xBi_2$

The picture for the $CeNi_xBi_2$ films is similar to the $LaNi_xBi_2$ phase. Again already the asymmetry in the Laue oscillations suggested a density difference over the film thickness. To study the difference of the density, an X-ray reflectivity measurement of a $CeNi_xBi_2$ film grown at the optimal parameters was done. The results of the scan are shown in figure 7.34. In the scan oscillations up to an angle of 3° are observed. The angle of total reflection is determined to be ∼0.1°. This data also was fitted with the analysis software GXRR3 from Rigaku Corporation. The results of the fit are shown in table 7.4.

Table 7.4: Fitting results for the X-ray reflectivity measurement of the $CeNi_xBi_2$ film.

Layer	Thickness (nm)	Density ($\frac{g}{cm^3}$)	Roughness (nm)
3 (Bi)	2.247	7.55	1.06
2 ($CeNi_xBi_2$)	23.456	10.71/8.86	1.38
1 (Ni)	4.042	8.88	1.307
Sub (MgO)	—	3.585	0.406

Best fit results were obtained with a multilayer structure as it is shown in table 7.4 and in the inset of figure 7.34. The model is very similar to the one used for the $LaNi_xBi_2$ films (section 7.3.6. Again a Ni "‘buffer-layer"’ and a Bi top layer is found with thicknesses of ∼4 nm and ∼2.2 nm, respectively. The $CeNi_xBi_2$ layer is determined to be roughly 23.5 nm thick. The density was fitted with a linear variation along the layer in c-direction. The density at the bottom is determined to be 10.71 g/cm^3. This ∼7 % above the density of $CeNi_xBi_2$ which is determined to be 10.04 g/cm^3. The top density is determined to be 8.86 g/cm^3 and thus ∼12 % below the theoretical density of $CeNi_xBi_2$.

As already stated in the chapter about $LaNi_xBi_2$ the reason for that behaviour is not clear. The density variation can be a result of stoichiometry variations perpendicular to the film surface or may even be a result of film decomposition starting from the top of the film. A decomposition starting from the top is suggested by an experiment were a film is

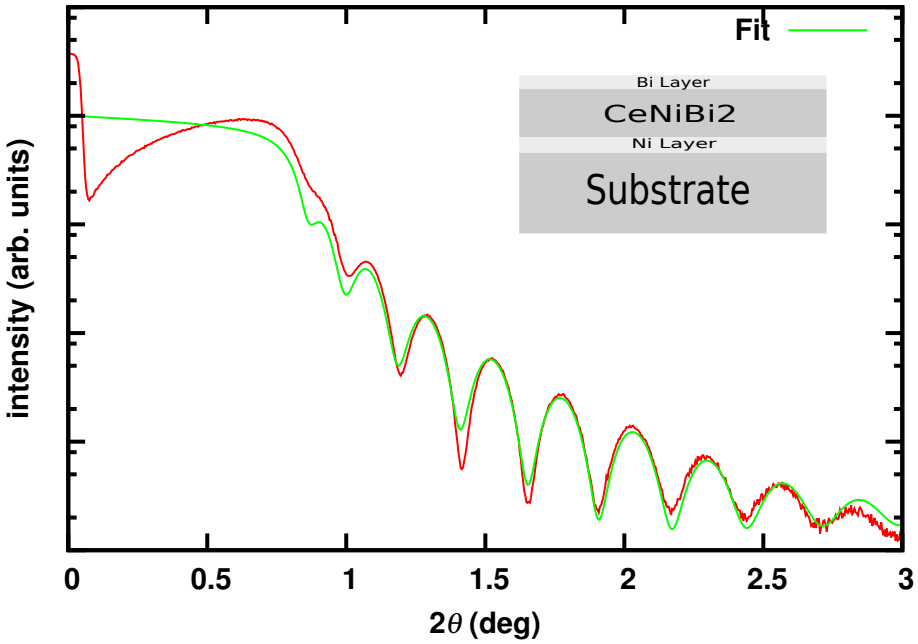

Figure 7.34: X-ray reflectivity measurement and the results of a fitting procedure of the $CeNi_xBi_2$ film grown at optimum parameters. The inset shows a scheme of the model which was used for the fitting procedure.

taken out of the chamber, exposed to air for a few seconds and directly locked back into the chamber again. RHEED images taken before and after this process showed a major difference. While the film before the take out did show clear and bright streaks, the RHEED picture after the exposure to atmosphere did not show a diffraction pattern anymore. This behaviour indicates a fast decomposition directly after the exposure to air starting from the film surface.

7.5 Substitution

One big advantage of the MBE technique is the possibility of substitute one element by another if the growth parameters are known. Since the optimum growth parameters for $LaNi_xBi_2$ and $CeNi_xBi_2$ were found substituting different elements in these compounds is the next step. The substitution of lanthanum by cerium did work quite well. The logical choice for a substitution is the transition metal site. One appropriate candidate for substituting nickel is iron, cobalt or copper. Iron and cobalt are already known in the field of pnictide superconductors and iron containing compounds exhibit superconducting transition temperatures of up to 56 K. However, the first choice in this thesis for a nickel substitute was copper. The main reason for that is described in section 7.2. The idea is to substitute the relative nonmagnetic nickel ions by the more magnetic copper ions since it is known from the undoped cuprate superconductors that the copper ions order antiferromagnetically.

For the bismuth site in principle the elements of the whole pnictide group starting with nitrogen down to antimony would be good candidates. For a starting, antimony was tried for a substitute since it is already known that $LaNi_xSb_2$ grows on MgO substrates using MBE.

The case for nitrogen is much more challenging and although there were a few attempts to grow nitrogen containing films the results are not conclusive and much more work need to be done on nitrogen compounds. Because of that the nitrogen films will not be discussed in this thesis.

Because of a lack of time these compounds were not studied as deep as it was done for $LaNi_xBi_2$ and $CeNi_xBi_2$. The next sections should be seen as a starting point for future research on these compounds and only give a short introduction into the potential of a successful thin film deposition using MBE.

7.5.1 $CeCu_xBi_2$

The first attempt to substitute the nickel by copper was done in the $CeNi_xBi_2$ compound. Reason for that is first of all the existing reports on copper containing '112'-compounds with cerium and bismuth [150]. A second reason is the higher T_C zero observed in $CeNi_xBi_2$ compared to the $LaNi_xBi_2$ phase. As a starting point, the optimal rates for the growth of $CeNi_{0.86}Bi_2$ were set which are 0.2 Å/s for cerium rate, 0.054 Å/s for copper rate, 1.15 Å/s for bismuth rate and 430 °C as growth temperature. To overcome the differences in density of copper and nickel the copper rate was adjusted accordingly.

Already the first attempt to grow the copper containing '112'-type compound was successful (figure 7.35a). Only (00l) reflections of the $CeCu_xBi_2$ phase are observed. The X-ray data was compared to data reported by Ye *et al.* [151] to confirm the formation of $CeCu_xBi_2$. There are no impurity reflections present in the $2\theta - \theta$ scan. The pattern is similar to the X-ray scans done for the $LaNi_xBi_2$ and $CeNi_xBi_2$ compounds. Only the (007) peak is not present in this X-ray scan and the (003) reflection exhibit a small shoulder on the right side which can not be identified. The c-axis lattice parameter can be determined to be 9.77 Å which is in agreement with values reported in literature [150, 151].

For the next attempt of the deposition of $CeCu_xBi_2$, the substrate temperature was lowered to 405 °C. This step was done because the RHEED picture during the deposition process suggested a lower growth temperature to be better for the formation of the $CeCu_xBi_2$ phase. Figure 7.35b shows the X-ray result of the film grown with these parameters. The shoulder observed for the (003) reflection disappeared in this $2\theta - \theta$ scan and the (007) peak appeared in the diffraction pattern. At 89.5° another peak can be identified which corresponds to the (009) reflection of the $CeCu_xBi_2$ structure. The c-axis lattice parameter is in the same range and was determined to be 9.808 Å. A further reduction in deposition temperature to 390 °C did not show any further improvement in the XRD results. However, the (007) peak disappeared again in the $2\theta - \theta$ scan while the (009) reflection still can be observed. The c-axis lattice parameter is determined to be 9.852 Å.

However, the aim of this section is to give a short overview of the possibility to substitute different sites and to find novel superconducting compounds which exhibit higher T_C values. Since the last results show that a phase formation of $CeCu_xBi_2$ is possible and the X-ray measurements confirm a phase-pure and textured growth the attention was turned more on the electrical transport properties of the thin films and to see if there is a T_C in copper deficient samples. For this purpose, a copper rate scan was carried out and a series of $CeCu_xBi_2$ samples was grown at various copper rates. The results of the resistivity measurements for these films are shown in figure 7.36.

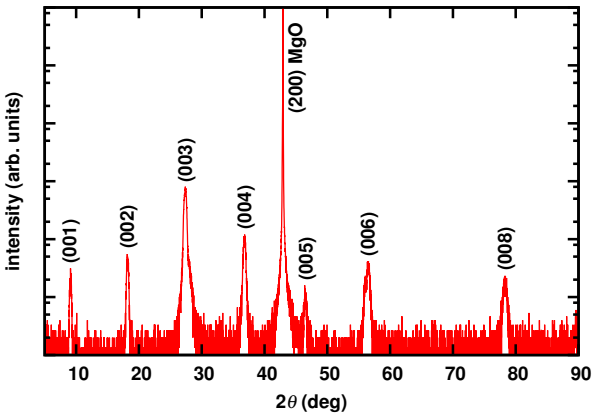

(a) $2\theta - \theta$ measurement of film grown at 430 °C

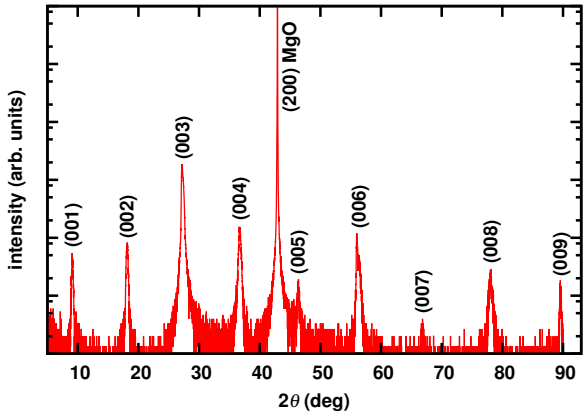

(b) $2\theta - \theta$ measurement of film grown at 405 °C

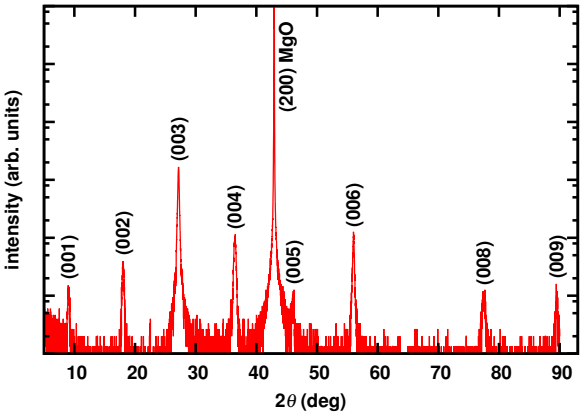

(c) $2\theta - \theta$ measurement of film grown at 390 °C

Figure 7.35: a) $2\theta - \theta$ measurement of the $CeCu_xBi_2$ film grown at a deposition temperature of 430 °C, b) 415 °C and c) 400 °C. The X-ray data for $CeCu_xBi_2$ were compared to reference [151].

The $CeCu_xBi_2$ films exhibit a totally different temperature behaviour of the resistivity as the $LaNi_xBi_2$ and the $CeNi_xBi_2$ films. While the nickel '112'-type films mostly show a metallic behaviour in the copper '112' films grown above 0.04 Å/s an increasing resistivity with decreasing temperature is observed. The film grown at 0.054 Å/s copper rate had a room temperature resistivity of 564 $\mu\Omega$ cm and increases to a maximum value of 720 $\mu\Omega$ cm at a temperature of 12 K. With further decreasing temperature the resistivity also starts to decrease until the minimum measurement temperature of 4.2 K is reached. Down to 4.2 K a T_C onset could not be observed.

The $CeCuBi_2$ film grown at a copper rate of 0.05 Å/s exhibit a similar resistivity behaviour. The resistivity also increases with decreasing temperature from a room temperature resistivity of 738 $\mu\Omega$ cm. Below 11.5 K the resistivity decreases again and a drop like feature can be observed. The inset of figure 7.36b shows an enlarged portion of this drop like feature. At this point further measurements are necessary to explain the nature of this drop. Either magnetization measurements or resistivity measurements at temperatures below 4.2 K could clarify this. Unfortunately the $CeCu_xBi_2$ films show a much more unstable behaviour in air than it was observed for $LaNi_xBi_2$ or $CeNi_xBi_2$ films.

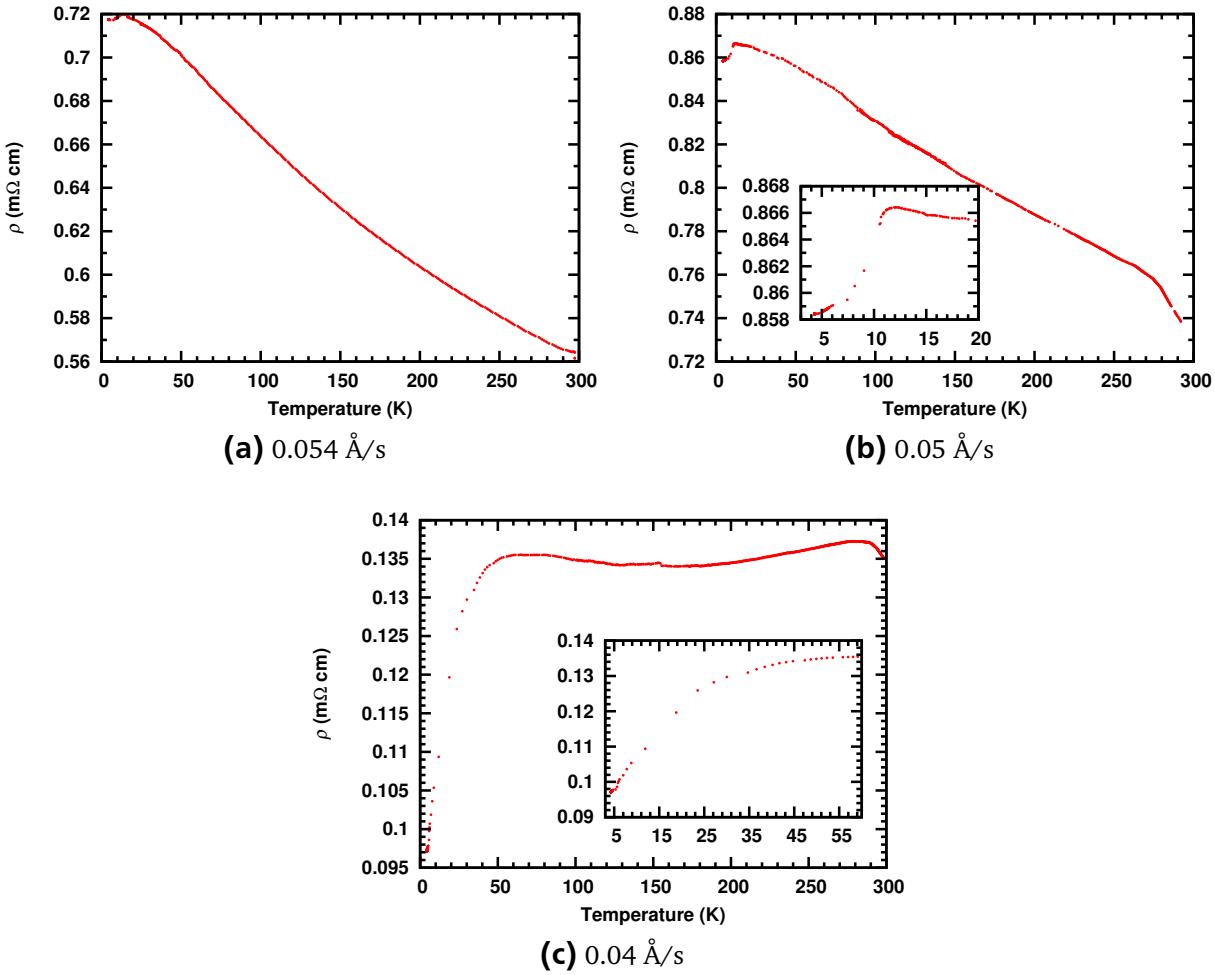

(a) 0.054 Å/s **(b)** 0.05 Å/s

(c) 0.04 Å/s

Figure 7.36: Resistivity measurements of the $CeCu_xBi_2$ films grown at various copper rates.

Further reduction in copper rate lead to a totally different behaviour (figure 7.36c). The film grown at 0.04 Å/s has a room temperature resistivity of 135 $\mu\Omega$ cm which is much lower compared to the $CeCu_xBi_2$ films grown at copper rates of 0.05 Å/s and 0.054 Å/s. The resistivity first increases slightly down to a temperature of 285 K. Below that the resistivity become a more metallic characteristic and decreases slightly until a temperature of 160 K is reached. At this temperature the resistivity curve has a minimum with a value of 133 $\mu\Omega$ cm. A further decrease in temperature lead to an increase in resistivity down to a temperature of ∼59 K. Here a resistivity value of 134 $\mu\Omega$ cm can be measured. This means overall the resistivity stays more or less constant over the whole temperature range down to ∼60 K. Below 60 K the resistivity starts to drop down to a value of 97 $\mu\Omega$ cm at 4.2 K (drop of 28%). Only a magnetization measurement could clarify this. This was not possible due to the instability of the film in air. Another possible reason for the resistivity behaviour observed in this film could be contact problems during the measurement. However, it was shown that the growth of $CeCu_xBi_2$ films is also possible with MBE. The data presented here is only a starting point for further investigation and parameter optimization. But it could be shown, that MBE is a powerful tool for doing that.

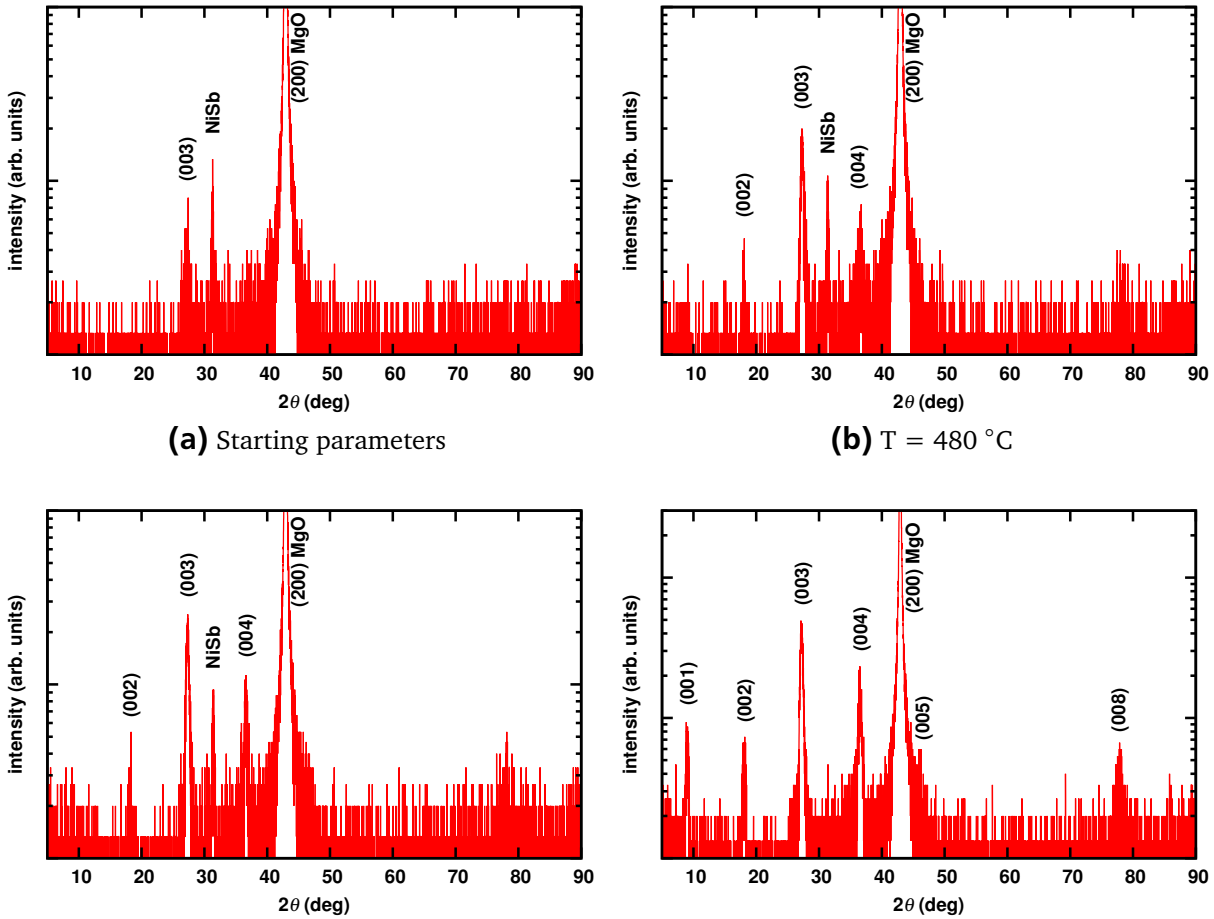

(a) Starting parameters **(b)** T = 480 °C

(c) Sb rate = 0.24 Å/s, T = 480 °C **(d)** Sb rate = 0.24 Å/s, T = 525 °C

Figure 7.37: $2\theta - \theta$ measurements of the $CeNi_xSb_2$ films grown at various antimony rates and growth temperatures.

7.5.2 $CeNi_xSb_2$

For a substitute on the pnictide site in the '112' bismuth compounds antimony is one possibility. The advantage of antimony over e.g. nitrogen is the possibility to evaporate it from solid sources. This makes the procedure more straight forward. In addition, the growth parameters are already known for $LaNi_xSb_2$. The parameters for the first attempt were 0.09 Å/s for cerium rate, 0.021 Å/s for nickel rate, 0.2 Å/s for the antimony rate and a growth temperature of 445 °C. One has to notice, that the evaporation characteristics for bismuth and antimony are totally different. While bismuth melts at ∼200 °C and evaporates at ∼500°C, antimony sublimes from its solid state. One big challenge in evaporating antimony is the stability of the source. To overcome the issues here and to have more control over the deposition process, the elemental rates where set rather low compared to the deposition of $LaNi_xBi_2$, $CeNi_xBi_2$ and $CeCu_xBi_2$.

Already the first attempt to grow a $CeNi_xSb_2$ film succeeded and phase formation was observed. Figure 7.37a shows the $2\theta - \theta$ measurement of the grown $CeNi_xSb_2$ film. The most intense peak belongs to a NiSb phase [152]. In addition the (003) reflection of the desired $CeNi_xSb_2$ phase could be detected [153]. To support phase formation the growth

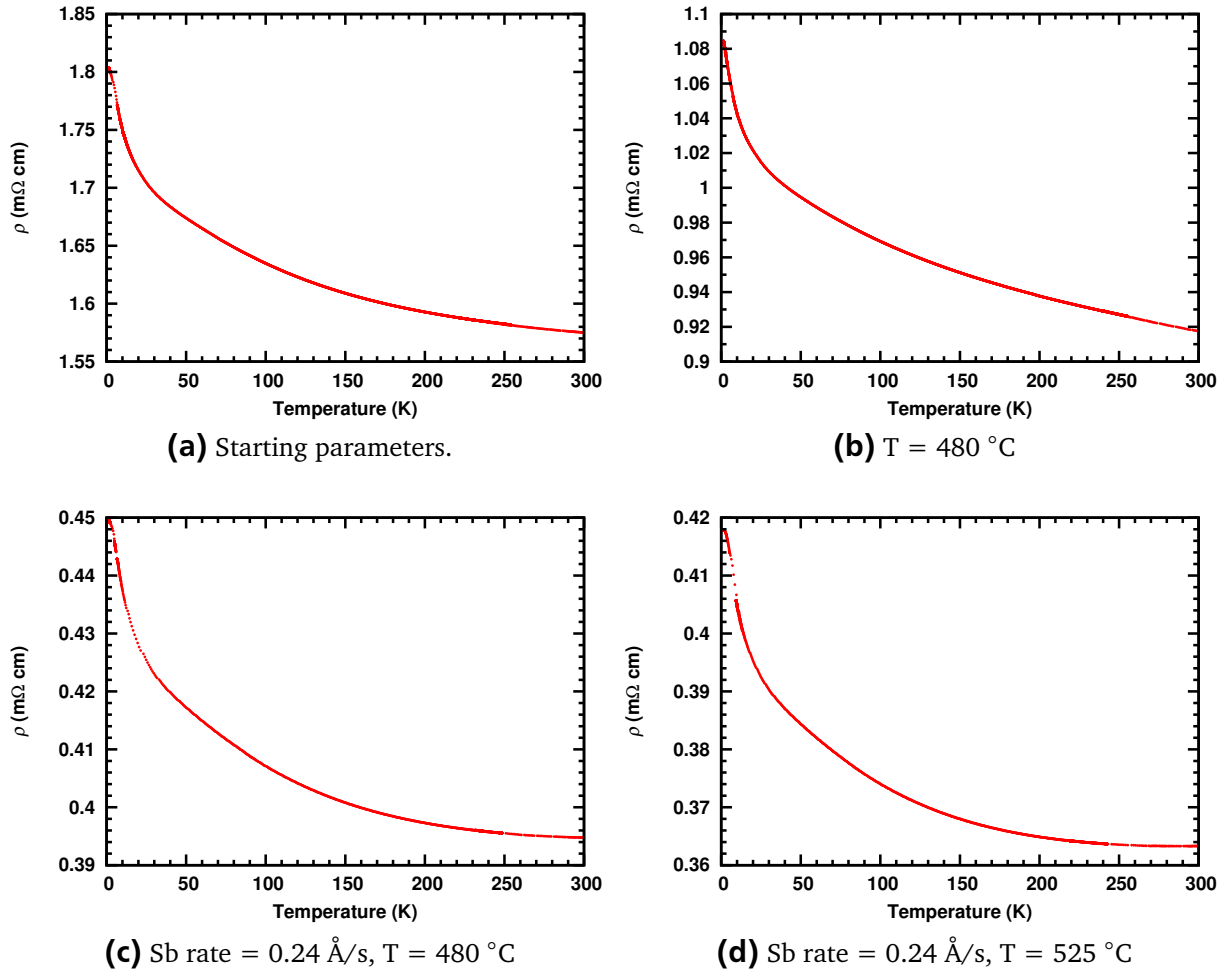

(a) Starting parameters.

(b) T = 480 °C

(c) Sb rate = 0.24 Å/s, T = 480 °C

(d) Sb rate = 0.24 Å/s, T = 525 °C

Figure 7.38: Resistivity measurements of the $CeNi_xSb_2$ films grown at various antimony rates and growth temperatures.

temperature was increased to a value of 480 °C and the result of the $2\theta - \theta$-scan is shown in figure 7.37b and one could identify NiSb impurities. Beside that, the formation of the $CeNi_xSb_2$ phase improved and additional peaks like the (002) and the (004) reflection can be detected. Further improvement in phase formation was achieved by increasing the growth temperature to a value of 525 °C (figure 7.37d). At this temperature, the NiSb impurity phase disappeared. Instead many reflections which can be indexed as (00l) reflections of the $CeNi_xSb_2$ phase are observed. An increase in antimony rate did not have an effect on phase formation (figure 7.37c).

This result shows that also the growth of an antimony '112'-type compound containing cerium is possible and the resistivity behaviour is of interest. Figure 7.38 shows the results of the resistivity measurements. There is no metallic behaviour observed for all of the $CeNi_xSb_2$ films. Instead the resistivity increases with decreasing temperature. For none of the films a T_C onset can be observed. This is in agreement with reports on bulk samples by Muro *et al.* [153]. They found $LaNiSb_2$ to be superconducting at temperatures below 1 K. For $CeNi_xSb_2$ a similar resistivity behavior of an increasing resistivity with decreasing temperature was found. The $CeNi_xSb_2$ films grown at a substrate temperature of 525 °C and an increased antimony rate of 0.24 Å/s exhibits a room temperature resistivity of

$\sim$363 $\mu\Omega$ cm and a resistivity of $\sim$418 $\mu\Omega$ cm at 1.6 K. These values are in good agreement with the resistivity values reported by Muro *et al*. [153]. For further investigation optimized growth parameters are necessary and further improvement in the crystal quality has to be done. The results presented here are a starting point for future work. Especially the growth temperature and the influence of the nickel rate on structural and electrical properties have to be studied in detail.

8 Summary and Outlook

The last section of this thesis gives a brief summary of the work done during this study and the results. Finally, a short outlook about possible future experiments is given.

The discovery of the iron based superconductors with at T_C as high as 56 K led to intense research activities all over the world. This was partly due to the reason of a different compound to that of cuprates which shows superconductivity with relatively high T_C, raising hope of sheding light on the mechanism of superconductivity in high T_C superconductors. At the same time, this new class of superconductors contain the toxic element arsenic. The goal of the present study discussed in this thesis is the search for new arsenic free compounds, which could be superconducting. As it was well established from the study of cuprate superconductors, substitution of various atomic sites in the new class of superconductors would lead to new compounds with better properties. In the present study, a thin film synthesis technique, namely RMBE, was chosen.

First of all the deposition of a '1111'-type $LaNiBiO_{1-x}$ compound was tried. Starting from results gained during a previous study, the focus of parameter optimization was put towards the oxidation conditions. However, even with the lowest oxidation conditions possible in the current MBE set up at Darmstadt University of Technology (0.17 sccm molecular oxygen) only polycrystalline films of low quality with considerable amount of La_2O_3 impurities could be fabricated. The films exhibit a T_C onset of 5 K which is higher than reported in bulk values [127], but no T_C zero was observed down to 4.2 K.

Since the oxidation conditions could not be lowered any further in the MBE set up and handling two different anions in one compound (O^{2-} and Bi^{3-}) is challenging, the focus was shifted to the thin film development of oxygen free compounds. The idea was to establish the growth conditions for the growth of arsenic free pnictide superconductors without have to handle two anions. Beside the '1111'-type compounds, there are mainly three different types of oxygen free compounds. The most important one is the '122'-type and the idea was to grow a lanthanum deficient '122'-type compound. As a starting point the results gained for the growth of the '1111'-type compound were used. Although it was possible to grow an epitaxial compound without any impurities after some optimization, it was clear that the compound which was synthesized was not the intended '122' compound as the XRD pattern showed forbidden reflections. ICP-OES measurements revealed a stoichiometry of '112'.

The new $LaNiBi_2$ compound was published shortly after the discovery during this work by Mizoguchi *et al.* [136]. The report was about a very unstable compound in ambient atmosphere with impurity phases and a T_C zero of 3.9 K. The crystal structure is the same *P4/nmm* structure as for the '1111' compounds. Peculiar in this novel compound is the presence of two different bismuth ions: Bi^{3-} in the NiBi plane and Bi^{1-} in a bismuth square net structure in the (001) layer of the unit cell.

During this work it was possible to optimize the deposition parameters to grow impurity free superconducting high quality thin films of $LaNi_xBi_2$ on MgO single crystal substrates. To best of our knowledge, this was the first report of high quality pnictide thin films without any impurity phases. For the optimization, temperature scans as well as composition tuning

were performed. Phase formation only was observed in a small growth temperature window between 390 °C and 450 °C. Above and below no phase formation was detected in $2\theta - \theta$ scans. At the optimum parameters a T_C zero of 3.95 K was observed. With varying the nickel rate T_C decreases on both sides of the optimum rate. The films exhibit poor metallic electrical behaviour. With a FWHM of the rocking curve of 0.06° the best films exhibit an excellent crystal quality. Laue oscillations observed in the $2\theta - \theta$ scans confirmed the good film quality. However, it was found that the films grow 45° rotated with respect to the MgO substrate. The reason for that is not yet clear and needs further investigation. One possible reason could be an atomic rearrangement so that the negatively charged ions of the film compound (bismuth) and the substrate (oxygen) avoid each other. Although the crystal quality of the films is very good, the films used to decompose when stored in ambient atmosphere within 1—2 days. When kept in humidity of around 60% the films decompose within a few hours. This is in contrast to the reported case of bulk synthesis by Mizoguchi *et al*. [136], where the samples directly decompose when exposed to the ambient atmosphere.

After the optimum parameters were found the power of the MBE technique could be demonstrated by substituting lanthanum by cerium. The $CeNi_xBi_2$ films exhibit a slightly higher T_C zero of 4.05 K. Besides that, the films are very similar to the $LaNi_xBi_2$ films in growth behaviour, crystal quality and stability in ambient atmosphere. Only the bismuth rate to grow the $CeNi_xBi_2$ films is more than twice as high as the rate needed for the $LaNi_xBi_2$ compound. Other than that the compounds are almost the same, even the 45° rotated growth on MgO was observed for these films.

After the optimum growth parameters for $LaNi_xBi_2$ and $CeNi_xBi_2$ compounds were found, other substitution experiments were performed. It could be shown that it is possible to substitute bismuth by antimony and nickel by copper. Here only first attempts were done and a phase formation was observed. Further optimization is necessary to study these compounds, as well.

This would be a good starting point for future experiments. While for the established compounds $LaNi_xBi_2$ and $CeNi_xBi_2$ the question of film rotation has to be clarified, for the other mentioned compounds the whole parameter optimization has to be done. For the future, one could also think about a substitution of bismuth by nitrogen and nickel by other transition metals such as iron, cobalt, palladium and so on. In addition, it would be interesting to measure important values such as H_C and J_C for the '112'-compounds. The mechanism of superconductivity is also not clear. It was reported that superconductivity, other than in the iron based superconductors, occurs in the bismuth square net and not in the NiBi layer [136]. High quality thin films could help to clarify this issue.

Recent publications report on superconductivity at 43 k in $Ca_{1-x}RE_xFeAs_2$ (RE = La to Gd) [154, 155]. Only Ce does not show a superconducting transition. All of these '112' compounds have the $P4/nmm$ crystal structure. Thus, it is possible to grow high quality thin films of this newly discovered compounds with rather high T_C using the parameters optimized and presented in this thesis.

Bibliography

[1] H. Kamerlingh-Onnes, Comm. Leiden, Suppl. Nr. **34** (1913).

[2] J. Bardeen, L. N. Cooper, and J. R. Schrieffer, Phys. Rev. **108**, 1175 (1957).

[3] J. G. Bednorz and K. A. Müller, Z. Phys. B Cond. Mat. **64**, 189 (1986).

[4] L. Gao, Y. Y. Xue, F. Chen, Q. Xiong, R. L. Meng, D. Ramirez, and C. W. Chu, Phys. Rev. B **50**, 4260 (1994).

[5] Y. Kamihara, T. Watanabe, M. Hirano, and H. Hosono, J. Am. Chem. Soc. **130**, 3296 (2008).

[6] C. Wang, L. Li, S. Chi, Z. Zhu, Z. Ren, Y. Li, Y. Wang, X. Lin, Y. Luo, S. Jiang, *et al.*, Europhys. Lett. **83**, 67006 (2008).

[7] M. K. Wu, J. R. Ashburn, C. J. Torng, P. H. Hor, R. L. Meng, L. Gao, Z. J. Huang, Y. Q. Wang, and C. W. Chu, Phys. Rev. Lett. **58**, 908 (1987).

[8] A. Schilling, M. Cantoni, J. D. Guo, and H. R. Ott, Nature **363**, 56 (1993).

[9] H. Kamerlingh-Onnes, Comm. Leiden **140b, c** u. **141b** (1914).

[10] D. J. Quinn and W. B. Ittner, J. Appl. Phys. **33**, 748 (1962).

[11] H. Ibach and H. Lüth, *Festkörperphysik - Einführung in die Grundlagen* (Springer, 2009), 7th ed., german.

[12] W. Buckel and R. Kleiner, *Supraleitung - Grundlagen und Anwendungen* (Wiley-VCH, 2004), 6th ed., german.

[13] W. Meißner and R. Ochsenfeld, Naturwissenschaften **21**, 787 (1933), german.

[14] F. London and H. London, Z. Phys. **96**, 359 (1935).

[15] C. Kittel, *Einführung in die Festkörperphysik* (Oldenbourg, 2006), 14th ed., german.

[16] R. Doll and M. Näbauer, Phys. Rev. Lett. **7**, 51 (1961).

[17] L. N. Cooper, Phys. Rev. **104**, 1189 (1956).

[18] H. Fröhlich, Phys. Rev. **79**, 845 (1950).

[19] J. Bardeen, L. N. Cooper, and J. R. Schrieffer, Phys. Rev. **106**, 162 (1957).

[20] Z. A. Ren, J. Yang, W. Lu, W. Yi, X. L. Shen, Z. C. Li, G. C. Che, X. L. Dong, L. L. Sun, F. Zhou, *et al.*, Europhys. Lett. **82**, 57002 (2008).

[21] H. Kito, H. Eisaki, and A. Iyo, J. Phys. Soc. Jpn. **77**, 063707 (2008).

[22] Z.-A. Ren, W. Lu, J. Yang, W. Yi, X.-L. Shen, Z.-C. Li, G.-C. Che, X.-L. Dong, L.-L. Sun, F. Zhou, *et al.*, Chin. Phys. Lett. **25**, 2215 (2008).

[23] M. Rotter, M. Tegel, and D. Johrendt, Phys. Rev. Lett. **101**, 107006 (2008).

[24] K. Sasmal, B. Lv, B. Lorenz, A. Guloy, F. Chen, Y.-Y. Xue, and C. Chu, Phys. Rev. Lett. **101**, 107007 (2008).

[25] G. Chen, Z. Li, J. Dong, G. Li, W. Hu, X. Zhang, X. Song, P. Zheng, N. Wang, and J. Luo, Phys. Rev. B **78**, 224512 (2008).

[26] J. Tapp, Z. Tang, B. Lv, K. Sasmal, B. Lorenz, P. Chu, and A. Guloy, Phys. Rev. B **78**, 060505(R) (2008).

[27] X. Wang, Q. Liu, Y. Lv, W. Gao, L. Yang, R. Yu, F. Li, and C. Jin, Solid State Commun. **148**, 538 (2008).

[28] M. Pitcher, D. Parker, P. Adamson, S. Herkelrath, A. Boothroyd, R. Ibberson, M. Brunelli, and S. Clarke, Chem. Commun. 2008 p. 5918 (2008).

[29] F.-C. Hsu, J.-Y. Luo, K.-W. Yeh, T.-K. Chen, T.-W. Huang, P. Wu, Y.-C. Lee, Y.-L. Huang, Y.-Y. Chu, D.-C. Yan, *et al.*, Proc. Nat. Acad. Sci. USA **105**, 14262 (2008).

[30] J. Jaroszynski, F. Hunte, L. Balicas, Y.-J. Jo, I. Raievic, A. Gurevich, D. C. Larbalestier, F. F. Balakirev, L. Fang, P. Cheng, *et al.*, Phys. Rev. B **78**, 174523 (2008).

[31] M. M. Altarawneh, K. Collar, C. H. Mielke, N. Ni, S. L. Bud'ko, and P. C. Canfield, Phys. Rev. B **78**, 220505(R) (2008).

[32] H. Q. Yuan, J. Singleton, F. F. Balakirev, S. A. Baily, G. F. Chen, J. L. Luo, and N. L. Wang, Nature **457**, 565 (2009).

[33] M. Kano, Y. Kohama, D. Graf, F. Balakirev, A. S. Sefat, M. A.McGuire, B. C. Sales, D.Mandrus, and S. Tozer, J. Phys. Soc. Jpn. **78**, 084719 (2009).

[34] A. S. Sefat, R. Jin, M. A. McGuire, B. C. Sales, D. J. Singh, and D. Mandrus, Phys. Rev. Lett. **101**, 117004 (2008).

[35] A. Yamamoto, J. Jaroszynski, C. Tarantini, L. Balicas, J. Jiang, A. Gurevich, D. C. Larbalestier, R. Jin, A. S. Sefat, M. A. McGuire, *et al.*, Appl. Phys. Lett. **94**, 062511 (2009).

[36] S. A. Baily, Y. Kohama, H. Hiramatsu, B. Maiorov, F. F. Balakirev, M. Hirano, and H. Hosono, Phys. Rev. Lett. **102**, 117004 (2009).

[37] Y. J. Song, J. S. Ghim, B. H. Min, Y. S. Kwon, M. H. Jung, and J.-S. Rhyee, Appl. Phys. Lett. **96**, 212508 (2010).

[38] M. Putti, I. Pallecchi, E. Bellingeri, M. R. Cimberle, M. Tropeano, C. Ferdeghini, A. Palenzona, C. Tarantini, A. Yamamoto, J. Jiang, *et al.*, Supercond. Sci. Technol. **23**, 034003 (2010).

[39] H. F. Braun, Phys. Lett. A **75**, 386 (1980).

[40] B. S. Chandrasekhar and J. K. Hulm, J. Phys. Chem. Solids **7**, 259 (1958).

[41] K. .Shimizu, T. Kimura, S. Furomoto, K. Takeda, K. Kontani, Y. Onuki, and K. Amaya, Nature **412**, 316 (2001).

[42] D. C. Johnston, Adv. in Phys. **59**, 803 (2010).

[43] S. Fujitsu, S. Matsuishi, and H. Hosono, Int. Mater. Rev. **57**, 311 (2012).

[44] V. Johnson and W. Jeitschko, J. Solid State Chem. **11**, 161 (1974).

[45] Y. Kamihara, H. Hiramatsu, M. Hirano, R. Kawamura, H. Yanagi, T. Kamiya, and H. Hosono, J. Am. Chem. Soc. **128**, 10012 (2006).

[46] K. Miyazawa, S. Ishida, K. Kihou, P. M. Shirage, M. Nakajima, C. H. Lee, H. Kito, Y. Tomioka, T. Ito, H. Eisaki, *et al.*, Appl. Phys. Lett. **96**, 072514 (2010).

[47] S. Matsuishi, Y. Inoue, T. Nomura, H. Yanagi, M. Hirano, , and H. Hosono, J. Am. Chem. Soc. **130**, 14428 (2008).

[48] S. Matsuishi, Y. Inoue, T. Nomura, M. Hirano, and H. Hosono, J. Phys. Soc. Jpn. **77**, 113709 (2008).

[49] K. Ishida, Y. Nakati, and H. Hosono, J. Phys. Soc. Jpn. **78**, 062001 (2009).

[50] X. F. Wang, T. Wu, G. Wu, H. Chen, Y. L. Xie, J. J. Ying, Y. J. Yan, R. H. Liu, and X. H. Chen, Phys. Rev. Lett. **102**, 117005 (2009).

[51] C.-H. Lee, A. Iyo, H. Eisaki, H. Kito, M. T. Fernandez-Diaz, T. Ito, K. Kihou, H. Matsuhata, M. Braden, and K. Yamada, J.Phys. Soc. Jpn. **77**, 083704 (2008).

[52] A. F. Kemper, T. A. Maier, S. Graser, H.-P. Cheng, P. J. Hirschfeld, and D. J. Scalapino, New J. Phys. **12**, 073030 (2010).

[53] K. Kuroki, H. Usui, S. Onari, R. Arita, and H. Aoki, Phys. Rev. B **79**, 224511 (2009).

[54] H. Ogino, Y. Matsumara, Y. Katsura, K. Ushiyama, S. Horii, K. Kishio, and J.-I. Shimoyama, Supercond. Sci. Technol. **22**, 075008 (2009).

[55] G. R. Stewart, Rev. Mod. Phys. **83**, 1589 (2011).

[56] N. Terasaki, H. Mukuda, M. Yashima, Y. Kitaoka, K. Miyazawa, P. M. Shirage, H. Kito, H. Eisaki, and A. Iyo, J. Phys. Soc. Jpn. **78**, 013701 (2009).

[57] F. Ning, K. Ahilan, T. Imai, A. S. Sefat, R. Jin, M. A. McGuire, B. C. Sales, and D. Mandrus, J. Phys. Soc. Jpn. **77**, 013705 (2008).

[58] P. C. Canfield, S. L. Budko, N. Ni, J. Q. Yan, and A. Kracher, Phys. Rev. B **80**, 060501 (2009).

[59] N. Ni, A. Thaler, A. Kracher, J. Q. Yan, S. L. Budko, and P. C. Canfield, Phys. Rev. B **80**, 024511 (2009).

[60] S. Jiang, H. Xing, G. Xuan, C. Wang, Z. Ren, C. Feng, J. Dai, Z. Xu, and G. Cao, J. Phys.: Condens. Matter **21**, 382203 (2009).

[61] Z.Wang, H. Yang, C. Ma, H. Tian, H. Shi, J. Lu, L. Zeng, and J. Li, J. Phys.: Condens. Matter **21**, 495701 (2009).

[62] M. Rotter, C. Hieke, and D. Johrendt, Phys. Rev. B **82**, 014513 (2010).

[63] T. Nakano, S. Tsutsumi, N. Fujiwara, S. Matsuishi, and H. Hosono, Phys. Rev. B **83**, 180508 (2011).

[64] X. F. Wang, T. Wu, G. Wu, R. H. Liu, H. Chen, Y. L. Xie, and X. H. Chen, New J. Phys. **11**, 045003 (2009).

[65] C. Lester, J.-H. Chu, J. G. Analytis, S. C. Capelli, A. S. Erickson, C. L. Condron, M. F. Toney, I. R. Fisher, and S. M. Hayden, Phys. Rev. B **79**, 144523 (2009).

[66] F. Rullier-Albenque, D. Colson, A. Forget, and H. Alloul, Phys. Rev. Lett. **103**, 057001 (2009).

[67] J. Guo, S. Jin, G. Wang, S. Wang, K. Zhu, T. Zhou, M. He, and X. Chen, Phys. Rev. B **82**, 180520(R) (2010).

[68] C.-T. Chen, C. C. Tsuei, M. B. Ketchen, Z.-A. Ren, and Z. X. Zhao, Nature Phys. **6**, 260 (2010).

[69] D. R. Parker, M. J. Pitcher, P. J. Baker, I. Franke, T. Lancaster, S. J. Blundell, and S. J. Clarke:, Chem. Commun. **16**, 2189 (2009).

[70] M. Wang, M. Wang, H. Miao, S. V. Carr, D. L. Abernathy, M. B. Stone, X. C. Wang, L. Xing, C. Q. Jin, X. Zhang, *et al.*, Phys. Rev. B **86**, 144511 (2012).

[71] S. Borisenko, V. Zabolotnyy, D. Evtushinsky, T. Kim, I. Morozov, A. Yaresko, A. Kordyuk, G. Behr, A. Vasiliev, R. Follath, *et al.*, Phys. Rev. Lett. **105**, 067002 (2010).

[72] M. J. Pitcher, T. Lancaster, J. D. Wright, I. Franke, A. J. Steele, P. J. Baker, F. L. Pratt, W. T. Thomas, D. R. Parker, S. J. Blundell, *et al.*, J. Am. Ceram. Soc. **132**, 10467 (2010).

[73] T. M. McQueen, Q. Huang, V. Ksenofontov, C. Felser, Q. Xu, H. Zandbergen, Y. S. Hor, J. Allred, A. J. Williams, D. Qu, *et al.*, Phys. Rev. B **79**, 014522 (2009).

[74] T. M. McQueen, A. J. Williams, P. W. Stephens, J. Tao, Y. Zhu, V. Ksenofontov, F. Casper, C. Felser, and R. J. Cava, Phys. Rev. Lett. **103**, 057002 (2009).

[75] R. Viennois, E. Giannini, D. van der Marel, and R. Cerny, J. Solid State Chem. **183**, 769 (2010).

[76] Y. Mizuguchi, F. Tomioka, S. Tsuda, T. Yamaguchi, and Y. Takano, J. Phys. Soc. Jpn. **78**, 074712 (2009).

[77] N. Katayama, S. Ji, D. Louca, S.-H. Lee, M. Fujita, T. J. Sato, J. S. Wen, Z. J. Xu, G. D. Gu, G. Xu, *et al.*, J. Phys. Soc. Jpn. **79**, 113702 (2010).

[78] S. Margadonna, Y. Takabayashi, Y. Ohishi, Y. Mizuguchi, Y. Takano, T. Kagayama, T. Nakagawa, M. Takata, and K. Prassides, Phys. Rev. B **80**, 064506 (2009).

[79] R. H. Liu, X. G. Luo, M. Zhang, A. F. Wang, J. J. Ying, X. F. Wang, Y. J. Yan, Z. J. Xiang, P. Cheng, G. J. Ye, *et al.*, Europhys. Lett. **94**, 27008 (2011).

[80] F. Hunte, J. Jaroszynski, A. Gurevich, D. C. Larbalestier, R. Jin, A. S. Sefat, M. A. McGuire, B. C. Sales, D. K. Christen, and D. Mandrus, Nature **453**, 903 (2008).

[81] H. Hiramatsu, T. Katase, T. Kamiya, and H. Hosono, J. Phys. Soc. Jpn. **81**, 011011 (2012).

[82] H. Hiramatsu, T. Katase, T. Kamiya, M. Hirano, and H. Hosono, Appl. Phys. Lett. **93**, 162504 (2008).

[83] E. Backen, S. Haindl, T. Niemeier, R. Hühne, T. Freudenberg, J. Werner, G. Behr, L. Schultz, and B. Holzapfel, Supercond. Sci. Technol. **21**, 122001 (2008).

[84] M. Kidszun, S. Haindl, E. Reich, J. Hänisch, K. Iida, L. Schultz, and B. Holzapfel, Supercond. Sci. Technol. **23**, 022002 (2010).

[85] S. Haindl, M. Kidszun, A. Kauffmann, K. Nenkov, N. Kozlova, J. Freudenberger, T. Thersleff, J. Hänisch, J. Werner, E. Reich, *et al.*, Phys. Rev. Lett. **104**, 077001 (2010).

[86] M. Kidszun, S. Haindl, T. Thersleff, J. Werner, M. Langer, J. Hänisch, K. Iida, E. Reich, L. Schultz, and B. Holzapfel, Europhys. Lett. **90**, 57005 (2010).

[87] T. Kawaguchi, H. Uemura, T. Ohno, R. Watanabe, M. Tabuchi, T. Ujihara, K. Takenaka, Y. Takeda, and H. Ikuta, Appl. Phys. Exp. **2**, 093002 (2009).

[88] T. Kawaguchi, H. Uemura, T. Ohno, M. Tabuchi, T. Ujihara, K. Takenaka, Y. Takeda, and H. Ikuta, Appl. Phys. Lett. **97**, 042509 (2010).

[89] S. Ueda, T. Yamagishi, S. Takeda, S. Agatsuma, S. Takano, A. Mitsuda, and M. Naito, Physica C **471**, 1167 (2011).

[90] H. Uemura, T. Kawaguchi, T. Ohno, M. Tabuchi, T. Ujihara, Y. Takeda, and H. Ikuta, Solid State Commun. **152**, 735 (2012).

[91] A. Leithe-Jasper, W. Schnelle, C. Geibel, and H. Rosner, Phys. Rev. Lett. **101**, 207004 (2008).

[92] H. Hiramatsu, T. Katase, T. Kamiya, M. Hirano, and H. Hosono, Appl. Phys. Express **1**, 101702 (2008).

[93] E.-M. Choi, S.-G. Jung, N. H. Lee, Y.-S. Kwon, W. N. Kang, D. H. Kim, M.-H. Jung, S.-I. Lee, and L. Sun, Appl. Phys. Lett. **95**, 062507 (2009).

[94] H. Hiramatsu, T. Katase, T. Kamiya, M. Hirano, and H. Hosono, Phys. Rev. B **80**, 052501 (2009).

[95] J. S. Kim, T. D. Blasius, E. G. Kim, and G. R. Stewart:, J. Phys.: Condens. Matter **21**, 342201 (2009).

[96] S. R. Saha, N. P. Butch, K. Kirshenbaum, J. Paglione, and P. Y. Zavalij, Phys. Rev. Lett. **103**, 037005 (2009).

[97] Y. Mizuguchi, K. Deguchi, S. Tsuda, T. Yamaguchi, and Y. Takano, Phys. Rev. B **81**, 214510 (2010).

[98] T. Hanna, Y. Muraba, S. Matsuishi, N. Igawa, K. Kodama, S. Shamoto, and H. Hosono, Phys. Rev. B **84**, 024521 (2011).

[99] Y. Mizuguchi, K. Deguchi, S. Tsuda, T. Yamaguchi, and Y. Takano, Europhys. Lett. **90**, 57002 (2010).

[100] Y. Mizuguchi, K. Deguchi, Y. Kawasaki, T. Ozaki, M. Nagao, Tsuda, T. Yamaguchi, and Y. Takano, J. Appl. Phys. **109**, 013914 (2011).

[101] H. Hiramatsu, T. Katase, T. Kamiya, and H. Hosono, IEEE Trans. Appl. Supercond. **23**, 7300405 (2013).

[102] S. Agatsuma, T. Yamagishi, S. Takeda, and M. Naito, Physica C **470**, 1468 (2010).

[103] T. Katase, H. Hiramatsu, H. Yanagi, T. Kamiya, M. Hirano, and H. Hosono, Solid State Commun. **149**, 2121 (2009).

[104] K. Iida, J. Hänisch, R. Hühne, F. Kurth, M. Kidszun, S. Haindl, J. Werner, L. Schultz, and B. Holzapfel, Appl. Phys. Lett. **95**, 192501 (2009).

[105] S. Lee, J. Jiang, J. D. Weiss, C. M. Folkman, C. W. Bark, C. Tarantini, A. Xu, D. Abraimov, A. Polyanskii, C. T. Nelson, *et al.*, Appl. Phys. Lett. **95**, 212505 (2009).

[106] S. Lee, J. Jiang, Y. Zhang, C. W. Bark, J. D. Weiss, C. Tarantini, C. T. Nelson, H. W. Jang, C. M. Folkman, S. H. Baek, *et al.*, Nat. Mater. **9**, 397 (2010).

[107] K. Iida, S. Haindl, T. Thersleff, J. Hänisch, F. Kurth, M. Kidszun, R. Hühne, I. Mönch, L. Schultz, B. Holzapfel, *et al.*, Appl. Phys. Lett. **97**, 172507 (2010).

[108] K. Iida, J. Hänisch, T. Thersleff, F. Kurth, M. Kidszun, S. Haindl, R. Hühne, L. Schultz, and B. Holzapfel, Phys. Rev. B **81**, 100507 (2010).

[109] N. H. Lee, S.-G. Jung, D. H. Kim, and W. N. Kang, Appl. Phys. Lett. **96**, 202505 (2010).

[110] S. Takeda, S. Ueda, T. Yamagishi, S. Agatsuma, S. Takano, A. Mitsuda, and M. Naito, Appl. Phys. Express **3**, 093101 (2010).

[111] M. K. Wu, F. C. Hsu, K. W. Yeh, T. W. Huang, J. Y. Luo, M. J. Wang, H. H. Chang, T. K. Chen, S. M. Rao, B. H. Mok, *et al.*, Physica C **469**, 340 (2009).

[112] M. J. Wang, J. Y. Luo, T. W. Huang, H. H. Chang, T. K. Chen, F. C. Hsu, C. T. Wu, P. M. Wu, A. M. Chang, and M. K. Wu, Phys. Rev. Lett. **103**, 117002 (2009).

[113] Y. Han, W. Y. Li, L. X. Cao, S. Zhang, B. Xu, and B. R. Zhao, J. Phys.: Condens. Matter **21**, 235702 (2009).

[114] Y. Han, W. Y. Li, L. X. Cao, X. Y. Wang, B. Xu, B. R. Zhao, Y.Guo, and J. L. Yang, Phys. Rev. Lett. **104**, 017003 (2010).

[115] E. Bellingeri, I. Pallecchi, R. Buzio, A. Gerbi, D. Marrè, M. R. Cimberle, M. Tropeano, M. Putti, A. Palenzona, and C. Ferdeghini, Appl. Phys. Lett. **96**, 102512 (2010).

[116] M. Ohring, *Materials Science of Thin Films* (Academic Press, 2002), 2nd ed.

[117] K. L. Chopra, *Thin Film Phenomena* (McGraw-Hill Book Company, 1969).

[118] M. A. Herman, W. Richter, and H. Sitter, *Epitaxy*, vol. 62 (Springer, 2004).

[119] J. M. Phillips, J. Appl. Phys. **79**, 1829 (1996).

[120] B. H. Moeckly, S. E. Russek, D. K. Llathrop, R. A. Buhrmann, J. Li, and J. W. Mayer, Appl. Phys. Lett. **57**, 1687 (1990).

[121] A. Ichimiya and P. I. Cohen, *Reflection High Energy Electron Diffraction* (Cambridge University Press, 2004), 1st ed.

[122] G. Diehl, *An Overview of Thin Film Deposition Measurement & Control Techniques* (Sigma Instruments, 2006).

[123] M. Birkholz, *Thin Film Analysis by X-Ray Scattering* (WILEY-VCH, 2006).

[124] J. B. Nelson and D. P. Riley, Proc. Phys. Soc. Lond. **8**, 160 (1945).

[125] M. McElfresh, *Fundamentals of Magnetism and Magnetic Measurements* (Quantum Design, 1994).

[126] S. Muir, J. Vielma, G. Schneider, A. Sleight, and M. Subramanian, J. Solid State Chem. **185**, 156 (2012).

[127] V. L. Kozhevnikov, O. N. Leonidova, A. L. Ivanovskii, I. R. Shein, B. N. Goshchitskii, and A. E. Kar'kin, JETP Lett. **87**, 649 (2008).

[128] A. Buckow, *Thin Film Deposition of the Superconductor LaNiBiO$_{1-x}$ using Reactive Molecular Beam Epitaxy* (Darmstadt University of Technology, Diploma Thesis 2009).

[129] *ICDD PDF Card 04-007-2357* (Last Modification Date: 25.01.2010).

[130] A. Buckow, R. Retzlaff, J. Kurian, and L. Alff, Phys. Proc. **27**, 300 (2012).

[131] H. T. Takeshita, T. Oishi, and N. Kuriyama, J. Alloys Compounds **333**, 266 (2002).

[132] G. Elert, *The Physics Hypertextbook* (Online, 2012), URL `http://physics.info`.

[133] M. Naito and K. Ueda, Supercond. Sci. Technol. **17**, R1 (2004).

[134] B. T. Matthias, Phys. Rev. **92**, 874 (1953).

[135] S. Park, K. Kang, W. Han, and T. Vogt, J. Alloys Compounds **400**, 88 (2005).

[136] H. Mizoguchi, S. Matsuishi, M. Hirano, M. Tachibana, E. Takayama-Muromachi, H. Kawaji, and H. Hosono, Phys. Rev. Lett **106**, 057002 (2011).

[137] K. Kodama, S. Wakimoto, N. Igawa, S. Shamoto, H. Mizoguchi, and H. Hosono, Phys. Rev. B **83**, 214512 (2011).

[138] J. Park, G. Lee, F. Wolff-Fabris, Y. Y. Koh, M. J. Eom, Y. K. Kim, M. A. Farhan, Y. J. Jo, C. Kim, J. H. Shim, *et al.*, Phys. Rev. Lett. **107**, 126402 (2011).

[139] J. K. Wang, L. L. Zhao, Q. Yin, G. Kotliar, M. S. Kim, M. C. Aronson, and E. Morosa, Phys. Rev. B **84**, 064428 (2011).

[140] L. Schoop, D. Hirai1, C. Felser, and R. J. Cava, Europhys. Lett. **101**, 67001 (2013).

[141] A. D. Hillier, J. Quintanilla, and R. Cywinski, Phys. Rev. Lett. **102**, 117007 (2009).

[142] O. Y. Zelinska and A. Mar, J. Solid State Chem. **179**, 3776 (2006).

[143] A. Buckow, R. Retzlaff, J. Kurian, and L. Alff, Supercond. Sci. Technol. **26**, 015014 (2013).

[144] H. Luetkens, H. H. Klauss, M. Kraken, F. J. Litterst, T. Dellmann, R. Klingeler, C. Hess, R. Khasanov, A. Amato, C. Baines, *et al.*, Nature Mater. **8**, 305 (2009).

[145] P. Mele, K. Matsumoto, Y. Haruyama, M. Mukaida, Y. Yoshida, and T. Kiss, Appl. Phys. Expr. **2**, 073002 (2009).

[146] A. Buckow, K. Kupka, R. Retzlaff, J. Kurian, and L. Alff, Appl. Phys. Lett. **101**, 162602 (2012).

[147] J. Kurian and M. Naito, IEEE Trans. Appl. Supercond. **15**, 2966 (2005).

[148] I. Vartanyants, C. Ern, W. Donner, W. Caliebe, and H. Dosch, Appl. Phys. Lett. **77**, 3929 (2000).

[149] C. Uher and W. P. Pratt, Phys. Rev. Lett. **39**, 491 (1977).

[150] H. Flandorfer, O. Sologub, C. Godart, K. Hiebl, A. Leithe-Jasper, P. Rogl, and H. Noel, Solid State Commun. **97**, 561 (1996).

[151] J. Ye, Y. K. Huang, K. Kadowaki, and T. Matsumoto, Acta Cryst. **C52**, 1323 (1996).

[152] M. C. L. Clanche, S. Deputier, J. C. Jegaden, R. G. rin, Y. Ballini, and A. Givarc'h, J. Alloys Compds. **206**, 21 (1994).

[153] Y. Muro, N. Takeda, and M. Ishikawa, J. Alloys Compds. **257**, 23 (1997).

[154] K. Kudo, T. Mizukami, Y. Kitahama, D. Mitsuoka, K. Iba, K. Fujimura, N. Nishimoto, Y. Hiraoka, and M. Nohara, J. Phys. Soc. Jpn. **83**, 025001 (2014).

[155] A. Sala, H. Yakita, H. Ogino, T. Okada, A. Yamamoto, K. Kishio, S. Ishida, A. Iyo, H. Eisaki, M. Fujioka, *et al.*, arXiv:1404.2738 (2014).

List of Figures

List of Tables

Acknowledgement

I want to thank Prof. Dr. Lambert Alff for the possibility to do my PhD thesis in such an interesting and late-breaking topic.

In addition I wish to thank Prof. Dr. Wolfgang Donner for being the second assessor of my thesis and for his infinite input in all aspects of X-ray diffraction.

I thank Prof. Dr. Wolfgang Ensinger and Prof. Dr. Barbara Albert for taking the part of 3rd and 4th examiner.

Furthermore I want to thank Dr. Jose Kurian for his supervising. With infinite patience he gave me an amazing insight in science of thin films, MBE and superconductivity.

My further thanks goes to Renate Benz for performing the ICP-OES measurements for me.

A big thanks goes to the rest of the ATFT group. You guys are special.

A special thanks goes to family Baulig and family Berg for letting me be a part of your everyday life. I wish you all the best.

I am thankful for my family. You are the ones who made this possible and I can not thank you enough!

My last thanks are for my wife Lydia and our wonderful son Leonas. Lydia, I thank you for your support in so many ways and Leonas, I thank you for showing me what is really important in life.

Publications

R. Retzlaff, A. Buckow, P. Komissinskiy, S. Ray, S. Schmidt, H. Mühlig, F. Schmidl, P. Seidel, J. Kurian and L. Alff, *Superconductivity and role of pnictogen and Fe substitution in 112-$LaPd_xPn_2$ (Pn=Sb,Bi)*, Phys. Rev. B **91** (2015) 104519

A. Buckow, R. Retzlaff, J. Kurian and L. Alff, *Growth of superconducting epitaxial $LaNi_xBi_2$ pnictide thin films with a Bi square net layer by reactive molecular beam epitaxy*, Supercond. Sci. Technol. **26** (2013) 015014

J. Kurian, A. Buckow, R. Retzlaff, L. Alff, *Search for superconductivity in $LaNiP_2$ (P = Bi, Sb) thin films grown by reactive molecular beam epitaxy*, Physica C **484** (2013) 171–174

A. Buckow, K. Kupka, R. Retzlaff, J. Kurian, and L. Alff, *Superconducting epitaxial thin films of $CeNi_xBi_2$ with a bismuth square net structure*, Appl. Phys. Lett. **101** (2012) 162602

A. Buckow, R. Retzlaff, J. Kurian, L. Alff, *MBE growth of $LaNiBiO_{1-x}$ thin films*, Physics Procedia **27** (2012) 300–303

R. Hord, G. Cordier, K. Hofmann, A. Buckow, G. Pascua, H. Luetkens, L. Alff, B. Albert, *Transitions Between Lanthanum Cuprates: Crystal Structures of T′, Orthorhombic, and K_2NiF_4-type La_2CuO_4*, Z. Anorg. Allg. Chem. **637** (2011) 1114–1117

R. Hord, H. Luetkens, G. Pascua, A. Buckow, K. Hofmann, Y. Krockenberger, J. Kurian, H. Maeter, H.-H. Klauss, V. Pomjakushin, A. Suter, B. Albert, and L. Alff, *Enhanced two-dimensional behavior of metastable T'-La_2CuO_4, the parent compound of electron-doped cuprate superconductors*, Phys. Rev. B **82** (2010) 180508(R)

Conference contributions

R. Retzlaff, A. Buckow *et al.*, *Superconducting thin films of As-free pnictide $LaPd_{1-x}Sb_2$ grown by reactive molecular beam epitaxy*, DPG spring-meeting 2013 (Regensburg)

A. Buckow *et al.*, *Synthesis of As-free pnictide superconductors $RENi_{1-x}Bi_2$ (RE=La, Ce) using Molecular Beam Epitaxy*, DPG spring-meeting 2012 (Berlin)

R. Retzlaff, A. Buckow *et al.*, *As-free pnictide $LaNi_{1-x}Sb_2$ thin films grown by Reactive Molecular Beam Epitaxy*, DPG spring-meeting 2012 (Berlin)

J. Kurian, A. Buckow *et al.*, *Epitaxial thin films of arsenic free pnictide superconductors grown by MBE*, International Symposium on Superconductivity 2011 (Tokio)

A. Buckow *et al.*, *MBE growth of $LaNiBiO_{1-x}$ thin films*, International Symposium on Superconductivity 2011 (Tokio)

A. Buckow *et al.*, *Search for novel arsenic free pnictide superconductors*, DPG spring-meeting 2011 (Dresden)

A. Buckow *et al.*, *Enhanced two-dimensional behaviour of metastable T'–La_2CuO_4, the parent compound of electron doped cuprate superconductors*, DPG spring-meeting 2011 (Dresden)

A.Buckow *et al.*, *Thin Film Deposition of the Pnictide Superconductors $LaO_{1-x}NiBi$ and $LaO_{1-x}CuBi$ using Reactive Molecular Beam Epitaxy*, DPG spring-meeting 2010 (Regensburg)

Curriculum Vitae

Personal data

born	16th of September 1983 in Hanau
martial status	married, one child

Career

2012 – today	Research Staff Member and Group Leader, Fraunhofer Institute for Silicate Research ISC – Project Group Materials Recycling and Resource Strategies IWKS, Alzenau and Hanau, Germany
2009 – 2012	Research Staff Member, Darmstadt University of Technology, Materials Science Department, Advanced Thin Film Technology Devision, Darmstadt, Germany

University

2009 – 2015	PhD at Darmstadt University of Technology, Materials Science Department, Advanced Thin Film Technology Devision, Darmstadt, Germany
2004 – 2009	Studies of Materials Science, Darmstadt University of Technology, Darmstadt, Germany

Alternative Civilian Service

2003 – 2004	Evangelische Johanneskirchengemeinde Hanau, Hanau, Germany

School

1994 – 2003	Secondary School: Hohe Landesschule Hanau, Hanau, Germany
1990 – 1994	Elementary School: Grundschule Rückingen, Erlensee, Germany